

COMPUTATIONAL STUDIES OF COMPLEX CRYSTAL STRUCTURES

A Dissertation

Presented to the Faculty of the Graduate School
of Cornell University

in Partial Fulfillment of the Requirements for the Degree of
Doctor of Philosophy

by

Brian Michael Abbett

August 2018

© 2018 Brian Michael Abbett
ALL RIGHTS RESERVED

COMPUTATIONAL STUDIES OF COMPLEX CRYSTAL STRUCTURES

Brian Michael Abbett, Ph.D.

Cornell University 2018

The properties of numerous technologically important materials are determined by the crystal structure. Understanding the relationship between a material's properties and its crystal structure allows materials with specific properties to be designed by modifying or controlling the crystal structure. Many materials have been designed using chemical intuition which is continually improved as more and more materials are made. This process relies on new materials being synthesized and characterized, which often requires significant time and effort.

Density functional theory was developed more than half a century ago and provides a way to simulate the electronic structure, and therefore numerous properties of a crystal structure. Combined with ever improving computational abilities, in many cases it has become easier to study materials by simulating their properties than synthesizing them. While these simulations do not perfectly replicate the properties of a real material, the predictions of simulations are often reliable enough to serve as a guide for where to focus experimental efforts.

Simulations provide a straightforward way to study crystals that may not be possible to synthesize experimentally because the crystal structure is completely controlled during a simulation, whereas the laws of physics control an actual crystal structure. This precise control over the crystal structure allows the relationship between crystal structure and a material's properties to be easily and directly probed. Once this relationship is understood, efforts can be

made to force a material to form in a crystal structure with desirable properties.

This dissertation presents several computational studies, primarily using density functional theory, of crystal structures and their relationship to macroscopic properties. $\text{La}_2\text{SrCr}_2\text{O}_7$ was studied to explain why it forms in a never before seen crystal structure. A coupling between *A*-site disorder, *B*-site chemistry, and octahedral rotations was found and provides a route towards controlling the crystal structure in related materials. Antiferroelectricity was studied in PbZrO_3 and found to be dependent on a flat energy landscape encompassing nonpolar and polar structures. Ideas for future work to improve the understanding of antiferroelectricity and possibly designing new antiferroelectrics are discussed. Finally, the crystal structure of $\text{Ln}_2\text{NiO}_{4+\delta}$ was studied, paying particular attention to the arrangement of excess oxygen atoms. These arrangements have a significant effect on the properties of $\text{Ln}_2\text{NiO}_{4+\delta}$ and should be considered in future computational studies.

BIOGRAPHICAL SKETCH

Brian Abbett was born and raised in Montgomery Village, Maryland. In 2006 he enrolled in the College of Engineering at Cornell University. During his undergraduate studies he developed an interest in simulating complex systems and earned a B.S. in Engineering Physics with minors in Applied Mathematics and Information Science in 2010. Having decided he liked being at Cornell, Brian stayed for an extra year to earn an M.Eng. in Engineering Physics in 2011. During that year he further developed his computational skills by simulating a two dimensional disc galaxy with a black hole in the center for his M. Eng. project under the advisement of Professor Lovelace. Brian then decided to pursue a Ph.D. in Applied Physics and joined Professor Fennie's research group to perform first principles simulations of materials. After several years he added Professor Benedek as a second adviser, whose research also involves simulating materials. Twelve years after originally enrolling at Cornell, Brian had learned a tremendous amount at Cornell and decided it was time to continue pursuing his passion of simulating complex systems in a new environment.

ACKNOWLEDGEMENTS

I would like to thank my advisers Professor Craig Fennie and Professor Nicole Benedek for their support and guidance while I was in graduate school. I would also like to thank Professor Charles Van Loan and Professor Darrell Schlom for serving on my committee and providing advice and mentorship during my time at Cornell.

I would also like to extend thanks to everyone that worked in the Fennie or Benedek groups during the last several years. In particular I would like to thank Guru Khalsa for the numerous discussion we had which were invaluable to completing my Ph.D. Also, Turan Birol for helping me learn about the numerous subtleties involved in the type of research performed in our group. Thanks also to Gerhard Olsen, Betül Pamuk, and Nikhil Sivadas for all the interesting discussions and supporting me over the last couple years as I finished my Ph.D.

I also thank Austin Griffith and Asha Jain for their friendship and support throughout my time in graduate school. The time we spent together was always enjoyable and provided much needed breaks from the day to day work of graduate school.

Finally, I would like to thank my parents. I would not have been able to complete my Ph.D. without their support throughout my time at Cornell.

TABLE OF CONTENTS

Biographical Sketch	iii
Acknowledgements	iv
Table of Contents	v
List of Tables	vii
List of Figures	viii
1 Introduction	1
1.1 Why study crystal structures?	1
1.2 Studying structure property relationships	1
1.3 Organization	3
2 Crystallographic tools and notation	5
2.1 Definition of a crystal structure	5
2.1.1 Space groups and Wyckoff sites	7
2.2 Reciprocal space	10
2.3 Distortions of crystal structures	12
2.4 Symmetry adapted modes	15
3 Practical Calculations	19
3.1 Density functional theory	19
3.1.1 Hubbard U	23
3.2 Implementation of density functional theory	24
3.2.1 Crystal structure optimization	27
3.2.2 Phonons	28
3.2.3 Nudged Elastic Band	29
3.3 Bond Valence Model	31
4 The crystal structure of $\text{La}_2\text{SrCr}_2\text{O}_7$	33
4.1 Introduction	33
4.2 Summary of experimental results	33
4.3 First-principles results	36
4.4 Linear correlation analysis	43
4.5 Interpretation of correlations	52
4.6 Calculation details	59
4.7 Conclusion	60
5 Antiferroelectricity in PbZrO_3	63
5.1 Introduction	63
5.2 Methods	67
5.3 Search for polar structures	68
5.4 Transition path from Pbam to $\text{I}2\text{cm}$	74
5.5 Path from Pbam to $\text{R}3\text{c}$	77
5.6 Domain boundaries in real samples	80

5.7	Domain boundaries and switching	85
5.8	Are there other low energy structures?	90
5.8.1	Free energy couplings	91
5.8.2	Structural model	92
5.8.3	Are these structures stable?	96
5.8.4	Quantifying the flatness of the energy landscape	98
5.8.5	Possible implications of structural model	103
5.9	Summary	104
6	Computational studies of Ln_2NiO_4	107
6.1	Motivation	107
6.2	Previous work on Ln_2NiO_4	108
6.3	Previous work on $Ln_2NiO_{4+\delta}$	110
6.4	Simulating excess oxygen	115
6.4.1	Generating arrangements of excess oxygen	116
6.4.2	Choice of stoichiometric structure	119
6.5	Parameters of density functional theory calculations	121
6.6	Is the charge state of excess oxygen O^{2-} ?	123
6.7	Calculation of formation energies	123
6.8	Effect of simulation cell on formation energy	124
6.9	Activation energy of ionic migration	128
6.10	Classical potentials	136
6.11	Energetics of $Pr_2NiO_{4+\delta}$ using Buckingham potentials	137
6.12	Multiple excess oxygen atoms per cell using density functional theory	138
6.13	Phonons in $Ln_2NiO_{4+\delta}$	143
6.13.1	Supercell lattice dynamics method	143
6.13.2	Demonstration of SCLD method	147
6.13.3	Analyzing individual wave vectors	151
6.13.4	Ordered and disordered excess oxygen arrangements	153
6.13.5	Phonons in $Pr_2NiO_{4.25}$	155
6.14	Raman active phonons	159
6.15	Discussion	161
7	Summary and future work	163
A	Additional polar structures in $PbZrO_3$	167
B	Unit cell relaxation in $La_2NiO_{4+\delta}$	171
	Bibliography	173

LIST OF TABLES

4.1	Possible $n=2$ Ruddlesden-Poppers structures. The tilt system follows the notation of Reference [59] which is essentially Glazer notation extended to the Ruddlesden-Poppers and uses slightly different notation. An equivalent Glazer like notation is also provided for each structure [25].	35
4.2	Symmetries of structures considered with alternate A-site orders. The La/Sr sites columns denote which La and Sr ions were swapped from their expected positions as shown in Figure 4.3. As an example the ninth row means that La4 and La8 sites were swapped with the Sr1 and Sr2 sites.	40
4.4	List of the structural features we calculated for each of our relaxed structures.	47
5.1	Calculated energy relative to the experimental Pbam ground state structure for several structures. Space group names are given using default settings and where possible alternate settings in the Pbam unit cell. The direction of the polar irrep (Γ_4^-), antiphase octahedral rotations (R_4^+), and the Σ_2 irrep are given for each structure. The modified Glazer notation [96] shows the direction of polarization and octahedral rotations. En. A and B are the energy of structure in a fixed unit cell and the fully relaxed unit cell.	70
5.2	Comparison of relaxed <i>Pbam</i> structure to the experimental structure at 10 K from Reference [97] shows excellent agreement. . . .	71
5.3	Estimated electric field strength in MV/cm required to overcome energy barriers along each transition path.	89
6.1	Parameters used in Buckingham potentials, from References [141] and [142].	137
A.1	A selection of structures found in the structure search for low energy polar structures. Every metastable polar phase found is included, while some nonpolar structures were excluded. En. A and B are the energy of structure in a fixed unit cell and the fully relaxed unit cell.	168

LIST OF FIGURES

2.1	Colored spheres represent different elements. Bonds between some elements are drawn as lines to assist with visualization. The crystal structure on the left is meant to extend out to infinity. This infinitely repeating arrangement of atoms can be represented by either of the unit cells shown, assuming periodic boundary conditions. The two unit cells differ only in visualization - the far right uses a shaded region to indicate a BX_6 octahedron instead of 6 bonds connecting B to X	6
2.2	The $n=1$ through 3 members of the Ruddlesden-Popper series. This series has chemical formula $A_{n+1}B_nX_{3n+1}$. The $n=\infty$ member of this series is the perovskite structure. The Ruddlesden-Popper series can be viewed as a periodic stacking of perovskite layers that shifts every n layers.	8
2.3	A two dimensional lattice (left) and its corresponding reciprocal lattice (right).	11
2.4	Green lines indicate the irreducible Brillouin zone of the cubic perovskite structure. Dashed lines are parallel to the reciprocal lattice vectors. The irreducible wedges extends from the origin at Γ to halfway to the next nearest reciprocal lattice point. The edges of the irreducible wedge are labeled as: Γ -M is Σ , M-X is Z, X-R is S, M-R is T, Γ -X is Δ , and Γ -R is Λ	12
2.5	The three possible kinds of octahedral rotations and their corresponding Glazer notation. From left to right: no rotations, out of phase rotations, and in phase rotations. In each case the rotation pattern is along the third crystallographic axes (out of the page).	13
2.6	Two distortions which vary by a simple oscillation. The Γ_4^- distortion moves every blue atom to the right, effectively having a spatial oscillation with zero frequency. The M_5^- distortion moves the blue atoms left or right in an alternating pattern. This M_5^- distortion is the same as the Γ_4^- distortion, but modulated by a sine wave with wave vector at M	18
3.1	The energies along an example transition path calculated using NEB. The horizontal axis is an arbitrary coordinate corresponding to distance along the transition path.	30
4.1	The expected and actual crystal structure of $\text{La}_2\text{SrCr}_2\text{O}_7$. Shaded blue regions indicate CrO_6 octahedra and red spheres are oxygen atoms. The La and Sr cations are shown as orange and green spheres. In the actual structure the La and Sr cations are disordered so their sites are colored according as a mixture of orange and green corresponding to the amount of La and Sr in a particular location.	34

4.2	An example of how disorder between the La and Sr cations was treated. The structure on the right is identical to the structure on the left except several of the La and Sr cations have switched locations.	37
4.3	Schematic labeling the A-site positions.	42
4.4	Relaxed energies per formula unit (f.u.) of 108 structures with varying La/Sr distributions with respect to the energy of the Amam reference structure with La/Sr cations on their expected sites. Color and shape of points indicate the ratio of Sr/La distribution and initial ionic positions, respectively. Note that in many cases plot symbols overlap. The horizontal axis is labeled by arbitrary structure numbers corresponding to Table 4.2. The structures are sorted by the Sr/La ratio and the mean distance between Sr cations in our relaxed Amam structure after swapping Sr/La positions, but before any further relaxation. A general tendency for energy to be lowered as the Sr cations spread out is evident.	44
4.5	Relaxed energies per formula unit (f.u.) of 108 structures with varying La/Sr distributions with respect to the energy of the Amam reference structure with La/Sr cations on their expected sites. Color and shape of points indicate the ratio of Sr/La distribution and initial ionic positions respectively. The horizontal axis is the mean distance between Sr cations in our relaxed Amam structure after swapping Sr/La positions, but before any further relaxation.	45
4.6	Linear correlation coefficients of the features listed in Table 4.4 for structures relaxed starting from A2/a ionic positions and constrained to the experimental unit cell.	50
4.7	Linear correlation coefficients of the features listed in Table 4.4 for structures relaxed starting from A2/a ionic positions with the unit cell fully relaxed.	51
4.8	Average discrepancy factor, in valence units (v.u.) of La cations in the rock salt layer and equatorial oxygen ions as a function of the average CrO ₆ distortion index with various A-site distributions. Light purple points correspond to the reference Amam structure with the expected A-site cation ordering.	53
4.9	Average maximum Cr-O bond length as a function of the average CrO ₆ distortion index with various A-site distributions. Light purple points correspond to the reference Amam structure with the expected A-site cation ordering. As the mean maximum Cr-O bond length increases, the mean CrO ₆ distortion index increases linearly. The maximum of each is reached in the Amam structure with La and Sr cations on their expected sites.	54

4.10	Average discrepancy factor of La cations in the rock salt layer and equatorial oxygen ions as a function of the average in-plane Cr-O-Cr angle with various A-site distributions. Light purple points correspond to the reference Amam structure with the expected A-site cation ordering.	57
4.11	Calculated energies relaxed structures. The zero of energy is taken as the energy of the Amam structure with ferromagnetic spin ordering. Colored points have ferromagnetic ordering, while the corresponding gray point is the energy of the same structure with antiferromagnetic ordering.	61
5.1	The polarization response to an electric field for linear dielectrics, ferroelectrics, and antiferroelectrics.	64
5.2	The crystal structure of several PbZrO ₃ phases. (a) The ground state Pbam structure. The displacements of Pb due to the Σ_2 mode are highlighted. (b) A view of the R_4^+ mode in Pbam. In Glazer notation these rotations are $a^-a^-c^0$. (c) The I2cm structure. (d) The R3c structure.	65
5.3	Group-subgroup relations between numerous relevant structures. The groups for the ground state and two candidate polar phases are shown in red boxes. The octahedral rotation pattern, polarization direction, and direction of Σ_2 allowed in each structure is given for each group. Energies are given for each group that we found a metastable structure (some structures relax into supergroups).	73
5.4	Energy and structural details of a transition path between Pbam and I2cm. The horizontal axis is a transition coordinate which merely signifies progression along the transition path. (a) Energy along transition path. (b) Amplitude of relevant distortions along the transition path.	75
5.5	Schematic of how the instability of I2cm leads to R3c. Red and blue arrows indicate the octahedral rotation axis and the polarization axis respectively. (a) Both axes are constrained along [110], giving I2cm symmetry. (b) Both axes are free to rotate along [11z], giving I1a1 symmetry. (c) Both axes are constrained along [111], giving R3c symmetry.	78
5.6	Energy and structural details of a transition path between Pbam and R3c. The horizontal axis is a transition coordinate which merely signifies progression along the transition path. (a) Energy along transition path. (b) Amplitude of relevant distortions along the transition path.	79

5.7	The displacement directions of the b planes of Pb ions are shown as arrows for several structures in the same unit cell. These structures can be labeled with a series of integers to denote the number of consecutive planes of Pb ions which displace in the same direction. (a) Pbam, (b) P2cm, (c) I2cm.	81
5.8	Diagrams of Pb displacements near an atomically sharp boundary between a domain of 2,2 displacements, which extend to the left of each diagram, and a polar domain, which extends to the right of each diagram. These are the only possible atomically sharp boundaries. A set of 3,1 displacements near the boundary is highlighted in each case. (a,b) Show the boundary with two and one antialigned Pb displacements adjacent to the polar region.	84
5.9	Space groups accessible as a function of $\Sigma_2(i, j)$. Rotating by 90 degrees in the (i, j) plane produces an equivalent structure so only the first quadrant is shown. $i=j$, $i=0$, and $i \neq j$ are shown in red, green, and blue respectively. The $i=j=0$ case is shown in orange. (a) Accessible space groups with $a^-a^-c^0$ octahedral rotations included in the structure. The ground state Pbam structure is indicated with a purple X. (b) Accessible space groups with $a^-a^-c^0$ octahedral rotations and a P_{xx0} polarization. This mimics applying an electric field along [110] to the phases shown in (a). A possible transition path from Pbam to P2cm to I2cm is shown as the purple dashed line.	86
5.10	Energy and structural details of a multistep transition path between Pbam and I2cm or R3c. The horizontal axis in each plot is a transition coordinate which merely signifies progression along the transition path. (a) Energy along the indirect transition path from Pbam to I2cm. The energy of a direct transition path is included for comparison. (b) Amplitude of relevant distortions along the indirect transition path. (c,d) Same as (a,b) except for a path from Pbam to R3c.	87
5.11	Energetics of structures with various displacement patterns. Lines are included for ease of reading but have no physical significance. Black, red, and blue points are the energy of fully relaxed, relaxed in fixed cubic unit cell, and of an unrelaxed structure generated based on the structural model.	91

5.12	Calculated energies for various elements of the structural model relative to the cubic Pbam ground state structure. From high to low energy the curves are: only Pb displacing, Pb/Zr/O displacing against each other, Pb displacing and R_4^+ , Pb/Zr/O displacing against each other and R_4^+ , full estimate of Σ_2^k and R_4^+ , full estimate of Σ_2^k and $S_4^{(1/2)-k}$ and R_4^+ , relaxed structure in fixed cubic unit cell, and the fully relaxed structure (yellow, orange, purple, green, light blue, dark blue, red, and black respectively).	94
5.13	Frequency of the most unstable phonon involving $a^0a^0c^-$ in structures with displacement pattern of the form nm . Phonon calculations were performed in unit cells equivalent to that of the fully relaxed cubic cell. The 1 displacement pattern is treated as $n = \infty$. Black line is linear fit to all data points.	98
5.14	The energies of structures with Pb/Zr/O displacing in various displacement patterns. Shaded regions in the upper plot highlight displacement patterns with effectively degenerate energies. The shaded regions each have a distinct number of domain walls per layer. The number of domain walls per layer is linearly related to the energy, as shown in the lower plot.	100
5.15	The energies of $AZrO_3$ in two kinds of unit cells. Energies are given with respect to both I2cm and Pm $\bar{3}$ m. Best fit lines are included for the 24 displacement patterns considered in each case.	102
6.1	The crystal structure of La_2NiO_4 . Green, gray and red spheres represent La, Ni and oxygen respectively. NiO_6 octahedra are shown as a shaded gray region.	109
6.2	The magnetic ordering of spins on the Ni ions in Ln_2NiO_4 . Green spheres represent La and the shaded gray regions are NiO_6 octahedron. Spins in opposite directions are shown as blue and purple arrows centered on each Ni ion. The crystal structure is identical to the $P4_2/n$ cm structure shown in Figure 6.1.	110
6.3	Example crystal structure with a single excess oxygen atom in the unit cell. Green, gray, red, and black spheres represent Ln , Ni, oxygen, and the excess oxygen. Shaded gray regions are NiO_6 octahedra. The excess oxygen atom is tetrahedrally coordinated by Ln ions. The excess oxygen atom also repels the four oxygen atoms closest to it, shown as bonds here, due to the Coulomb interaction.	112
6.4	Schematic of interstitialcy mechanism. Green, red, and black spheres represent Ln , oxygen, and the interstitial oxygen. Shaded blue regions are NiO_6 octahedra. Unoccupied interstitial sites are shown as empty squares. The interstitial oxygen takes the place of another oxygen, which simultaneously moves to an unoccupied adjacent interstitial site as indicated by arrows.	113

6.5	The primitive unit cell for an $I4/mmm$ $n=1$ Ruddlesden-Popper structure. Green, gray, red, and black spheres represent La, Ni, oxygen, and the two possible sites for excess oxygen in this unit cell respectively. NiO_6 octahedra are shown as a shaded gray region.	117
6.6	The primitive unit cell for the Cmca and $\text{P4}_2/\text{ncm}$ structures with possible interstitial sites shown. Green, gray, and red spheres represent La, Ni, oxygen. NiO_6 octahedra are shown as a shaded gray region. The possible excess oxygen sites are shown in black for Cmca and gold/purple for $\text{P4}_2/\text{ncm}$. In Cmca these sites are equivalent but in $\text{P4}_2/\text{ncm}$ these sites have two slightly different environments, and are differentiated here by color.	120
6.7	Calculated formation energies for $\text{Ln}_2\text{NiO}_{4.25}$ and $\text{Ln}_2\text{NiO}_{4.125}$. Energy is given in eV per excess oxygen atom (O_i). Excess oxygen arrangements are connected by a thin black line across the three Ln	126
6.8	Two possible unit cells for $\text{Ln}_2\text{NiO}_{4.125}$. Green, blue, red, and black spheres represent Ln , Ni, oxygen, and excess oxygen.	126
6.9	Formation energies for $\text{La}_2\text{NiO}_{4+\delta}$	127
6.10	The crystal structure in the vicinity of an excess oxygen atom and a large supercell of the lowest energy $\text{La}_2\text{NiO}_{4.125}$ structure shown in Figure 6.8. Green, blue, red, and black spheres represent La, Ni, oxygen, and the excess oxygen. Shaded regions are NiO_6 octahedra; red and blue shading indicate that an octahedron is in the upper or lower layer respectively. The opacity of each octahedron is set by how distorted an octahedron is relative to a uniform octahedron. Only two perovskite layers are shown in the supercell.	131
6.11	Migration barriers and activation energies for $\text{La}_2\text{NiO}_{4+\delta}$	132
6.12	Migration barriers and activation energies for $\text{Ln}_2\text{NiO}_{4.125}$. Black lines connect points corresponding to the lowest energy excess oxygen arrangement. Two such lines are drawn, corresponding to ionic transport along the two symmetrically distinct in plane directions.	133
6.13	Example of Ln_5O_8 polyhedron. Shaded orange and blue regions are the Ln_5O_8 polyhedra and NiO_6 octahedra. Green, red, blue, and black spheres represent Ln , oxygen, Ni, and the mobile oxygen atom. The migration barrier as a function of the Ln_5O_8 volume is also shown. Best fit lines are given for each Ln . Points shown as 'x' have unit cells which define two or more of the Ln vertices on the Ln_5O_8 polyhedron to be the same atom due to periodic boundary conditions. These points are treated as outliers and excluded from the best fit line.	135

6.14	Energies of $\text{Pr}_2\text{NiO}_{4+\delta}$ after relaxation using Buckingham pair potentials. The structure # was determined by sorting the relaxed energies. The zero of energy for each δ is taken as the lowest energy structure. Insets highlight the low energy structures.	139
6.15	Density functional theory and Coulomb energies of $\text{Pr}_2\text{NiO}_{4.25}$ with various arrangements of excess oxygen. Blue points are the energy of an arrangement combined with the I4/mmm structure before any relaxation. Red points are after relaxation. Lines connect points before and after relaxation. The plot to the right is zoomed in on the low energy relaxed structures and omits connecting lines for clarity.	140
6.16	Density functional theory and Buckingham potential energies of $\text{Pr}_2\text{NiO}_{4.25}$ with various arrangements of excess oxygen. Red '+' symbols have $N = 2$ or 4, black 'x' symbols have $N = 1$	141
6.17	The lowest energy $\text{Pr}_2\text{NiO}_{4.25}$ structure. Green, gray, red, and black spheres represent Ln, Ni, oxygen, and the excess oxygen. Shaded gray regions are NiO_6 octahedra.	142
6.18	The SCLD phonon dispersion of I4/mmm using I4/mmm as the parent structure. The standard phonon dispersion of I4/mmm is overlaid in red.	148
6.19	The SCLD phonon dispersion of $\text{P4}_2/\text{ncm}$ using $\text{P4}_2/\text{ncm}$ as the parent structure. The standard phonon dispersion of $\text{P4}_2/\text{ncm}$ is overlaid in red.	149
6.20	The SCLD phonon dispersion of $\text{P4}_2/\text{ncm}$ using I4/mmm as the parent structure. The SCLD phonon dispersion is identical to that of Figure 6.19 except it has been unfolded into the I4/mmm Brillouin zone. The standard phonon dispersion of I4/mmm is overlaid in red.	150
6.21	$Z(\mathbf{k} = X, \omega)$ for La_2NiO_4 in the I4/mmm and $\text{P4}_2/\text{ncm}$ structures, using I4/mmm as the parent structure.	152
6.22	$Z(\mathbf{k} = X, \omega)$ for La_2NiO_4 in the I4/mmm and $\text{P4}_2/\text{ncm}$ structures, using I4/mmm as the parent structure. The contribution from only oxygen ions to Z is also shown.	153
6.23	$Z(\mathbf{k} = M, \omega)$ for several $\text{Pr}_2\text{NiO}_{4.25}$ structures using $\text{P4}_2/\text{ncm}$ as the parent structure. The black line is for a structure with a fully ordered arrangement of excess oxygen. Colored lines correspond to several random arrangements of excess oxygen.	154
6.24	The averaged SCLD phonon dispersion of 23 $\text{Pr}_2\text{NiO}_{4.25}$ structures using $\text{P4}_2/\text{ncm}$ as the parent structure. The standard phonon dispersion of $\text{P4}_2/\text{ncm}$ is overlaid in red.	156
6.25	$Z(\mathbf{k} = M, \omega)$ and contributions to it from each element as calculated in a low energy $\text{Pr}_2\text{NiO}_{4.25}$ structure as a function of b . A peak around 75 cm^{-1} splits and shifts, as signified by arrows.	158

6.26	Frequency of the highest frequency phonon involving mostly the Γ_5^+ irrep as defined with respect to $P4_2/nm$ (the X_1^+ irrep with respect to $I4/mmm$) for several structures. Red '+' symbols are relaxed $\text{Pr}_2\text{NiO}_{4+\delta}$ structures commensurate with the X point of $I4/mmm$. Black 'x' symbols are the $P4_2/nm$ structure doped with holes corresponding to two holes per excess oxygen atom (2δ).	161
B.1	Formation energies of $\text{La}_2\text{NiO}_{4+\delta}$ calculated in fully relaxed unit cells compared with the energy in a corresponding unit cell constrained to the $I4/mmm$ lattice.	172
B.2	Migration barriers of $\text{La}_2\text{NiO}_{4.125}$ calculated in fully relaxed unit cells compared with the energy in a corresponding unit cell constrained to the $I4/mmm$ lattice.	172

CHAPTER 1

INTRODUCTION

1.1 Why study crystal structures?

Many useful devices ranging from semiconductors used in transistors [1, 2] to simple metals used to conduct electricity [3] to ferromagnets used in memory devices [4], are made of crystalline materials. The crystal structure of these materials often plays a critical role in determining the properties of the material. As an example of this, consider pure carbon which can form diamond, graphite, or graphene. Diamond is one of the hardest known materials while graphite is very soft and can be used for writing on paper. Graphene is a two dimensional material with a wide range of special electrical properties. It has been shown that by stacking layers of graphene on top of each other at various angles, the material can behave as an insulator or a superconductor [5]. The difference among these materials is the arrangement of carbon atoms, that is, the crystal structure.

1.2 Studying structure property relationships

Several questions related to crystal structure are relevant to the design of a new material with a desired property. As a demonstration of this process, these questions are discussed within the context of materials which exhibit ferroelectricity. Ferroelectricity has been extensively studied, though there is ongoing research in this field, and each of these questions has been addressed to some extent.

First, what is the fundamental mechanism which enables the property? For a material to exhibit ferroelectricity it must have a polar crystal structure and the polarization must be switchable using an electric field. A crystal structure with inversion symmetry (meaning inverting the crystal structure about a point leaves it unchanged) cannot be polar, so breaking inversion symmetry is critical for a material to exhibit ferroelectricity.

Second, what generally causes a material to possess this fundamental mechanism? Generally for inversion symmetry to be broken, the atoms in a crystal structure must displace away from some high symmetry positions. These displacements can happen due to bonding preferences of the atoms in the crystal structure or be induced via coupling to other distortions of crystal structure [6, 7].

Third, which specific materials and crystal structures will possess this fundamental mechanism? Part of addressing this question is assessing how strong the desired property in a material will be. In a ferroelectric this could be how large the polarization is. Various mechanisms are known to cause atoms to displace from high symmetry positions. A mismatch in the size of ionic nuclei relative to the space around it can lead to a polar structure. Ions which have active electronic lone pairs are also well known to displace away from high symmetry positions. Crystal structures specifically designed layer by layer can lead to a polarization via couplings between distortions in the crystal structure [8].

Finally, how can these specific materials be synthesized? In some cases a new material can be made using standard solid state chemical reactions. In other cases the desired crystal structure is inherently metastable and must be stabilized using special growth techniques, such as molecular beam epitaxy.

In practice these questions are not always addressed sequentially. The process may be iterated as new information is found or new mechanisms are discovered.

1.3 Organization

The research described in this dissertation focuses on understanding the first and second questions for several classes of materials. Before describing these studies two introductory chapters are given. Chapter 2 will provide a formal definition of crystal structure and discusses how crystal structures can be quantified and studied. Chapter 3 discusses density functional theory, the method used for accurately simulating a crystal structure, as well as some of the practical considerations when simulating a crystal structure. These two chapters are intended to provide a minimal introduction to crystal structures and density functional theory. Further details in these areas can be found in various standard texts [3, 9, 10, 11, 12, 13, 14, 15, 16]

Chapter 4 describes the mechanisms leading to a never before seen and unexpected crystal structure of $\text{La}_2\text{SrCr}_2\text{O}_7$, which was synthesized prior to this study. This material was studied to determine why it formed in an unexpected crystal structure. Understanding an unexpected result helps improve chemical intuition about materials and can ultimately prove useful in future research. In this case, by determining why $\text{La}_2\text{SrCr}_2\text{O}_7$ adopts a novel crystal structure, a coupling between *A*-site disorder, *B*-site chemistry and octahedral rotations was discovered. This coupling provides a route towards controlling similar crystal structures and could conceivably be used to design new ferroelectrics.

Chapter 5 discusses the fundamental mechanism which leads to antiferroelectricity in PbZrO_3 . Antiferroelectrics can be used as actuators or high energy capacitors but the toxicity of Pb in most known antiferroelectrics is undesirable. Therefore being able to design new antiferroelectrics, which do not contain Pb, is desirable. This study focused on determining what makes a material exhibit antiferroelectricity - a question that has remain unsolved for more than 50 years. While not completely resolved, significant progress has been made and several directions for future research into this area have been identified, including some ideas on how new antiferroelectrics may be found.

Chapter 6 describes the crystal structure of $\text{Ln}_2\text{NiO}_{4+\delta}$ in detail. This class of materials is a candidate for use as a cathode in a solid oxide fuel cell, but currently requires an operating temperature too high for practical use. By gaining insight into the crystal structure of Ln_2NiO_4 , the ultimate goal is to design a new material which would require a lower operating temperature by decreasing the activation energy of ionic migration. This study provides a systematic method for studying the arrangement of excess oxygen atoms and shows that these arrangements have a strong effect on properties - including the activation energy. This study demonstrated that the arrangement of excess oxygen, which has previously been mostly neglected, is important to consider when simulating these materials. This idea suggests another iteration through the series of questions above may be needed to properly understand all the properties of $\text{Ln}_2\text{NiO}_{4+\delta}$. Phonon broadening as a function of the excess oxygen arrangement was also considered and may be useful for interpreting experimentally measured phonon dispersions.

CHAPTER 2

CRYSTALLOGRAPHIC TOOLS AND NOTATION

A crystalline material is comprised of a large number of atoms. In an ideal crystal the position of these atoms follow a perfectly periodic pattern, meaning the atoms exhibit translational symmetry. This perfect periodicity is broken by thermal fluctuations which cause the atoms to vibrate around a central position. These fluctuations do not change the average position of atoms - unless otherwise specified any reference to the position of an atom will ignore these thermal fluctuations and refer to the average central position. In an actual crystal there will also be various defects, such as missing or extra atoms, caused by entropy. If these defects occur relatively infrequently within a crystal, they can be ignored as a first approximation. This is not always the case - Chapter 6 will discuss a material in which defects are the primary subject of interest.

This chapter will discuss crystal structures under the simplifying assumption that there is no disorder or defects in the structure. Many crystallographic tools also make this assumption and their generalization to handle crystal structures with disorder is an active field of research [17]. While much of the research presented in this dissertation deals with some form of disorder, the crystallographic tools used to understand ordered structures are still useful.

2.1 Definition of a crystal structure

A crystal structure can be represented using a unit cell and periodic boundary conditions. This formally treats the crystal structure as an infinitely repeating arrangement of atoms with translational symmetry. Doing so is a reasonable ap-

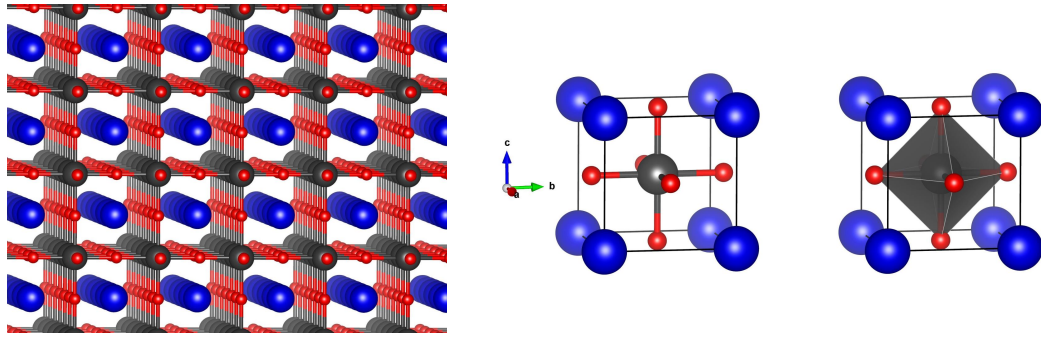


Figure 2.1: Colored spheres represent different elements. Bonds between some elements are drawn as lines to assist with visualization. The crystal structure on the left is meant to extend out to infinity. This infinitely repeating arrangement of atoms can be represented by either of the unit cells shown, assuming periodic boundary conditions. The two unit cells differ only in visualization - the far right uses a shaded region to indicate a BX_6 octahedron instead of 6 bonds connecting B to X .

proximation for a crystalline sample which may be several centimeters in size while the distance between atoms is only several hundred picometers. In other words there is a very large number of atoms (roughly 10^8) that follow a periodic placement in space before the edge of the crystal is reached. A depiction of how a crystal structure can be represented by a unit cell and periodic boundary conditions is shown in Figure 2.1. These images, as well as many other images of crystal structures in this dissertation were made using VESTA [18].

The unit cell used to represent a crystal structure can be specified using three vectors, which are referred to as lattice vectors. This is convenient when specifying a crystal structure within a specific set of Cartesian axes as is often done when simulating the properties of a crystal structure on a computer. Rotating the entire crystal structure does not change it so the unit cell could also be specified with only the lengths and angles between these three vectors. This set of

six numbers is the minimum needed to fully specify the unit cell for a crystal structure and is also frequently used. The three lattice vectors are commonly referred to as **a**, **b** and **c**.

Two types of crystal structure have been considered in this work and will be discussed extensively: perovskites and the Ruddlesden-Popper series. Several Ruddlesden-Popper's and the perovskite structure are shown in Figure 2.2. These names refer to a class of structures which allow many possible crystal structures. For example, many perovskite structures have orthorhombic unit cells rather than the cubic unit cell shown in Figure 2.2. These structures are still referred to as perovskites because the arrangement of atoms remains very similar to the cubic case. A more specific system is therefore needed to uniquely label crystal structures.

2.1.1 Space groups and Wyckoff sites

Symmetry may be used to generate a more meaningful label for a crystal structure. This can be done using the symmetry group of the structure, which is the group of symmetry operators that do not alter the crystal structure. These groups are known as space groups and the 230 possible groups in three dimensions have been enumerated [9]. These groups have labels which specify the symmetry operators in the group, for example *Imma*. The *I* indicates the unit cell used is body centered, the two *m*'s indicate mirror planes exist along the first and second lattice vector, and the *a* indicates a glide plane along the first lattice vector perpendicular to the third lattice vector. A detailed description of these labels can be found in Reference [9].

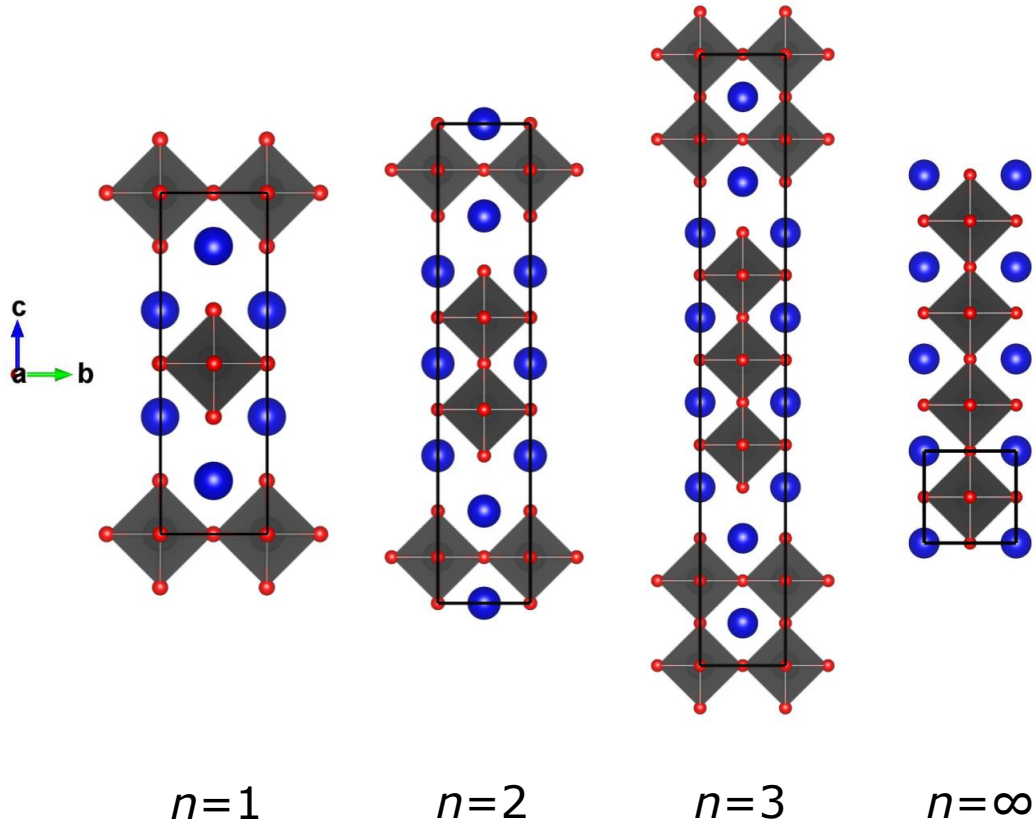


Figure 2.2: The $n=1$ through 3 members of the Ruddlesden-Popper series. This series has chemical formula $A_{n+1}B_nX_{3n+1}$. The $n=\infty$ member of this series is the perovskite structure. The Ruddlesden-Popper series can be viewed as a periodic stacking of perovskite layers that shifts every n layers.

The space group name is often used to refer to a particular crystal structure and given context, is usually sufficient to identify a crystal structure. Space group names, however, do not uniquely label a crystal structure. This must be the case as space group depends only on symmetry - any parameters, such as the shape of the unit cell or other internal degrees of freedom are not specified by space group. Further, it is possible for two crystal structures to belong to the same space group yet have structures that cannot be equivalent re-

ardless of changes to the various allowed degrees of freedom. This occurs in the Ruddlesden-Popper series for different n - in each case the space group is $I4/mmm$ but the structures are clearly distinct. These structures differ in symmetry by the spatial frequency of mirror planes perpendicular to the vertical axis. Each structure has this mirror plane symmetry but the number of symmetrically distinct atoms in each structure is different. To fully specify a crystal structure it is therefore necessary to specify all symmetry allowed degrees of freedom in the structure. The shape and size of the unit cell can be specified using three lengths and three angles, as discussed above.

Two methods are commonly used to specify the internal degrees of freedom in a crystal structure. The first is to simply list the position of every atom within a unit cell. This method is convenient for performing simulations or whenever a real space picture of the crystal structure is required. Alternatively, a single position can be specified for each set of symmetrically equivalent atoms.

A set of symmetrically equivalent atoms in a crystal structure are said to occupy a particular Wyckoff position. The complete set of allowed Wyckoff positions for each space group is enumerated in Reference [9]. Many Wyckoff positions do not allow any motion of the atoms, for instance an atom sitting on inversion center cannot move in any direction without breaking the symmetry of the crystal structure. Each space group allows a general position, meaning a position of no particular symmetry, which allows atoms on this position to move in concert with other equivalent atoms occupying this Wyckoff position so that the symmetry of the particular space group is not broken. It is also possible for a Wyckoff position to allow one or two degrees of freedom - an atom may be free to move along z but not x or y . When specifying a crystal structure using

Wyckoff positions, only the type of position (listed as the number of equivalent atoms on the position and a letter labeling the position, for example 3c) and any allowed degrees of freedom are given. This provides the minimum amount of information to completely and uniquely specify a the crystal structure.

Programs exist which take a unit cell and a list of atomic positions as input and determine the space group and occupied Wyckoff orbits. This kind of tool can be used to verify that a crystal structure being studied has the symmetry one expects, which is important to verify when dealing with complicated structures. The *FINDSYM* program [19] was used for this purpose throughout this work.

2.2 Reciprocal space

The periodic nature of crystal structures naturally lends itself to Fourier analysis. Any spatially dependent property of the crystal will be periodic in real space, and can thus be represented by a simple Fourier series with spatial frequencies that fall on a specific set of lattice points. This set of points is known as the reciprocal lattice. If the lattice vectors that represent a crystal structure in real space are \mathbf{a}_1 , \mathbf{a}_2 , and \mathbf{a}_3 , then the set of reciprocal lattice vectors which define the reciprocal lattice are

$$\mathbf{b}_1 = \frac{1}{\Omega} \mathbf{a}_2 \times \mathbf{a}_3 \quad (2.1)$$

$$\mathbf{b}_2 = \frac{1}{\Omega} \mathbf{a}_3 \times \mathbf{a}_1 \quad (2.2)$$

$$\mathbf{b}_3 = \frac{1}{\Omega} \mathbf{a}_1 \times \mathbf{a}_2 \quad (2.3)$$

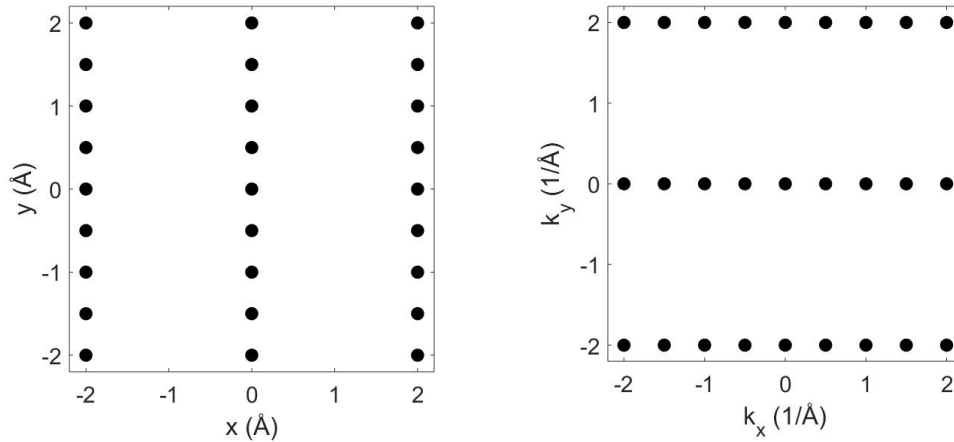


Figure 2.3: A two dimensional lattice (left) and its corresponding reciprocal lattice (right).

where $\Omega = \mathbf{a}_1 \cdot (\mathbf{a}_2 \times \mathbf{a}_3)$. A depiction of a simple two dimensional rectangular lattice with its corresponding reciprocal lattice is shown in Figure 2.3. An arbitrary point in reciprocal is usually referred to as wave vector \mathbf{k} and corresponds to periodic oscillations in real space as defined by a Fourier transform.

When computing the properties of a crystal structure it often necessary to integrate various quantities over reciprocal space. For example, the energy of the electronic band structure is determined by an integral over the electronic energy eigenstates. The limits of the integral are set by the Brillouin zone, which is defined as the region in reciprocal space closest to a particular point on the reciprocal lattice. Symmetry can be used to reduce the Brillouin zone into an irreducible wedge. The value of any quantity anywhere in reciprocal space can then be determined using values from the irreducible wedge. More details on reciprocal space and Brillouin zones can be found in these texts [3, 11, 10].

Points of special symmetry in the irreducible wedge are given special labels. The origin is always labeled as Γ , while other points are labeled depending on

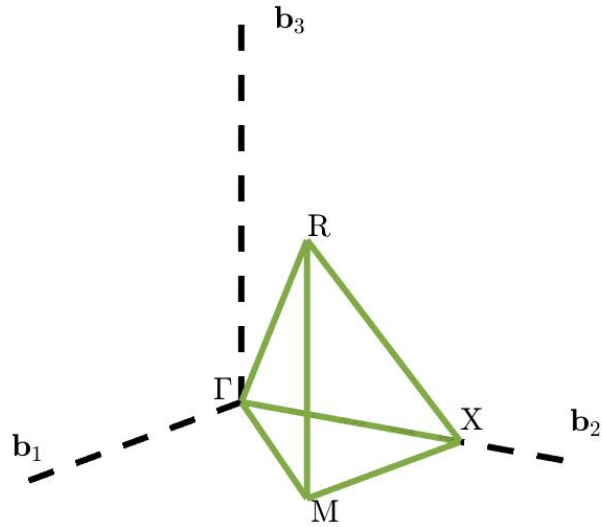


Figure 2.4: Green lines indicate the irreducible Brillouin zone of the cubic perovskite structure. Dashed lines are parallel to the reciprocal lattice vectors. The irreducible wedge extends from the origin at Γ to halfway to the next nearest reciprocal lattice point. The edges of the irreducible wedge are labeled as: Γ -M is Σ , M-X is Z, X-R is S, M-R is T, Γ -X is Δ , and Γ -R is Λ .

the symmetry of the crystal structure. These labels can be obtained from online tools [20] and are enumerated in tables [14]. The irreducible wedge of the cubic perovskite structure is shown in Figure 2.4.

2.3 Distortions of crystal structures

Small changes in a crystal structure can produce large changes in the macroscopic properties of the crystal. A well known example of this is the rare-earth nickelate perovskites ($R\text{NiO}_3$). Depending on the rare-earth cation, the material can behave as a metal or an insulator. Various studies have shown that the tran-

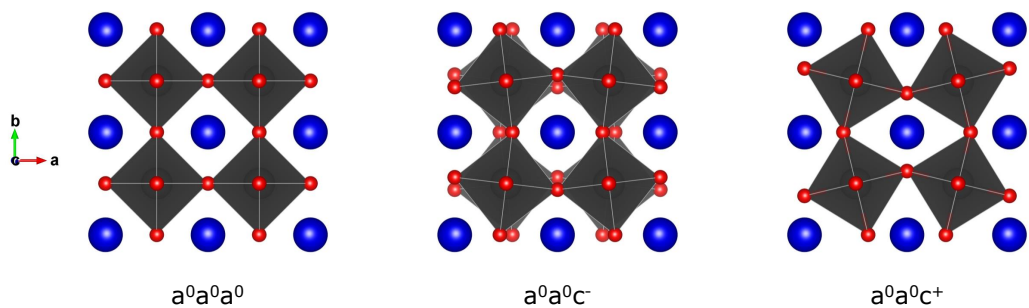


Figure 2.5: The three possible kinds of octahedral rotations and their corresponding Glazer notation. From left to right: no rotations, out of phase rotations, and in phase rotations. In each case the rotation pattern is along the third crystallographic axes (out of the page).

sition between metal and insulator occurs simultaneously with a change in the crystal structure. The mechanism driving the transition between metal and insulator is still being studied but seems related to a change in the rotation angle of the NiO_6 octahedron [21, 22, 23, 24].

The perovskite crystal structure is commonly observed with various patterns of octahedral rotations. These patterns can be labeled using Glazer notation [25]. The notation uses superscripts to denote the kind of rotation pattern about each crystallographic axis and letters to specify which axes are equivalent. When there are no rotations about an axis, it has a superscript of 0, in phase rotations are labeled with a +, and out of phase rotations are labeled with a -. Images of in and out of phase rotations are shown in Figure 2.5. When two letters are the same, it means the rotation amplitude about those two axes are equivalent. For instance, the $a^-a^-c^+$ pattern refers to an equal amplitude of out of phase rotations about the first and second crystallographic axes and in phase rotations about the third axis.

Octahedral rotations, as well as other kinds of crystal structure distortions, are observed in many perovskites and Ruddlesden-Poppers. These distortions tend to be absent at higher temperature (they may be present as fluctuations, but do not order over long range) and are frozen in to the structure as temperature is lowered. It is common to observe a sequence of transitions in which the crystal structure changes several times with temperature. In such cases there are usually several crystal structures which have similar energies (the lowest of which is observed in experiment). To study materials like this it is beneficial to consider a reference crystal structure.

Every perovskite crystal structure can be interpreted as the cubic structure shown in Figure 2.1 plus some set of distortions, making it a natural choice for a reference structure. Using it as a reference structure ensures that whichever distortions are considered are relatively small and can be labeled using a consistent language, for instance Glazer notation. Changes relative to the reference structure of various properties (energy, polarization, etc) can be calculated rather than an absolute value. This increases the accuracy of the calculations due to cancellation of error in the calculations - any errors calculated in the reference structure are usually similarly erroneous in slightly distorted structures.

The distorted structures shown in Figure 2.5 cannot be specified in the cubic perovskite unit cell shown in Figure 2.1. This is because the distortions, in this case octahedral rotations, have a repeat period twice as long as the cubic crystal structure. This apparent problem is resolved by artificially doubling the size of the cubic perovskite cell so that the distortions are commensurate with the enlarged unit cell. The enlarged unit cell is called a supercell. Supercells are frequently used when studying crystal structures because many distortions of

interest are not commensurate with the unit cell of the reference structure.

When using a supercell, the Brillouin zone is effectively folded back onto itself. This means certain points in reciprocal space are folded back to the origin, Γ , meaning those points are commensurate with the supercell. In other words, oscillations with periodicity corresponding to the wave vector \mathbf{k} which was folded back to Γ can be represented in the supercell.

As an example, a one dimensional crystal structure with lattice vector $\mathbf{a} = 4\hat{x}$ has reciprocal lattice vector¹ $\mathbf{b} = \frac{1}{4}\hat{x}$. The point $\frac{1}{4}\hat{x}$ in reciprocal space is thus equivalent to the origin because of the periodic nature of reciprocal space. Representing the same crystal structure in a supercell with lattice vector $\mathbf{a}_{\text{super}} = 8\hat{x}$ makes the reciprocal lattice become $\mathbf{b}_{\text{super}} = \frac{1}{8}\hat{x}$ and now the point $\frac{1}{8}\hat{x}$ becomes equivalent to the origin. This means oscillations associated with $\mathbf{k} = \frac{1}{8}\hat{x}$, that is oscillations with period of $8\hat{x}$, can be represented in the supercell which is exactly what one would expect based on the real space lattice vectors. For a three dimensional crystal structure with non orthogonal lattice vectors the details become more complicated but follow the same mathematical rules.

2.4 Symmetry adapted modes

For a crystal structure with N atoms in its unit cell there are in general $3N$ possible degrees of freedom corresponding to each atom moving along one of the three Cartesian directions. This xyz basis is easy to write down but is not a convenient basis to work in - moving a single atom along a Cartesian axis of-

¹Sometimes a factor of 2π is included in the reciprocal lattice vectors. This choice is arbitrary and depends on the Fourier transform convention being used.

ten breaks several symmetries simultaneously. A better basis to work in would have each degree of freedom remove a minimal set of symmetry operators at once. This basis can be constructed for any crystal structure and the distortions are known as symmetry adapted modes.

The symmetry adapted modes are orthogonal and form a complete basis, that is they span the $3N$ degrees allowed in the crystal structure [26]. Each symmetry adapted mode is associated with a particular irreducible representation (irrep) of the allowed distortion space [27]. Irreps can be labeled using several notations but follow the basic form X_5^+ [13, 28]. The X part of the label indicates the point in reciprocal space the distortion belongs to. The number in the subscript is an arbitrary label that has been defined historically [12]. The superscript can be either + or - which indicates the parity of the irrep. In cases when the irrep has neither even nor odd parity the superscript is omitted. A detailed explanation of the group theoretical definition of these modes can be found in [12].

The symmetry adapted modes can be viewed as order parameters and allow a Taylor series expansion of the crystal structures properties, particularly its energy, about the reference structure [29]. Due to the orthogonality of these modes, such an expansion is decoupled to second order. Assuming the expansion is made about a saddle point this means an energy expansion will look like

$$E = E_0 + \sum_i c_i Q_i^2 + \sum_{ijk} c_{ijk} Q_i Q_j Q_k + \sum_{ijkl} c_{ijkl} Q_i Q_j Q_k Q_l + \text{higher order terms} \quad (2.4)$$

where the sums run over all irreps, Q_i is the amplitude of the i^{th} irrep, and c_i is a coefficient in the expansion. In general c_i is not zero for any irrep. Many of the higher order coefficients are zero by symmetry, for example c_{ijk} is only allowed

to be nonzero for specific sets of irreps. The allowed nonzero coefficients in this expansion can be found by finding polynomials of the irreps which are left invariant under the symmetry operators of the crystal structure under consideration. The online program *INVARIANTS* [30] provides a simple way to find the allowed nonzero coefficients.

Symmetry adapted modes also provide a convenient way to compare structures. The total change between a high and low symmetry structure can be quantified by calculating the amplitude of each symmetry adapted mode in the low the symmetry structure. The amplitude of these modes can be compared across various structures to gain insight into what may drive phase transitions in a material.

Symmetry adapted modes can be viewed as a distortion modulated by a wave vector in reciprocal space. That is if a symmetry adapted mode, say Γ_4^- of the cubic perovskite structure, is defined in a unit cell, there will be a symmetry mode at other wave vectors \mathbf{k} that are the Γ_4^- distortion modulated by $\exp(2\pi i \mathbf{k} \cdot \mathbf{R})$ where \mathbf{R} is a vector pointing at a particular primitive unit cell of the supercell (ie pointing at one of the duplicated unit cells in the supercell). At the M point of the cubic perovskite, Γ_4^- becomes the M_5^- mode, which has $\mathbf{k} = [\frac{1}{2}, \frac{1}{2}, 0]$. The difference in these two distortions is shown in Figure 2.6.

Symmetry adapted modes can be obtained from several online tools, such as *ISODISTORT* [27] or *AMPLIMODES* [31, 32]. *ISODISTORT* was used throughout this work to define symmetry adapted modes and calculate their amplitudes. By default, this tool does not output a complete basis set of symmetry adapted modes. An in house tool was developed to force *ISODISTORT* to print out a complete basis set and manipulate it into a single matrix that can be used

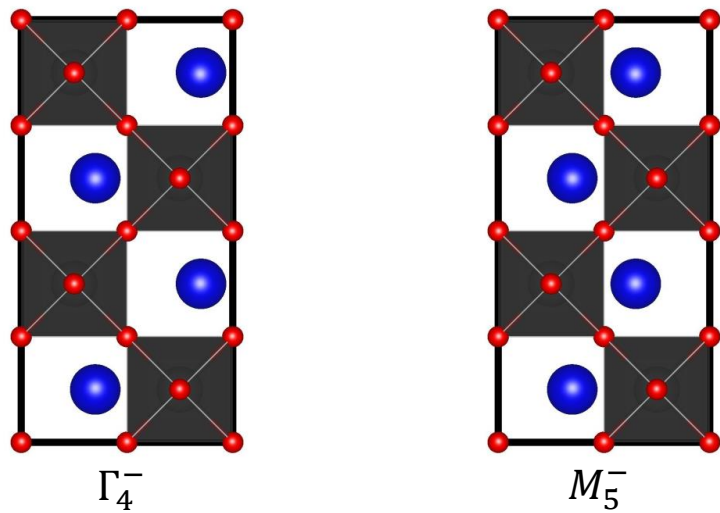


Figure 2.6: Two distortions which vary by a simple oscillation. The Γ_4^- distortion moves every blue atom to the right, effectively having a spatial oscillation with zero frequency. The M_5^- distortion moves the blue atoms left or right in an alternating pattern. This M_5^- distortion is the same as the Γ_4^- distortion, but modulated by a sine wave with wave vector at M .

offline. This allows the amplitude of each mode in a structure to be easily calculated without having to repeatedly use the web based tool. It further allows, for instance, an automated determination of irreps for each eigenmode of the dynamical matrix of a crystal structure which would be extremely tedious to perform manually using the web based tool.

CHAPTER 3

PRACTICAL CALCULATIONS

The work described in this dissertation used several computational tools to study crystal structures. The primary method, density functional theory, is described in Section 3.1 and the implementation of this theory is described in Section 3.2. This theory allows the energy of a crystal structure as well as the force on each atom in a crystal structure to be calculated. With this information it is possible to perform various computational experiments to extract information about a material and its possible crystal structures. Quantitative chemical bonding information for a crystal structure can be calculated using the Bond Valence Model, as described in Section 3.3.

3.1 Density functional theory

The explanation of density functional theory presented here follows the derivation in Reference [16]. There are many other texts which cover this subject, including Reference [15].

The Hamiltonian for a crystal structure can be written as

$$\begin{aligned}
 H = & \sum_{i=1}^N \frac{p_i^2}{2m} + \frac{1}{4\pi\epsilon_0} \frac{1}{2} \sum_{i,j=1;i \neq j}^N \frac{e^2}{|\mathbf{r}_i - \mathbf{r}_j|} - \frac{1}{4\pi\epsilon_0} \sum_{n=1}^K \sum_{i=1}^N \frac{Z_n e^2}{|\mathbf{r}_i - \mathbf{R}_n|} \\
 & + \sum_{n=1}^K \frac{p_n^2}{2M_n} + \frac{1}{4\pi\epsilon_0} \frac{1}{2} \sum_{n,n'=1;n \neq n'}^K \frac{Z_n Z_{n'} e^2}{|\mathbf{R}_n - \mathbf{R}_{n'}|}
 \end{aligned} \tag{3.1}$$

where i and n index electrons and atomic nuclei, p is momentum, m is the mass of an electron, M_n is the mass of the n^{th} nuclei, e is the charge of an electron, $Z_n e$ is the charge of the n^{th} nuclei, \mathbf{r} is the position of an electron, and \mathbf{R} is the position of a nuclei [16]. The terms in this equation correspond to the kinetic energy

of electrons, the Coulomb interaction between pairs of electrons, the Coulomb interaction between electrons and nuclei, the kinetic energy of nuclei, and the Coulomb interaction between pairs of nuclei. This Hamiltonian is far too complicated to solve directly, mainly due to the Coulomb interactions that couple each electron or nuclei in the crystal to every other electron or nuclei.

As a first step towards simplifying Equation 3.1, the Born-Oppenheimer approximation is used [33]. This approximation assumes that the nuclei in a crystal move so much slower than the electrons that the nuclei can be treated as stationary. The nuclei move slower because each proton or neutron, of which there can be many in a nuclei, has a mass more than 1800 times as large as an electron [16]. By applying this approximation, the terms involving only the nuclei in Equation 3.1 can be evaluated separately by assuming the nuclei are in a fixed position. After doing so, the remainder of the Hamiltonian is [16]

$$H = \sum_{i=1}^N \frac{p_i^2}{2m} + \frac{1}{4\pi\epsilon_0} \frac{1}{2} \sum_{i,j=1;i \neq j}^N \frac{e^2}{|\mathbf{r}_i - \mathbf{r}_j|} - \frac{1}{4\pi\epsilon_0} \sum_{n=1}^K \sum_{i=1}^N \frac{Z_n e^2}{|\mathbf{r}_i - \mathbf{R}_n|} \quad (3.2)$$

At this point it is convenient to rewrite the Hamiltonian of Equation 3.2 in the atomic unit system which brings all the constants in this equation to roughly order 1. The Coulomb interaction between electrons and nuclei is also rewritten as a function V_{ext} which depends on the fixed positions of nuclei as well as the position of electrons. After doing so, the Hamiltonian becomes [16]

$$H = \sum_{i=1}^N \left[-\frac{1}{2} \nabla_i^2 + V_{\text{ext}}(\mathbf{r}_i) \right] + \frac{1}{2} \sum_{i,j=1;i \neq j}^N \frac{1}{|\mathbf{r}_i - \mathbf{r}_j|} \quad (3.3)$$

While Equation 3.1 has been simplified somewhat to get to Equation 3.3, the Coulomb interaction between pairs of electrons is still not feasible to evaluate exactly for more than a few electrons. Further progress is made possible by

the first Hohenberg-Kohn theorem [34, 35] which proves that the lowest energy solution to this Hamiltonian is uniquely defined by a functional of the electron density [15]. In equation form this means a unique energy functional E exists:

$$E[n] = \min \langle \Psi | H | \Psi \rangle \quad (3.4)$$

where n is the electron density and Ψ is a many electron wave function solution to the Hamiltonian of Equation 3.3 [16]. The total number of electrons represented by n is required to be the total number of electrons, N . The form of the functional E is not known, but it can be written as follows

$$E[n] = T[n] + \int V_{\text{ext}}(\mathbf{r})n(\mathbf{r})d^3\mathbf{r} + \int \int \frac{n(\mathbf{r})n'(\mathbf{r}')}{|\mathbf{r} - \mathbf{r}'|}d^3\mathbf{r}d^3\mathbf{r}' + E_{\text{XC}}[n] \quad (3.5)$$

$T[n]$ is a functional representing the kinetic energy of a noninteracting electron gas, that is a set of electrons which behave entirely independently of each other. $E_{\text{XC}}[n]$ is called the exchange correlation functional and is defined as including everything that is not included in the rest of Equation 3.5. The exact form of this functional is unknown so it must be approximated, as will be discussed below. The expression for $E[n]$ gives the minimum energy of a system so it must be stable with respect to a variation in n . Taking a functional derivative and finding stable solutions leads to the Kohn-Sham equations [36, 16]

$$\left[-\frac{1}{2}\nabla^2 + V_{\text{ext}}(\mathbf{r}) + \frac{\delta E_{\text{XC}}[n]}{\delta n(\mathbf{r})} + \int \frac{n(\mathbf{r}')}{|\mathbf{r} - \mathbf{r}'|} \right] \psi_k(\mathbf{r}) = \varepsilon_k \psi_k(\mathbf{r}) \quad (3.6)$$

Equation 3.6 is similar to the usual Schrodinger equation for a single particle, except it has an effective potential which depends on the electron density. Solving this equation requires an iterative approach because the effective potential depends on n . Starting from an arbitrary n , the corresponding ψ_k is calculated and used to update n . This is repeated until the density n does not change sig-

nificantly between iterations. The total energy of the system is then [36, 16]

$$E = \sum_{k=1}^N \varepsilon_k - \frac{1}{2} \int \int \frac{n(\mathbf{r})n'(\mathbf{r}')}{|\mathbf{r} - \mathbf{r}'|} d^3\mathbf{r}d^3\mathbf{r}' + E_{\text{XC}}[n] - \int V_{\text{XC}}[n(\mathbf{r})]n(\mathbf{r})d^3\mathbf{r} \quad (3.7)$$

An important result due to Hohenberg and Kohn is that the electron density which minimizes the energy in Equation 3.7 corresponds to the actual electron density that would be obtained from solving the full Schrodinger equation [34]. This means the electron density can be solved for using a variational approach to minimize the energy [15].

The energy functional in Equation 3.5 is written in a way that separates known contributions to the energy (the kinetic energy of noninteracting electrons and most of the Coulomb energy) from the contributions in $E_{\text{XC}}[n]$ which are not known exactly. $E_{\text{XC}}[n]$ is called the exchange correlation functional because it accounts for the exchange interaction, arising from the electrons being indistinguishable fermions, and correlation which is due to interactions between electrons. In comparison to the kinetic energy and Coulomb terms already accounted for it is relatively small, suggesting that some approximation to this functional may yield good results.

The simplest approximation to $E_{\text{XC}}[n]$ is known as the local density approximation (LDA). The LDA takes advantage of the fact that the form of $E_{\text{XC}}[n]$ is known exactly for a uniform electron gas. At any point in space $E_{\text{XC}}^{\text{LDA}}[n]$ follows the form of the uniform electron gas for a given n [15]. The assumption that the energy depends only on the local electron density is what gives the LDA its name. Another class of exchange correlation functionals follow the generalized gradient approximation (GGA). In this case, the spatial derivative of the electron density is also included in the functional. There is not a unique way to do

this and many functionals have been made using the GGA [15] including those described in References [37] and [38].

Density functional theory only guarantees the ground state energy is calculated correctly. This effectively means it is a zero temperature theory, so that entropy is ignored. It also means that while unoccupied electronic states are calculated when solving Equation 3.6, they are not guaranteed to be correct. In practice they usually bear some resemblance to reality but are not perfect - for instance the electronic bandgap is usually underestimated. Despite these discrepancies, it is possible to calculate changes in something like the electronic bandgap correctly due to error cancellation.

3.1.1 Hubbard U

The LDA and GGA are known to be insufficient for describing the onsite Coulomb repulsion between electrons localized on an atom. This is part of the reason electronic bandgaps are underestimated and can cause materials which should be insulating to become erroneously metallic within density functional theory. One solution to this issue is to artificially increase the Coulomb repulsion for electrons occupying a particular electron shell. This is referred to as adding a Hubbard U or DFT+ U . The total energy within this approach is the DFT energy plus an additional term

$$E_{\text{DFT}+U} = E_{\text{DFT}} + \frac{U}{2} \left[\sum_{\sigma,j} \rho_{jj}^{\sigma} - \sum_{\sigma,j,l} \rho_{jl}^{\sigma} \rho_{lj}^{\sigma} \right] \quad (3.8)$$

where ρ specifies the number of electrons occupying a specific set electron shell [39, 40]. The value of U can qualitatively change the properties of a material, for instance from metallic to insulating or ferromagnetic to antiferromagnetic.

While methods exist to calculate an appropriate value of U for use in a particular material, they will not be used here [41, 42]. Rather it will be used as an empirical parameter and only when it is well known to be needed. Further, the exact value of U does not qualitatively effect the results discussed in this dissertation. This was checked by varying U over some range to ensure that the main results are not significantly altered. Essentially, DFT+ U was used to bring the strength of Coulomb repulsion on certain atoms closer to what it should be and as long as the value of U is within a reasonable range the properties of the material do not change significantly.

3.2 Implementation of density functional theory

The Vienna Ab initio Simulation Package (VASP) implements density functional theory and was used for all of the density functional theory results presented in this dissertation [43, 44, 45]. The package is still being actively developed and improved by a research group and the full details of its implementation are beyond the scope of this dissertation. However, there are several details that warrant some explanation here.

VASP uses plane waves to represent quantities such as the charge density. Plane waves form a convenient basis set for representing an arbitrary function subject to periodic boundary conditions and are thus a natural choice for studying crystalline materials. Within VASP the set of plane waves is set by specifying a maximum energy cutoff for the plane waves, or equivalently a maximum wave vector. In practice the number of plane waves used must be carefully determined on a case by case basis. This is done by converging a calculated prop-

erty with respect to the energy cutoff - higher energy cutoffs should give more accurate results and for a large enough cutoff there shouldn't be any significant change in calculated properties. Owing to the variational principle, converging the energy calculated by DFT with respect to the energy cutoff is relatively simple because the energy *cannot* increase as more plane waves are used to represent the charge density.

Reciprocal space must be represented on a discrete grid so that various quantities can be defined at specific wave vectors and integrals can be performed in reciprocal space. VASP allows manual specification of a set of points in reciprocal space for this purpose but in most cases it is preferable to use an automatically generated grid. Such a grid can be generated in VASP by using the Monkhorst-Pack method which defines a regular grid of points at some specified density along each reciprocal lattice vector [46]. This grid is reduced down into the irreducible Brillouin zone using symmetry to minimize computational effort. As with the energy cutoff, the density of these grids must be converged on a case by case basis to ensure that integrals over reciprocal space have been sampled sufficiently.

A basic density functional theory calculation requires diagonalizing an $N \times N$ matrix where N is the number of electrons being considered. The computational complexity is therefore $O(N^3)$ and practical calculations on modern supercomputers are limited to handling a few thousand electrons in a single calculation. This could severely limit which materials can be reasonably studied - a single unit cell of PbZrO_3 already has 146 electrons in it and large supercells may be required to understand a materials properties. To alleviate this issue, the number of electrons can be significantly reduced through the use of pseudopotentials.

A pseudopotential divides the electrons associated with a particular atom into core and valence electrons. The core electrons in a pseudopotential are treated as having a fixed size around an atom and are not directly included in the rest of a calculation. Instead, the core electrons induce some effective potential on the valence electrons. Outside of the fixed size of the core electrons the valence electrons are free to behave as normal within density functional theory, albeit subject to the effective potential from the core electrons. The use of pseudopotentials therefore reduces the number of electrons being simulated which provides significant computational benefit.

The wave functions of the valence electrons must still be treated within the core region. These wave functions must be orthogonal to the wave functions of the core electrons which leads to a rapidly oscillating charge density that requires many plane waves to represent. VASP uses the projector augmented wave method [47] to transform these wave functions into more smoothly varying functions. This approach greatly reduces the number of plane waves required to adequately represent the charge density, further lowering the computational burden.

The creation of a pseudopotential for a given element is not trivial and can be done within any approximation to the exchange correlation functional. One of the benefits of using VASP over codes which implement DFT is that it provides a set of pseudopotentials, including at least one for each element. These pseudopotentials have been used extensively by the community and can generally be used without being concerned about their accuracy.

Three approximations to the exchange correlation functional were used in this dissertation. The first is the standard LDA. This approach is well known

to overbind atoms, leading to crystal structures that are a roughly one percent smaller than in reality [48]. This is a small deviation but can have significant effects on certain properties. The PBE implementation [37] of the GGA addresses this deviation but tends to overcorrect it, leading to crystals that are slightly too large [48]. An improved GGA known as PBEsol [38] was created to address these volume discrepancies. Using PBEsol usually underestimates the volume of a crystal but by a smaller amount than LDA [48]. LDA, PBE, and PBEsol pseudopotentials are all available with VASP. PBEsol was used in most cases, though LDA and PBE were used occasionally to check the dependence of results on the choice of pseudopotential.

Up to this point, VASP has been described as a way to calculate the energy of a given crystal structure. This is one of its primary features but it can perform many other functions related to crystal structures. The most relevant features are explained in the proceeding sections.

3.2.1 Crystal structure optimization

In many cases the property of interest is not simply the energy of a crystal structure. It is often useful to predict the precise crystal structure which can be accomplished by minimizing the energy of an input crystal structure. The energy of the crystal structure can be minimized using a conjugate gradient routine where the degrees of freedom are the atomic positions in the crystal structure. Within the DFT community, performing this minimization is often referred to as relaxing the crystal structure. VASP provides routines which are highly specialized for relaxing crystal structures.

Usually when performing a relaxation the symmetry of a crystal structure is preserved. A relaxation can therefore lead to a saddle point on the energy surface rather than a local minima. This allows for a more controlled minimization process and for the energies of crystal structures with different symmetries to be compared.

3.2.2 Phonons

After relaxing a crystal structure into a saddle point, the Hessian (second derivative) matrix can be calculated with respect to the position of the atoms in the crystal structure. Within VASP, density functional perturbation theory [49, 50] or a finite difference scheme may be used to calculate this matrix. After appropriate scaling of this matrix by mass, the eigenvectors of this matrix correspond to the phonon modes of the crystal structure. These modes represent distortions of the crystal structure that behave as springs with spring constants given by the eigenvalues within the harmonic approximation.

Phonon modes can be excited and measured using external perturbations, such as light which have frequency close to the frequency of a mode's spring constant. A comparison of experimentally measured and computed phonons is possible and can help provide insight into a materials behavior.

Calculating the Hessian matrix provides information about the stability of a crystal structure. If the matrix has any negative eigenvalues, the corresponding eigenvectors can be added to the crystal structure and will lower the energy. Assuming the Hessian was calculated at a saddle point, this distortion will necessarily lower the symmetry of the crystal structure. The energy low-

ering distortion can be relaxed into the crystal structure to find a new, lower energy, saddle point in the energy landscape.

Iteratively repeating this process is a reasonably thorough method to search for low energy structures which may be reached via displacive distortions of the crystal structure. While it is never possible to completely explore an energy landscape this method will find all structures with lower energy than the parent structure which may be reached via displacive distortions, assuming there are not any unusual anharmonic couplings between phonon modes. This search will not find low energy structures that cannot be related by displacive modes, such as structures in a martensitic phase transition.

3.2.3 Nudged Elastic Band

The transition path between two crystal structures can be studied within VASP using the nudged elastic band (NEB) method. This method takes a sequence of crystal structures as an initial guess at the transition path between two structures as input. The initial guess at a transition path is usually taken as a linear interpolation between the two crystal structures of interest. It is important that these two crystal structures are properly aligned so that only the desired degrees of freedom are changed along the transition path - otherwise there will be unnecessary changes to the crystal structure along the transition path, such as a net translation of the structure, leading to erroneous results.

The NEB method relaxes each structure along the transition path simultaneously while maintaining a fixed distance between adjacent structures in the transition path. This is accomplished by adding a fictitious force to each struc-

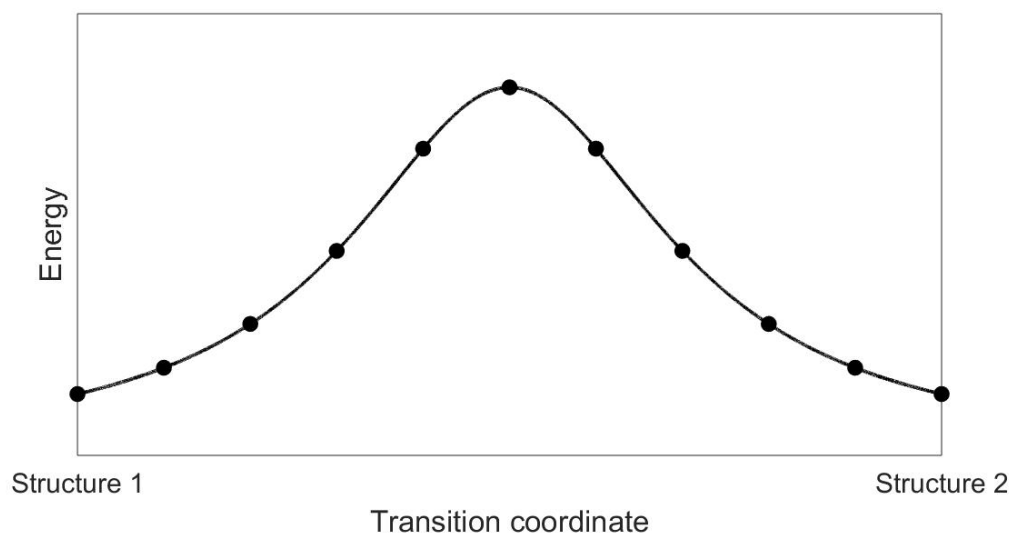


Figure 3.1: The energies along an example transition path calculated using NEB. The horizontal axis is an arbitrary coordinate corresponding to distance along the transition path.

ture to mimic a spring attached to the adjacent structures. After minimizing the energy of each structure along the transition path, one of the structures should relax into a saddle point corresponding to the transition state. An example of the energies of crystal structures along a transition path calculated by NEB is shown in Figure 3.1. The transition state is the highest energy point along the transition path and is necessarily a saddle point in the energy landscape.

An improved NEB algorithm, due to Henkelman, can be used after applying a small patch to VASP [51, 52]. The modification is called climbing image nudged elastic band (CI-NEB). This behaves very similarly to NEB but maximizes the energy of the highest energy structure along the transition path instead of minimizing it. This modification drastically improves the convergence rate of the calculation by actively forcing a single structure towards a saddle point.

3.3 Bond Valence Model

The bond valence model is an empirical model based on simple chemical concepts that can provide quantitative information about chemical bonding in a crystal structure [53, 54]. The model is based on Pauling's rules [55] and assumes purely ionic bonding. This model was used occasionally to help interpret crystal structures obtained from density functional theory.

Within the bond valence model, each bond is assigned a strength

$$S_{ij} = \exp\left(\frac{r_0 - r_{ij}}{b}\right) \quad (3.9)$$

where r_{ij} is the bond length between two atoms indexed by i and j . r_0 and b are empirically determined for each pair of elements that can share a bond. Extensive tables of these parameters are available [53].

Given the formal valence state of an ion, V_i , the discrepancy factor can be defined as

$$d_i = V_i - \sum_j S_{ij} \quad (3.10)$$

where the sum over j runs over all bonds involving ion i . Within the assumption of purely ionic bonding the sum provides an estimated value of the number of electrons received/donated to bonds by a given ion. For an ideally bonded ion that number would equal the formal valence state of the ion. The discrepancy factor measures the deviation from this ideal bonding environment. By convention a positive discrepancy factor indicates an underbonded ion, that is, an ion that wants to shorten its bonds in order to increase the number of electrons it has involved in bonds. Conversely, a negative discrepancy factor indicates an overbonded ion that wants to lengthen its bonds.

A global instability index can be defined as the root mean square of the discrepancy factors

$$G = \left[\frac{1}{N} \sum_i^N d_i^2 \right]^{1/2} \quad (3.11)$$

Values for G tend to be below 0.2 for realistic crystal structures and this metric has been used in the chemistry community to help verify novel crystal structures as valid [53].

As part of the work presented in this dissertation, a Fortran program was written which calculates discrepancy factors and the global instability index for a crystal structure. Fortran was chosen so that the code could better interface with several density functional programs also written in Fortran. The input to the program was designed to mimic the style of VASP so that it could be easily used on any crystal structures obtained from VASP. The program is also capable of calculating Coulomb energies, treating a modified bond valence model that attempts to include directional bonding information (bond valence vectors [53]) and optimizing a crystal structure subject to symmetry constraints with respect to G or any of the modified bond valence models. For the projects discussed in this dissertation, however, only the calculation of discrepancy factor and G were used so a complete description of the program is omitted.

CHAPTER 4

THE CRYSTAL STRUCTURE OF $\text{La}_2\text{SrCr}_2\text{O}_7$

4.1 Introduction

$\text{La}_2\text{SrCr}_2\text{O}_7$ was synthesized and characterized by experimental collaborators. The crystal structure was found to be a new and unexpected form of the $n=2$ Ruddlesden-Popper series. An in depth analysis of the crystal structure was performed using first principles calculations to understand why this material forms in a novel crystal structure. The crystal structure was found to be stabilized by a cooperative interaction between ionic distortions and disorder between the La and Sr cations. This unique coupling mechanism provides a route towards controlling tilting distortions in Ruddlesden-Poppers via cation disorder. Significant portions of this chapter are reproduced from a publication on this material¹.

4.2 Summary of experimental results

$\text{La}_2\text{SrCr}_2\text{O}_7$ was originally prepared to act as a substrate for a topochemical fluorination study focused on synthesizing phases containing Cr^{4+} [57]. The structure of $\text{La}_2\text{SrCr}_2\text{O}_7$ was expected to have an undistorted $n=2$ Ruddlesden-Popper phase belonging to space group $I4/mmm$. This expectation is based

¹Reproduced in part with permission from Reference [56] [R. Zhang, B. M. Abbett, G. Read, F. Lang, T. Lancaster, T. T. Tran, P. S. Halasyamani, S. J. Blundell, N. A. Benedek, and M. A. Hayward, *La₂SrCr₂O₇: Controlling the tilting distortions of $n = 2$ Ruddlesden-Popper phases through A-site cation order*, *Inorganic Chemistry*, vol. 55, pp. 89518960, Sep 2016]. Copyright 2016 American Chemical Society. Original online version: <http://pubsdc3.acs.org/articlesonrequest/AOR-KyS4FJngnx74cuXk9RbG>.

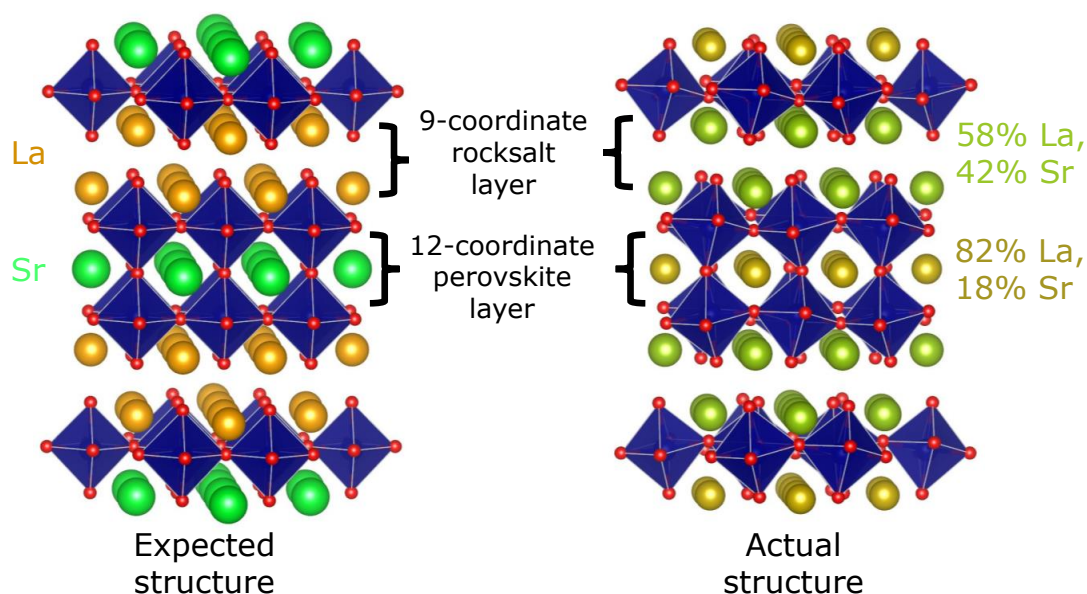


Figure 4.1: The expected and actual crystal structure of $\text{La}_2\text{SrCr}_2\text{O}_7$. Shaded blue regions indicate CrO_6 octahedra and red spheres are oxygen atoms. The La and Sr cations are shown as orange and green spheres. In the actual structure the La and Sr cations are disordered so their sites are colored according to a mixture of orange and green corresponding to the amount of La and Sr in a particular location.

on the tolerance factor of $\text{La}_2\text{SrCr}_2\text{O}_7$, a measure of the size mismatch between ions using their Shannon radii [58], being between that of $\text{La}_2\text{SrFe}_2\text{O}_7$ and $\text{La}_2\text{BaFe}_2\text{O}_7$ which both form in $I4/mmm$. The larger radii of Sr^{2+} compared to La^{3+} suggests that the the Sr cations will be located in the 12-coordinate perovskite layer, while the La cations will be in the 9-coordinate rocksalt layers. The expected structure is shown to the left of Figure 4.1.

The crystal structure was experimentally found to form in a distorted form of the $n=2$ Ruddlesden-Popper series. Determining the exact distortion is challenging in these materials because the distortions differ mainly in the position

Table 4.1: Possible $n=2$ Ruddlesden-Poppers structures. The tilt system follows the notation of Reference [59] which is essentially Glazer notation extended to the Ruddlesden-Poppers and uses slightly different notation. An equivalent Glazer like notation is also provided for each structure [25].

Space Group	Tilt Pattern	Glazer Notation
I4/mmm	000/000	$a^0a^0c^0/a^0a^0c^0$
Acam	$00\Psi_z/00\Psi_z$	$a^0a^0c^+/a^0a^0c^+$
Acam	$00\Phi_z/00\Phi_z$	$a^0a^0c^-/a^0a^0c^-$
Acmm	$\Phi\Phi 0/\bar{\Phi}\bar{\Phi} 0$	$a^-a^-c^0/\bar{a}^-\bar{a}^-c^0$
Amam	$\Phi\Phi 0/\Phi\Phi 0$	$a^-a^-c^0/a^-a^-c^0$
Pnam	$\Phi\Phi\Psi_z/\Phi\Phi\bar{\Psi}_z$	$a^-a^-c^+/a^-a^-c^+$
A2 ₁ am	$\Phi\Phi\Psi_z/\Phi\Phi\Psi_z$	$a^-a^-c^+/a^-a^-c^+$
A2/a	$\Phi\Phi\Phi_z/\Phi\Phi\Phi_z$	$a^-a^-c^-/a^-a^-c^-$

of oxygen atoms which do not produce easily observed changes in diffraction patterns. Several possible distorted structures were considered, as listed in Table 4.1. Out of these structures the A2/a structure was found to be the most likely structure experimentally, but the A2₁am and Amam structures could not be ruled out. The distortions in the A2/a structure are shown in Figure 4.1.

The observed distribution of La and Sr cations did not follow the expected ordered pattern. After structural refinement based on diffraction data, these cations were found to be disordered, meaning the cations are distributed randomly on a particular crystallographic site. The ratio of La to Sr on each atomic site is shown in Figure 4.1.

4.3 First-principles results

A series of first-principles density functional theory calculations were performed in order to gain further insight into the unexpected A-site cation ordering pattern and the $\Phi\Phi\Phi_z/\Phi\Phi\Phi_z$ tilting scheme observed for $\text{La}_2\text{SrCr}_2\text{O}_7$. Of particular interest is the rotations about the c-axis, which are what make this structure unique. Are these two structural features related, and if so, how? Details of the various parameters used in the calculations are explained in Section 4.6.

First, full structural relaxations were performed starting from the experimentally determined structural coordinates for the space groups and tilting schemes shown in Table 4.1; the Sr and La cations were placed on their expected sites, that is, Sr on the 12-coordinate perovskite A-site and La on the 9-coordinate rock salt A-site. The Acaa and Acmm structures both relaxed into $I4/mmm$, whereas the $A2/a$, $A2_1am$, and Pnam structures relaxed into Amam. In other words, tilts about the c-axis relaxed out for each structure, suggesting that octahedral tilts about c are energetically unfavorable without some disordering of the Sr and La sites. This is further corroborated by phonon calculations on $\text{La}_2\text{SrCr}_2\text{O}_7$ in the $I4/mmm$ and Amam space groups: lattice modes corresponding to octahedral tilts about c are stable (have real frequencies) in both space groups, indicating that such distortions are not energetically favorable.

Next, the effects of Sr/La disorder were explored by starting from a fully relaxed $I4/mmm$ structure and systematically generating a series of symmetry-unique structures (for a 24-atom simulation cell) with differing Sr/La distributions. These alternate distributions are an approximation of the disorder

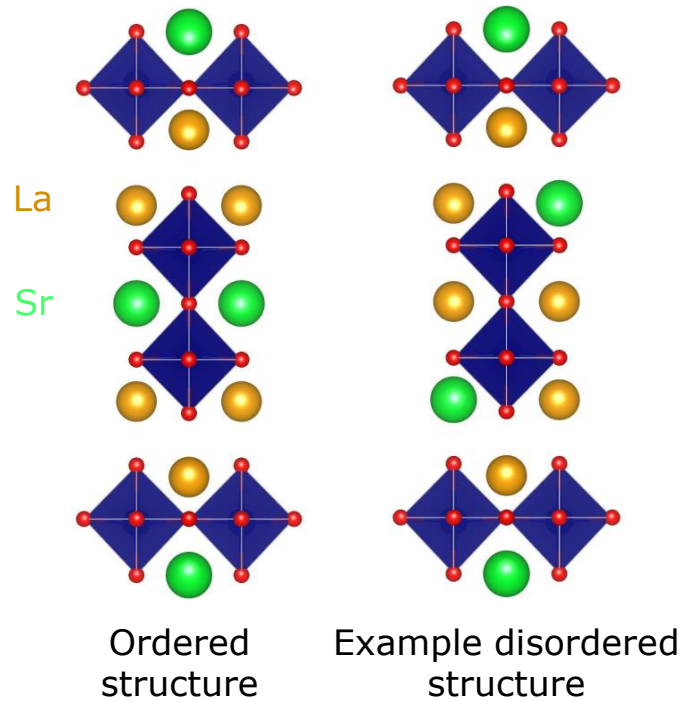


Figure 4.2: An example of how disorder between the La and Sr cations was treated. The structure on the right is identical to the structure on the left except several of the La and Sr cations have switched locations.

between La and Sr cations. An example of an alternate Sr/La distribution is shown in Figure 4.2. Within the 24-atom unit cell, any A-site disorder breaks the $I4/mmm$ symmetry with the resulting space group depending on the exact distribution of Sr and La cations. Without any structural relaxation, switching any Sr cation in a 12-coordinate site with any La cation in a 9-coordinate site raises the energy by at least 0.8 eV/formula unit (f.u.).

After full structural relaxation, the $I4/mmm$ structure with Sr and La on their expected sites remains the lowest in energy by approximately 20 meV/f.u. Hence, the results thus far suggest that, without some disordering of the Sr/La sites, octahedral tilts about the c-axis are energetically unfavorable, but without octahedral tilts the Sr and La cations prefer to be in the perovskite and rock salt

layers, respectively. Disordering of the Sr and La cations appears to be related to the experimental observation of the $\Phi\Phi\Phi_z/\Phi\Phi\Phi_z$ tilting scheme: why?

The computational framework used to simulate crystal structures does not allow for fractional occupancies of atoms, so it was necessary to investigate structures with many different specific distributions of Sr/La in order to enable comparisons between theory and experiment. Rather than trying to exactly reproduce the observed Sr/La distribution, the goal was to explore structural trends across a range of different distributions, which includes the experimentally observed one. Starting from a 48-atom simulation cell (four formula units), a series of structures were constructed with the following Sr/La distributions: 0/100 in rock salt, 100/0 in perovskite; 12.5/87.5 in rock salt, 75/25 in perovskite; 25/75 in rock salt, 50/50 in perovskite; 37.5/62.5 in rock salt, 25/75 in perovskite; 50/50 in rock salt, 0/100 in perovskite. Hence, this simulation cell can accommodate Sr/La distributions that approximate the observed one (42/58 in rock salt, 18/82 in perovskite) reasonably closely as well as the various octahedral twisting patterns considered in the experimental structure refinements. Investigating every possible arrangement of Sr and La cations for each distribution would be extremely computationally intensive (there are approximately 500 possible, not necessarily symmetry unique, structures for the 48-atom unit cell used), so 36 arrangements were selected by hand with a mix of the Sr/La distributions listed above. From the calculations in a 24-atom simulation cell, it was apparent that structures with multiple adjacent Sr cations tended to have higher energies. This tendency prompted the selection of arrangements with the Sr cations spread out in a 48-atom simulation cell, which were expected to also be lower in energy. Several arrangements with clusters of Sr cations were also included that were expected to be high in energy for comparison. For

each arrangement of Sr/La, a relaxation was performed starting from the experimental coordinates for $\text{La}_2\text{SrCr}_2\text{O}_7$ in $A2/a$, $Pnam$, and $A2_1am$; this produced $36 \times 3 = 108$ structures with varying Sr/La distributions for further investigation. This set of structures was expected to be sufficient to study structural and energetic trends relevant to the experimental data. The full list of structures considered and the symmetry of each is enumerated in Table 4.2. Note that, due to the A-site cation disorder, the final, relaxed structures are lower in symmetry than the starting $A2/a$, $Pnam$, and $A2_1am$ structures.

Table 4.2: Symmetries of structures considered with alternate A-site orders. The La/Sr sites columns denote which La and Sr ions were swapped from their expected positions as shown in Figure 4.3. As an example the ninth row means that La4 and La8 sites were swapped with the Sr1 and Sr2 sites.

Structure Number	La sites	Sr sites	A2/a like structure	Pnam like structure	A2 ₁ am like structure
1	1	4	P1	P1	P1
2	1	3	P1	P1	P1
3	1	2	P1	P1	P1
4	1	1	P1	P1	P1
5	1, 2	3, 4	P $\bar{1}$	P2 ₁	P1
6	1, 7	1, 2	P1	P1	P1
7	1, 6	1, 2	P1	P1	P1
8	1, 4	1, 2	Pc	Pc	Pc
9	4, 8	1, 2	P1	P1	P1
10	1, 4	1, 3	P1	P1	P1
11	1, 3	1, 2	P2	Pm	P1
12	1, 7	1, 3	P2 ₁	P2 ₁	Pc
13	1, 2	1, 2	P $\bar{1}$	P2 ₁	P1
14	3, 4	1, 2	$\bar{1}$	P2 ₁	P1
15	1, 2	1, 3	P1	P1	P1
16	1, 2	1, 4	P1	P1	P1
17	1, 3	1, 4	P2	Pm	P1
18	1, 3	1, 3	P2	Pm	P1
19	4, 8	2, 4	P1	Pc	P1
20	1, 4, 7	1, 2, 4	P1	P1	P1
21	1, 4, 7	1, 2, 3	P1	P1	P1
22	1, 7, 8	1, 2, 4	P1	P1	P1
23	1, 7, 8	1, 2, 3	P1	P1	P1
24	1, 7, 8	2, 3, 4	P1	P1	P1
25	3, 4, 8	1, 2, 3	P1	P1	P1
26	1, 4, 8	1, 3, 4	P1	P1	P1
27	1, 4, 8	2, 3, 4	P1	P1	P1
28	1, 7, 8	1, 3, 4	P1	P1	P1
29	3, 4, 8	1, 2, 4	P1	P1	P1
30	1, 4, 8	1, 2, 3	P1	P1	P1
31	1, 4, 8	1, 2, 4	P1	P1	P1
32	1, 4, 6, 7	1, 2, 3, 4	P2 ₁ /c	P2 ₁ /c	Pca2 ₁
33	1, 4, 7, 8	1, 2, 3, 4	P1	P1	P1
34	3, 4, 5, 6	1, 2, 3, 4	P2 ₁ /c	P2 ₁ 2 ₁ 2 ₁	Pc
35	3, 4, 7, 8	1, 2, 3, 4	P $\bar{1}$	P2 ₁ /c	P21
36	1, 4, 5, 8	1, 2, 3, 4	Cc	Pna2 ₁	Pc

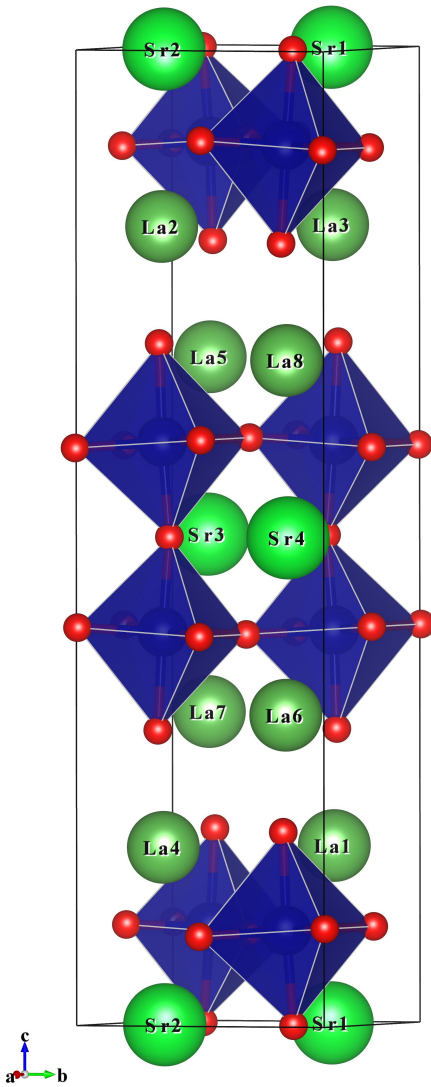


Figure 4.3: Schematic labeling the A-site positions.

Each of the $A2/a$, $Pnam$, and $A2_1am$ space groups is a subgroup of $Amam$ (with the La and Sr ions in their expected positions) and differ in the pattern of octahedral tilting about the c -axis. The $Amam$ structure is thus used as a reference structure, since $La_2SrCr_2O_7$ in this space group does not have octahedral tilts about c . Figure 4.4 shows that various distributions of Sr/La can result

in structures that are lower in energy than the Amam reference structure with Sr and La on their expected sites. The relaxations starting from A2/a, Pnam, and A2₁am always resulted in three structures with similar energies. The three initial structures relaxed into identical structures for some of the Sr/La distributions, but in these cases the relaxed energy is typically higher than that of the Amam reference structure. The energies shown in Figure 4.4 are shown again in Figure 4.5, with the x-axis changed to be the mean Sr-Sr distance, confirming the general trend that A-site arrangements with Sr cations spread out are lower in energy.

Thorough examination of the low-energy (compared to Amam) relaxed structures in Figure 4.4 revealed that the lowest energy structure for each Sr/La distribution has A2/a-like octahedral tilts about *c*, with a single exception. Sometimes one or both of the relaxations started from Pnam or A2₁am coordinates relaxed into the same structure as the relaxation started from A2/a coordinates. For the low-energy Sr/La distributions, these identical structures have octahedral tilts about *c* corresponding to the A2/a symmetry. Since the lowest energy structure for all but one of the Sr/La distributions has primarily A2/a-like octahedral tilts about *c*, these tilts appear to be the most stable so structural trends were analyzed within the A2/a-like structures.

4.4 Linear correlation analysis

Structural trends were analyzed among the 36 A2/a-like structures to better understand the interplay between A-site disorder and octahedral tilts. The large number of structures, combined with their low symmetry and Sr/La disorder,

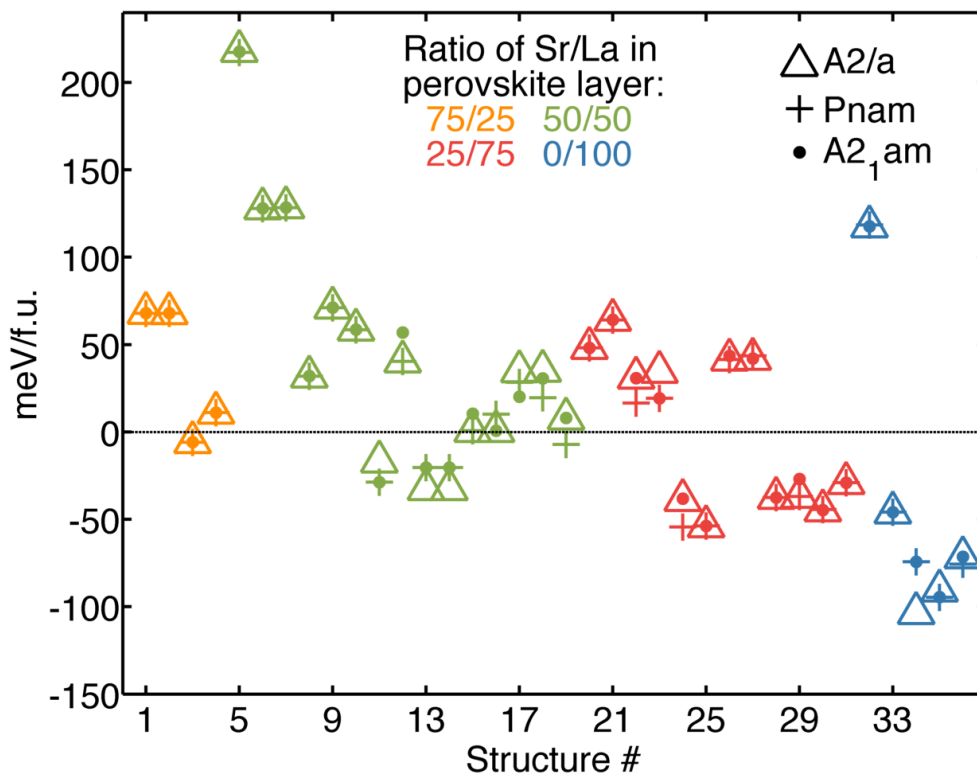


Figure 4.4: Relaxed energies per formula unit (f.u.) of 108 structures with varying La/Sr distributions with respect to the energy of the Amam reference structure with La/Sr cations on their expected sites. Color and shape of points indicate the ratio of Sr/La distribution and initial ionic positions, respectively. Note that in many cases plot symbols overlap. The horizontal axis is labeled by arbitrary structure numbers corresponding to Table 4.2. The structures are sorted by the Sr/La ratio and the mean distance between Sr cations in our relaxed Amam structure after swapping Sr/La positions, but before any further relaxation. A general tendency for energy to be lowered as the Sr cations spread out is evident.

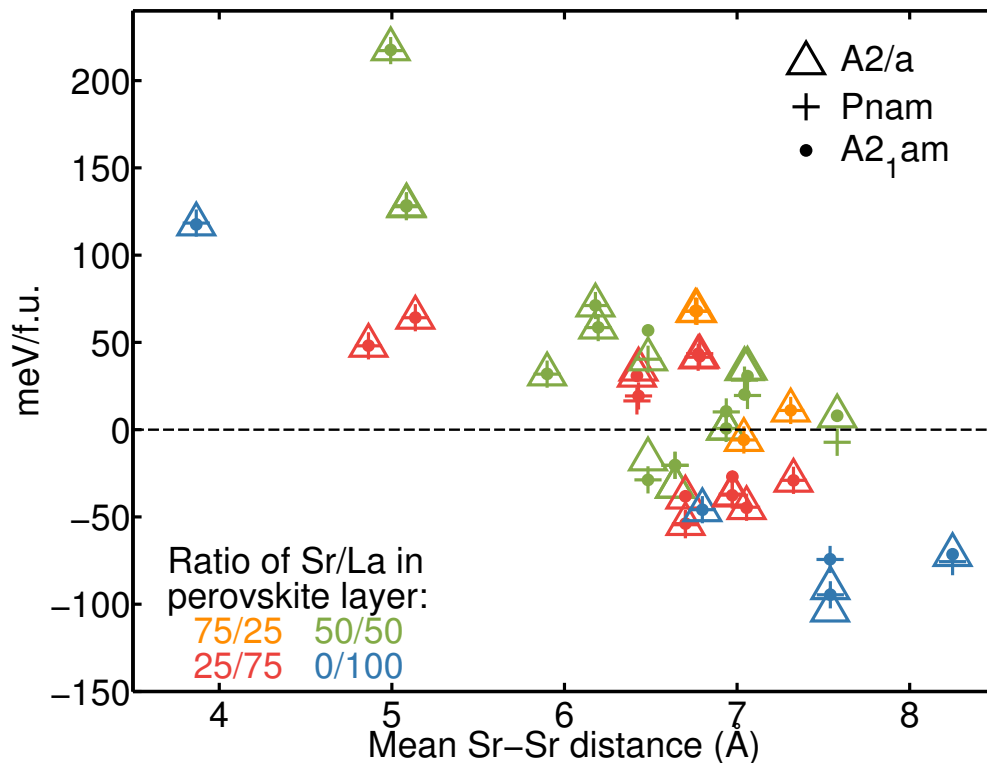


Figure 4.5: Relaxed energies per formula unit (f.u.) of 108 structures with varying La/Sr distributions with respect to the energy of the Amam reference structure with La/Sr cations on their expected sites. Color and shape of points indicate the ratio of Sr/La distribution and initial ionic positions respectively. The horizontal axis is the mean distance between Sr cations in our relaxed Amam structure after swapping Sr/La positions, but before any further relaxation.

demanded a systematic, quantitative approach. Correlations between various structural features and the octahedral tilts about *c* were searched for since the experimentally considered structures differ in their *c*-axis tilting patterns. The first challenge was to determine how to quantify the magnitude of tilting about the *c*-axis. Normally a rigorous symmetry-adapted mode analysis could be performed to obtain such information, but in this case A-site disorder makes such

an approach extremely challenging. As an alternative, bond valence discrepancy factors were used to quantify the average bonding environment of the equatorial oxygen atoms O_{eq} (that is, the oxygen atoms that reside in the CrO_2 layers) which will be directly affected by octahedral tilts about c . The discrepancy factor [60] is defined as the difference between the formal valence of a particular ion, and the calculated bond valence sum for the same ion in the structure of interest. A discrepancy factor of zero thus indicates that the ion is ideally coordinated. A positive discrepancy factor indicates underbonding (the cation-anion bonds are too long compared to the ideal, strain-free coordination environment in the bond valence model), whereas a negative discrepancy factor indicates overbonding (cation-anion bonds are too short). In addition, the values of 47 different structural features were calculated for each of the relaxed structures. A linear correlation analysis was used to guide the search for trends between these features and the bonding environment of the equatorial oxygens.

The structural features included, for example, Cr-O-Cr bond angles, CrO_6 volumes, and distortion indices (defined as the average fractional deviation of Cr-O bond lengths from the average Cr-O bond length in a CrO_6 octahedron [61]), and bond valence discrepancy factors for each atom. In many cases these features were averaged over the entire structure, which was necessary because the low symmetry of many structures allowed, for instance, each CrO_6 octahedron in a particular structure to be unique. Variances, minima, and maxima of various structural features were also calculated to help quantify structures with a large range of a particular structural feature. The complete list of structural features considered is given in Table 4.4.

Table 4.4: List of the structural features we calculated for each of our relaxed structures.

Feature Number	Feature
1	Calculated energy of structure
2	Average Cr-O-Cr in plane angle
3	Variance of Cr-O-Cr in plane angle
4	Average Cr-O-Cr angle
5	Variance of Cr-O-Cr angle
6	Bond valence global instability index
7	Average Cr-O bond length
8	Average CrO ₆ volume
9	Average CrO ₆ distortion index
10	Average CrO ₆ quadratic elongation
11	Average CrO ₆ bond angle variance
12	Variance of the average Cr-O bond length in each CrO ₆
13	Variance of CrO ₆ volumes
14	Variance of CrO ₆ distortion indices
15	Variance of CrO ₆ quadratic elongations
16	Variance of CrO ₆ bond angle variance
17	Minimum of average Cr-O bond length in each CrO ₆
18	Minimum CrO ₆ volume
19	Minimum CrO ₆ distortion index
20	Minimum CrO ₆ quadratic elongation
21	Minimum CrO ₆ bond angle variance
22	Maximum of average Cr-O bond length in each CrO ₆
23	Maximum CrO ₆ volume
24	Maximum CrO ₆ distortion index
25	Maximum CrO ₆ quadratic elongation
26	Maximum CrO ₆ bond angle variance
27	Range of CrO ₆ distortion indices
28	Average discrepancy factor of La
29	Average discrepancy factor of Sr
30	Average discrepancy factor of Cr
31	Average discrepancy factor of La in perovskite layer
32	Average discrepancy factor of La in rock salt layer
33	Average discrepancy factor of Sr in rock salt layer
34	Average discrepancy factor of apical oxygen in perovskite layer
35	Average discrepancy factor of apical oxygen in rock salt layer
36	Average discrepancy factor of equatorial oxygen
37	Variance of discrepancy factor of La
38	Variance of discrepancy factor of Sr
39	Variance of discrepancy factor of Cr
40	Variance of discrepancy factor of La in perovskite layer

Table 4.4 continued

Feature Number	Feature
41	Variance of discrepancy factor of La in rock salt layer
42	Variance of discrepancy factor of Sr in rock salt layer
43	Variance of discrepancy factor of apical oxygen in perovskite layer
44	Variance of discrepancy factor of apical oxygen in rock salt layer
45	Variance of discrepancy factor of equatorial oxygen
46	Ratio of Sr in perovskite layer
47	Average minimum Cr-O bond length
48	Average maximum Cr-O bond length

After calculating each of the features in Table 4.4 a pairwise linear correlation coefficient was calculated for each pair of features within each of the structure types considered. Figure 4.6 is a visualization of the results for structures relaxed starting from the A2/a ionic positions and constrained to the experimental unit cell. This analysis allowed trends to be easily identified, such as the nearly perfect correlation between the average maximum Cr-O bond length and the average CrO₆ volume.

For comparison the pairwise linear correlation coefficients for relaxations starting from the A2/a ionic positions but with an unconstrained unit cell are shown in Figure 4.7. While the overall trends appear similar, the structural correlations after allowing cell relaxation tend to be weaker. This is especially apparent for features involving average discrepancy factors (features 28-36). This difference is attributed in part to the low symmetry of the relaxed structures, which allows the unit cell to relax in a different way for each structure. Further, the bond valence model is based on coefficients that are fit to experimental data. Past experience has shown this seems to cause the model to become less reliable for interpreting DFT results that are not constrained to the experimental volume. For these reasons, the results from structures which are constrained to

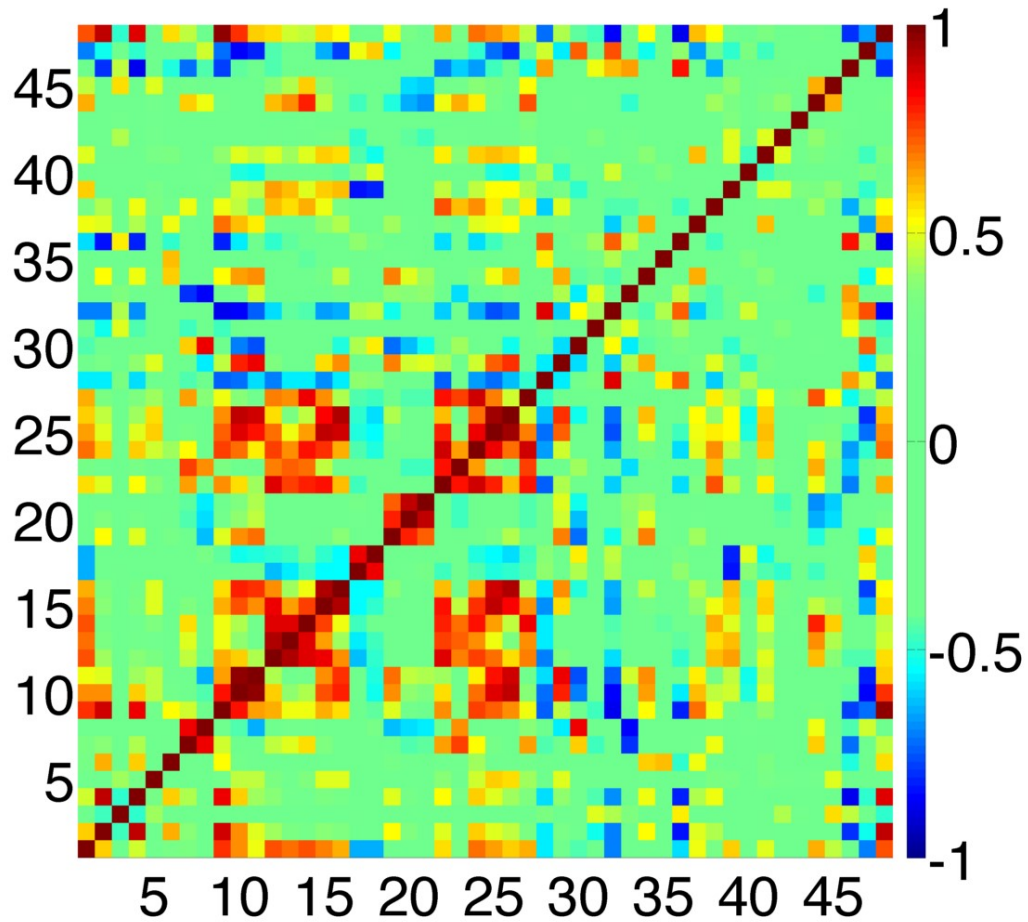


Figure 4.6: Linear correlation coefficients of the features listed in Table 4.4 for structures relaxed starting from A2/a ionic positions and constrained to the experimental unit cell.

the experimental unit cell were used.

The linear correlation analysis revealed strong correlations between the bonding environment of the O_{eq} anions and the average maximum Cr-O bond length, the Cr-O-Cr in-plane angle (this is the Cr-O-Cr angle assuming the three ions lie in the same plane, which emphasizes octahedral rotations about c rather than the in plane axes that dominate the Cr-O-Cr), the ratio of Sr to La in the

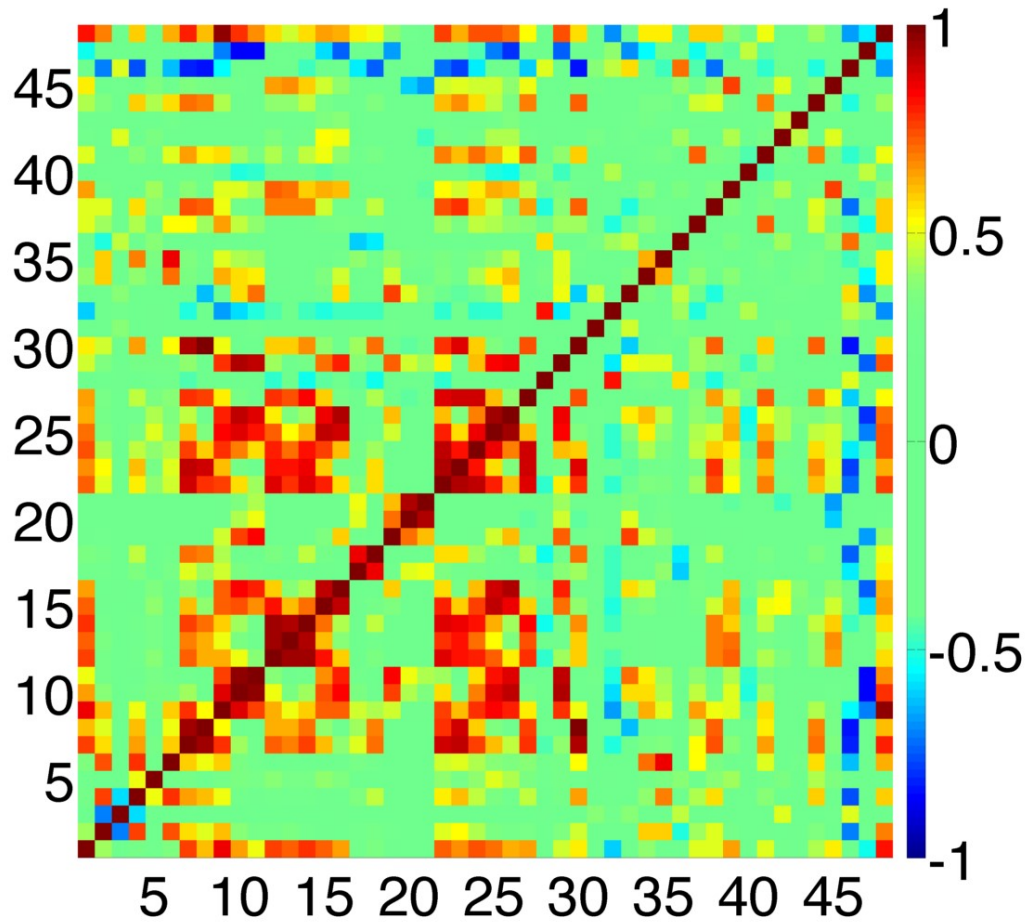


Figure 4.7: Linear correlation coefficients of the features listed in Table 4.4 for structures relaxed starting from A2/a ionic positions with the unit cell fully relaxed.

perovskite layer, the average CrO_6 distortion index, and the average discrepancy factor of La cations in the rock salt layers (La_{rs}). What do these correlations mean chemically and physically?

4.5 Interpretation of correlations

Figure 4.8 shows a plot of the average CrO_6 distortion index against the discrepancy factors of both the O_{eq} anions, and the La_{rs} cations, for A2/a energy minimized structures with a range of Sr/La cation distributions. The analogous discrepancy factors from the Sr/La cation-ordered Amam reference structure are also plotted in Figure 4.8. Noting the broad relationship between the Sr/La distribution (as indicated by the color of the points in Figure 4.8) and the CrO_6 distortion index, it is also apparent that the CrO_6 distortion index in the Amam reference structure (0.02578) is much larger than typically observed experimentally in other Cr^{3+} oxides. For comparison the distortion indices of Cr^{3+}O_6 octahedra in the experimentally determined structures for BiCrO_3 , LaCrO_3 , PrCrO_3 , GdCrO_3 , TbCrO_3 , YCrO_3 , HoCrO_3 , TmCrO_3 , YbCrO_3 , LuCrO_3 , InCrO_3 , and ScCrO_3 are, respectively, 0.00268 [62], 0.01143 [63], 0.00488 [63], 0.00181 [63], 0.0423 [63], 0.0044 [63], 0.00347 [63], 0.00083 [63], 0.00455 [63], 0.00445 [63], 0.01032 [64], and 0.00651 [64]. The remaining data in Figure 4.8 show that as an increasing fraction of the Sr cations are moved into the rock salt layer, the CrO_6 distortion index decreases dramatically. Further insight into this observation can be gained by noting that there is an almost linear relation between the average maximum Cr-O bond length and CrO_6 distortion index, as shown in Figure 4.9. This highlights the fact that the relatively large CrO_6 distortion index observed for the cation-ordered Amam reference structure can be attributed to a single long bond between the chromium and the axial oxide ion residing within the rock salt layer. As more strontium is moved into the rock salt layers, this axial Cr-O bond length decreases, and thus, the CrO_6 distortion index decreases.

The coupling between the Sr/La distribution and the Cr-O axial bond length

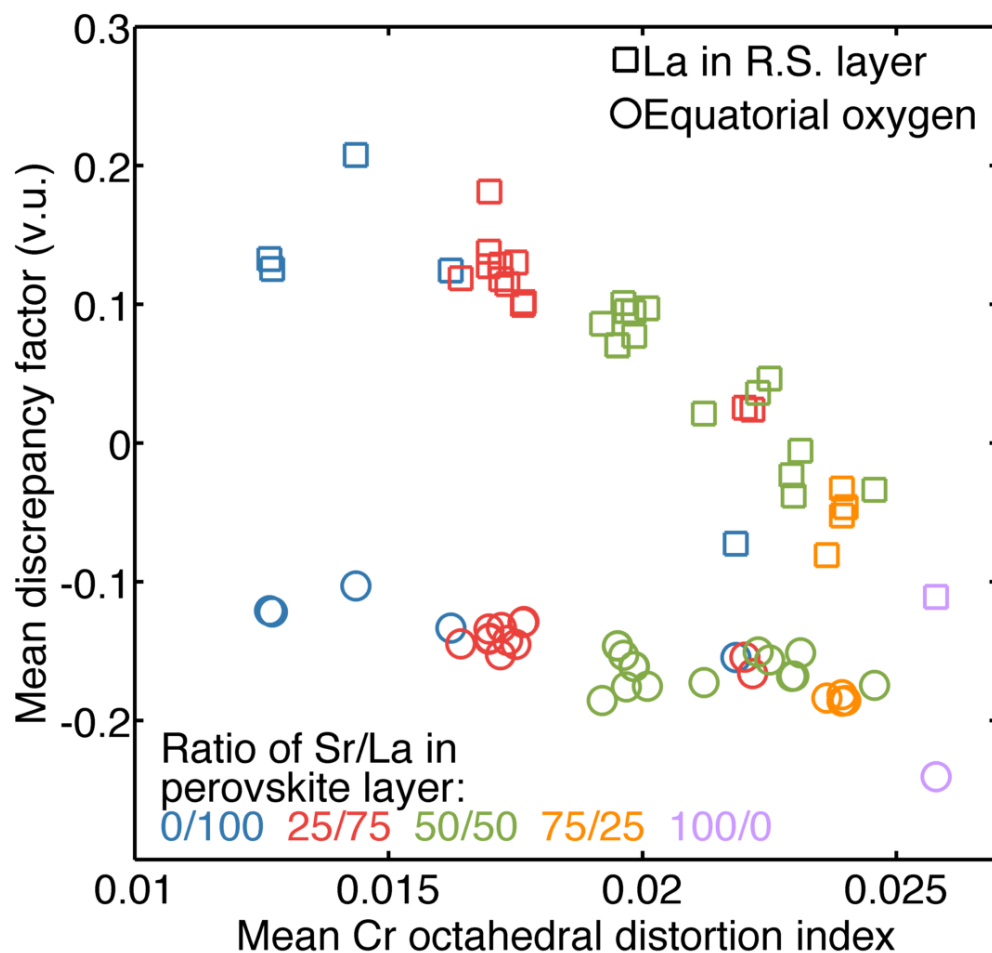


Figure 4.8: Average discrepancy factor, in valence units (v.u.) of La cations in the rock salt layer and equatorial oxygen ions as a function of the average CrO_6 distortion index with various A-site distributions. Light purple points correspond to the reference Amam structure with the expected A-site cation ordering.

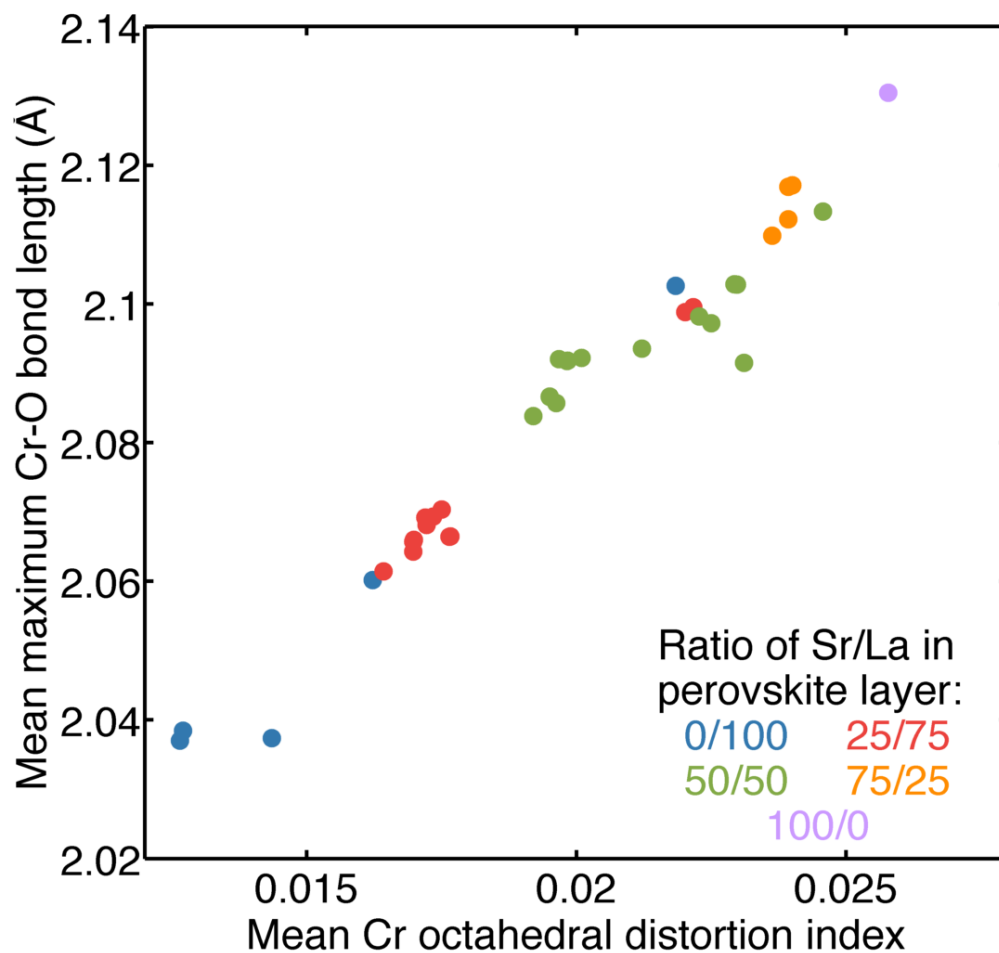


Figure 4.9: Average maximum Cr-O bond length as a function of the average CrO_6 distortion index with various A-site distributions. Light purple points correspond to the reference Amam structure with the expected A-site cation ordering. As the mean maximum Cr-O bond length increases, the mean CrO_6 distortion index increases linearly. The maximum of each is reached in the Amam structure with La and Sr cations on their expected sites.

can be accounted for by a simple electrostatic interaction. When the La and Sr cations are ordered within the Amam reference structure, there are negatively charged CrO_2 layers sandwiched between a positively charged LaO rock salt layer and a charge neutral SrO perovskite layer. In this situation the positively charged Cr atoms displace toward the neutral SrO layer, leading to a single long bond between Cr and an apical oxygen in the LaO layer. As the La/Sr distribution is disordered, the charges of the rock salt and perovskite AO layers become more even, and the tendency for Cr to undergo this distortion decreases, leading to a more uniform set of Cr-O bond lengths. Therefore, one of the reasons for the disordering of the La and Sr cations is to decrease the asymmetry of the CrO_6 units and thus strengthen the Cr-O bonding. However, as noted above, in the absence of octahedral tilts around the c-axis, Sr/La disorder is energetically unfavorable, so the strengthening of the Cr-O bonds alone is not sufficient to disorder the A-cations.

An indication of the role of the octahedral rotations in stabilizing the observed structure of $\text{La}_2\text{SrCr}_2\text{O}_7$ can also be seen in Figure 4.8, which shows that, in addition to the adoption of more symmetric CrO_6 units, the disordering of the Sr/La cations leads to an improvement in the O_{eq} bonding environment; these oxygen ions are significantly overbonded (compressed) in the Sr/La ordered Amam structure, and this overbonding is relieved somewhat by the unusual experimentally observed Sr/La distribution. However, the improvements in the bonding environments of O_{eq} and Cr come at the expense of a deterioration in the La_{rs} bonding environment. The La cations are slightly overbonded in the cation-ordered Amam reference structure and become increasingly underbonded as the concentration of Sr in the perovskite layers decreases. How do these observations relate to octahedral tilts about c?

Figure 4.10 shows the same data as Figure 4.8, but with the average in-plane Cr-O-Cr angle as abscissa. This angle decreases from 180° (indicating an increasing magnitude of tilts about c) as the concentration of Sr in the perovskite layers decreases, with an associated improvement/deterioration of the $O_{\text{eq}}/La_{\text{rs}}$ bonding environments. Summarizing the arguments above, the principal driver for the disordering of the La and Sr cations is the desire to lower the charge difference between the La-O rock salt and Sr-O perovskite layers, and thus making the CrO_6 units more symmetric. As noted previously, in the absence of octahedral tilts around the c -axis, the stabilization of the Cr-O bonding is not sufficient to overcome the inherent stability of the Sr/La A-site ordered configuration, so Sr/La disorder is not observed. However, in addition to equalizing the charges of the rock salt and perovskite layers, Sr/La disorder locally breaks symmetry about the equatorial oxygens, allowing them to displace and the CrO_6 units to rotate. This allows the O_{eq} bonding to be optimized, and in combination, the improvement to the bonding of both the chromium and equatorial oxide ions is sufficient to make the cation-disordered, $\Phi\Phi\Phi_z/\Phi\Phi\Phi_z$ distorted structure more stable than the cation-ordered Amam arrangement.

The importance of the optimization of the CrO_6 bonding as a driving force for the Sr/La cation disorder, and the associated $\Phi\Phi\Phi_z/\Phi\Phi\Phi_z$ distortion, is highlighted by comparing the $\text{La}_2\text{SrCr}_2\text{O}_7$ system to other $n=2$ Ruddlesden-Popper phases, most notably the Fe^{3+} containing $\text{Ln}_2\text{AEFe}_2\text{O}_7$ ($\text{AE} = \text{Sr}, \text{Ba}$) series. $\text{La}_2\text{SrFe}_2\text{O}_7$ adopts an undistorted $n=2$ Ruddlesden-Popper structure (space group $I4/mmm$) with a 53:47 Sr:La ratio on the perovskite A-site [65]. Likewise, $\text{La}_2\text{BaFe}_2\text{O}_7$ adopts an undistorted structure with a 73:37 Ba:La ratio on the perovskite A-site [65]. Thus, both phases favor locating the large AE^{2+} cation on the perovskite A-site (compared to the 33:66 $\text{AE}^{2+}:\text{La}^{3+}$ ratio expected

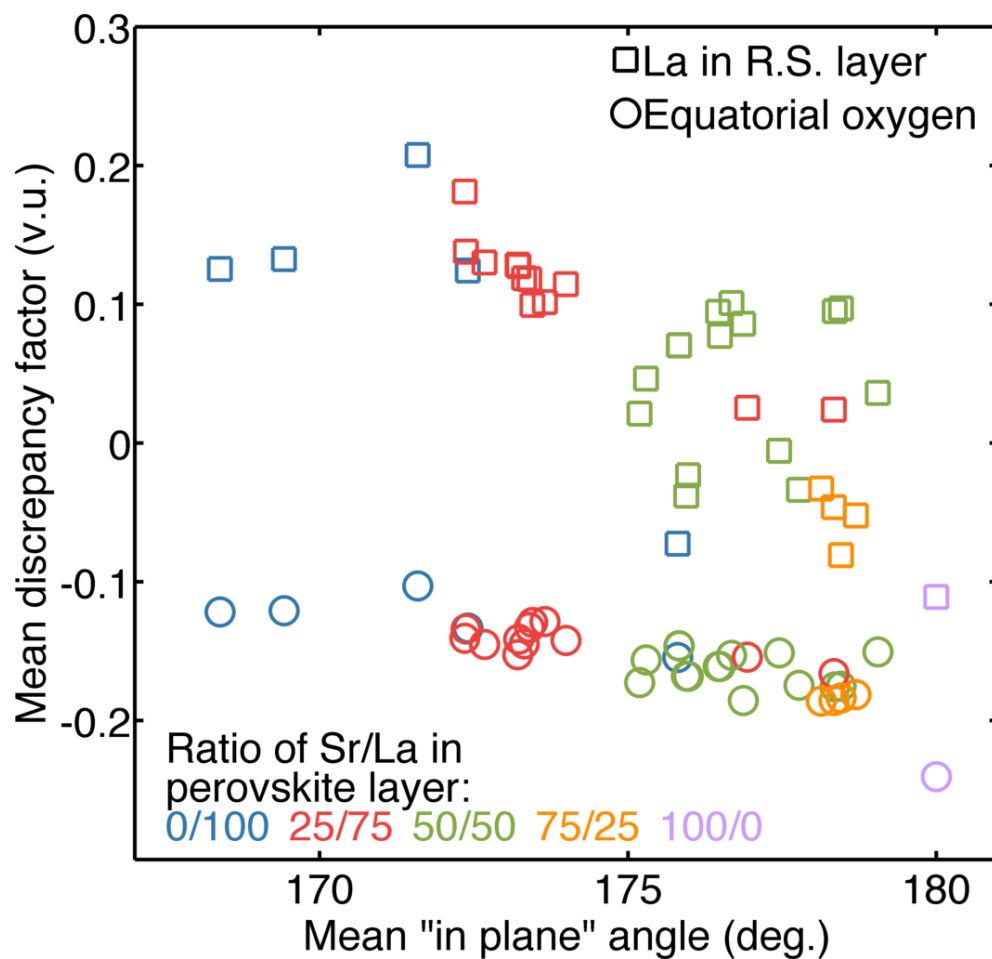


Figure 4.10: Average discrepancy factor of La cations in the rock salt layer and equatorial oxygen ions as a function of the average in-plane Cr-O-Cr angle with various A-site distributions. Light purple points correspond to the reference Amam structure with the expected A-site cation ordering.

statistically), and neither exhibit any collective rotations of their FeO_6 octahedra, in strong contrast to $\text{La}_2\text{SrCr}_2\text{O}_7$. A further contrast to the chromium system is that both $\text{La}_2\text{SrFe}_2\text{O}_7$ and $\text{La}_2\text{BaFe}_2\text{O}_7$ exhibit highly distorted FeO_6 units. As noted above, the primary distortion mode of the CrO_6 octahedra is the lengthening of the bond between chromium and the axial oxide ion in the rock salt layer. By defining a distortion parameter, MO_6 -axial-distort ($\text{MO}_{6\text{-ad}}$), as the ratio of the M-O bonds to the axial oxide ions in the rock salt and perovskite layers ($\text{MO}_{6\text{-ad}} = \text{M-O}_{\text{rs}}/\text{M-O}_{\text{p}}$), it can be seen that the FeO_6 units in $\text{La}_2\text{SrFe}_2\text{O}_7$ and $\text{La}_2\text{BaFe}_2\text{O}_7$ yield values of 1.12 and 1.14, respectively [65], compared to a value of 1.03 for $\text{La}_2\text{SrCr}_2\text{O}_7$. These observations are consistent with the idea that (i) the normal A-cation distribution of AE^{2+} on the perovskite A-site and La^{3+} on the rock salt A-site induces a distortion into the MO_6 octahedra and (ii) the desire to accommodate the Cr^{3+} cations in highly symmetric CrO_6 units leads to the adoption of the novel A-cation-disordered, $\Phi\Phi\Phi_z/\Phi\Phi\Phi_z$ distorted structure observed for $\text{La}_2\text{SrCr}_2\text{O}_7$.

The strong preference for locating Cr^{3+} centers in highly symmetric octahedral coordinations, in comparison to other transition metal cations such as Fe^{3+} , is also consistent with similar observations made for Cr^{3+} centers in a wide variety of other chemical systems. This wider observation is justified on the basis of the maximum ligand-field stabilization energy (LFSE) associated with the $t_{2g}^3 e_g^0$ local electronic configuration of Cr^{3+} , compared to the zero net LFSE for the $t_{2g}^3 e_g^2$ configuration of Fe^{3+} [66]. On lowering the symmetry of the MO_6 units, M-O bonding will be compromised; however, in the case of Fe^{3+} the associated lowering in energy of the occupied e_g antibonding orbitals will help to mitigate this, reducing the energy penalty for the distortion of Fe^{3+}O_6 units compared to Cr^{3+}O_6 units. This leads to the suggestion that a similar coupling of the A-site

cation order and octahedral rotations as observed in $\text{La}_2\text{SrCr}_2\text{O}_7$ can be expected in other $n=2$ Ruddlesden-Popper phases which contain “undistortable” transition metal cations, such as the as yet unreported phase $\text{La}_2\text{SrRh}_2\text{O}_7$, in which the expected low-spin $t_{2g}^6 e_g^0$ electronic configuration of Rh^{3+} should strongly resist distortions to the RhO_6 octahedra.

4.6 Calculation details

First-principles calculations were carried out using the Vienna ab Initio Simulation Package [43, 44]. The PBEsol exchange-correlation potential and projector augmented wave pseudopotentials [47, 45] were used throughout. The valence electron configurations for each pseudopotential were the following: $5s^2 5p^6 5d^1 6s^2$ for La; $4s^2 4p^6 5s^2$ for Sr; $3s^2 3p^6 3d^5 4s^1$ for Cr; and $2s^2 2p^4$ for O. The calculations were spin-polarized and included a Hubbard U of 4.0 eV for the Cr 3d electrons (changing U to 2.0 or 6.0 eV did not qualitatively change the structural analysis of the $A2/a$ structure). A complete study on the effects of including a Hubbard U on the La 4f electrons was not performed, but several tests indicated that this would mainly reduce the amplitude of octahedral rotations in relaxed structures, which does not alter the conclusions of this study.

Relaxations were considered converged when the force on each atom became smaller than $1 \text{ meV}/\text{\AA}$. A plane wave cutoff of 600 eV was used throughout. A $6 \times 6 \times 1$ Monkhorst-Pack mesh was used for the 24-atom simulation cells and a $4 \times 4 \times 1$ Monkhorst-Pack mesh was used for all other simulation cells. This energy cutoff and k-point mesh resulted in an energy difference between relaxed $A_{2/a}$ and $I4/mmm$ structures that is converged to within 0.05 meV

per formula unit, compared to higher plane wave cutoffs and denser kpoint meshes.

This study focused on structural features and trends, so a ferromagnetic ordering of spins on the Cr ions was assumed throughout most of the analysis. To check the effect of magnetic ordering on our simulations, the energy of each relaxed structure with the observed experimental antiferromagnetic ordering was calculated. The energy of the antiferromagnetic energy is lower for each structure, but the energy drop is similar in each case. Figure 4.11 shows the energy of both ferromagnetic and antiferromagnetic ordering for each structure. The relative energy difference between structures is qualitatively similar for each magnetic ordering so the trends found with ferromagnetic ordering should also exist in structures with antiferromagnetic ordering.

4.7 Conclusion

The complex coupling between the rotations of the CrO_6 octahedra and the La/Sr A-site distribution of $\text{La}_2\text{SrCr}_2\text{O}_7$ clearly demonstrates that the cooperative, symmetry-lowering distortions of $n=2$ Ruddlesden-Popper phases are not solely directed by the structural tolerance factor. Instead it appears that the structures adopted by these phases are determined by a number of different parameters in combination. This multiplicity of factors influencing the distorted structures of $n=2$ Ruddlesden-Popper phases provides many opportunities to direct the tilting arrangements in layered perovskite phases, to tune both the magnitude of the B-O-B angles and the symmetry of the cooperatively distorted network.

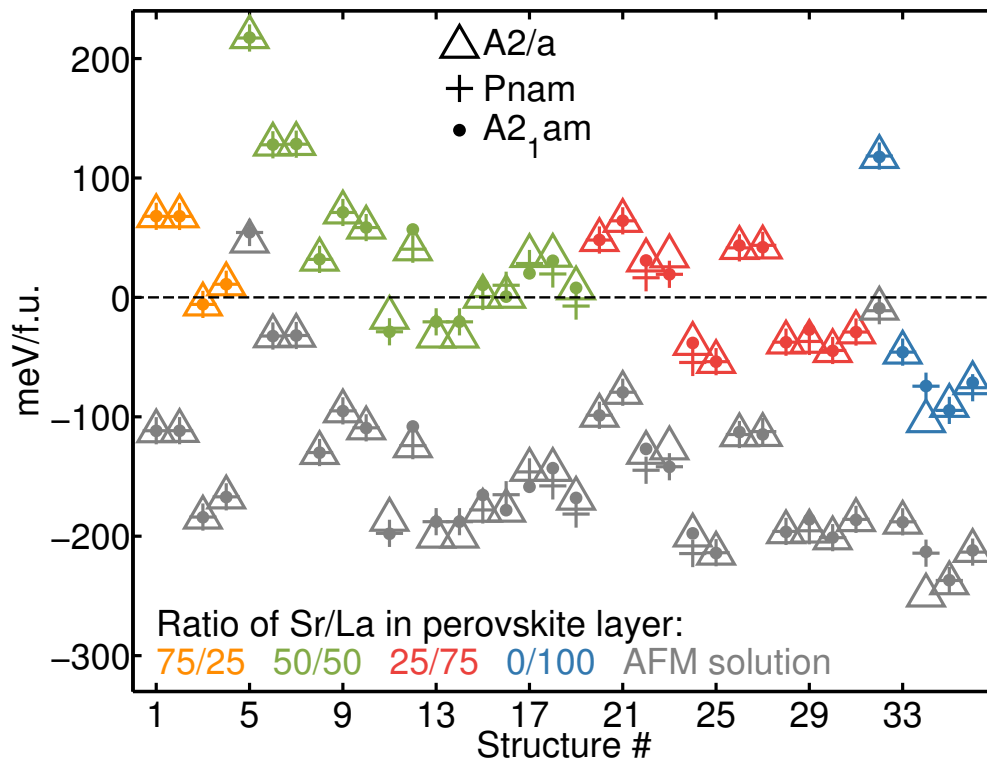


Figure 4.11: Calculated energies relaxed structures. The zero of energy is taken as the energy of the Amam structure with ferromagnetic spin ordering. Colored points have ferromagnetic ordering, while the corresponding gray point is the energy of the same structure with antiferromagnetic ordering.

In the specific case of $\text{La}_2\text{SrCr}_2\text{O}_7$ it was seen that the apparent energy penalty associated with distorting the CrO_6 octahedra couples together the A-cation distribution and the octahedral rotations. This suggests that if isovalent A-cation substitutions are made to $\text{La}_2\text{SrCr}_2\text{O}_7$ (e.g., Ca^{2+} for Sr^{2+} or a smaller lanthanide for La^{3+}) which lead to changes in the distribution of the AE^{2+} and Ln^{3+} cations between the A-sites in the perovskite and rock salt layers, there will be resulting changes to the cooperative rotations of the CrO_6 octahedra over and above those expected on the grounds of the changing tolerance factor. Thus, this

new coupling between A-site distribution and octahedral rotation could provide a route to realizing as yet unseen structural configurations and facilitate the preparation of phases with desired polar distortions. In addition there is an intriguing possibility that the coupling could be used in reverse to generate novel A-cation ordering schemes in Ruddlesden-Popper phases by utilizing the inflexibility of certain octahedrally coordinated B-cations.

CHAPTER 5

ANTIFERROELECTRICITY IN PbZrO_3

The relationship between the Pbam ground state and metastable polar structures in PbZrO_3 was investigated using first principles calculations. Both the R3c and I2cm structures are metastable polar structures which may be accessible by applying an electric field to Pbam. The I2cm structure is dynamically unstable to a rotation of its polarization and octahedral rotation axes from [110] to [111], resulting in R3c symmetry. A transition path calculated between Pbam and R3c passes through I2cm. This transition path combined with the instability of I2cm towards R3c reveals a simple structural relationship between Pbam and R3c. Several indirect transition paths from Pbam to R3c or I2cm were considered as well and their potential relevance to switching in a sample with preexisting domain boundaries is discussed. Additionally, an infinite set of low energy structures corresponding to various Pb cation displacement patterns was found. The relevance of these structures to several previous experimental results is discussed.

5.1 Introduction

On a macroscopic level, an antiferroelectric can be defined as a material which exhibits a characteristic double hysteresis loop under an applied electric field [67]. Despite much effort, a microscopic understanding of the macroscopic behavior has remained elusive [68, 69, 67, 70, 71]. One proposal is that a material will be antiferroelectric when it has a nonpolar ground state which can be driven into an energetically metastable polar phase via an applied electric field [67]. The prototypical antiferroelectric PbZrO_3 was studied with this proposal

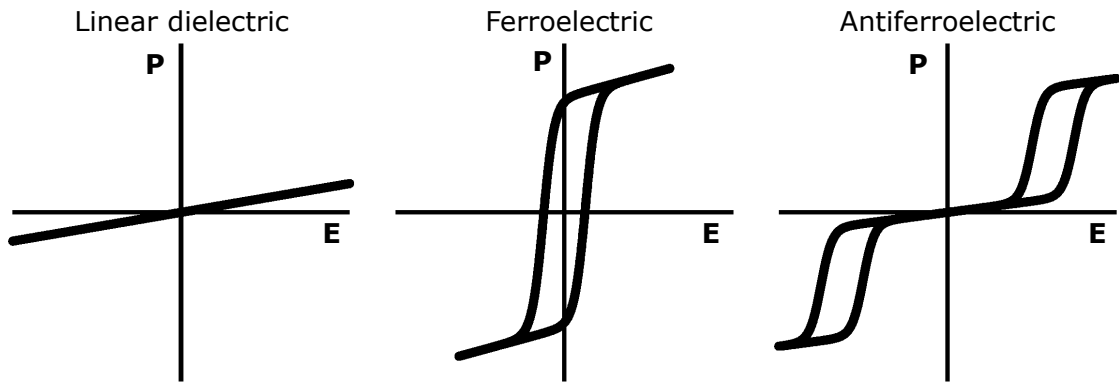


Figure 5.1: The polarization response to an electric field for linear dielectrics, ferroelectrics, and antiferroelectrics.

in mind.

A diagram of the antiferroelectric double hysteresis loop is shown in Figure 5.1. This type of hysteresis can be viewed as a combination of a linear dielectric response for smaller electric fields and a ferroelectric response for larger electric fields. The polarization response of antiferroelectrics stores a large amount of energy in the material under a large electric field, enabling antiferroelectrics to be used as high energy density capacitors [72]. The transition between low and high field regimes is often accompanied by large changes in properties other than the polarization, such as volume. Electric field control over this transition enables devices which use an electric field to control these other properties, such as actuators [73, 74] or tunable pyroelectrics [75].

PbZrO_3 was shown to be antiferroelectric in the 1950's [76] and is considered the prototypical antiferroelectric. PbZrO_3 and related materials have been studied extensively since then, both experimentally [77, 78, 79, 80, 81, 82, 83, 84, 70, 85, 86, 87, 88] and theoretically [89, 90, 91, 92, 93]. Important develop-

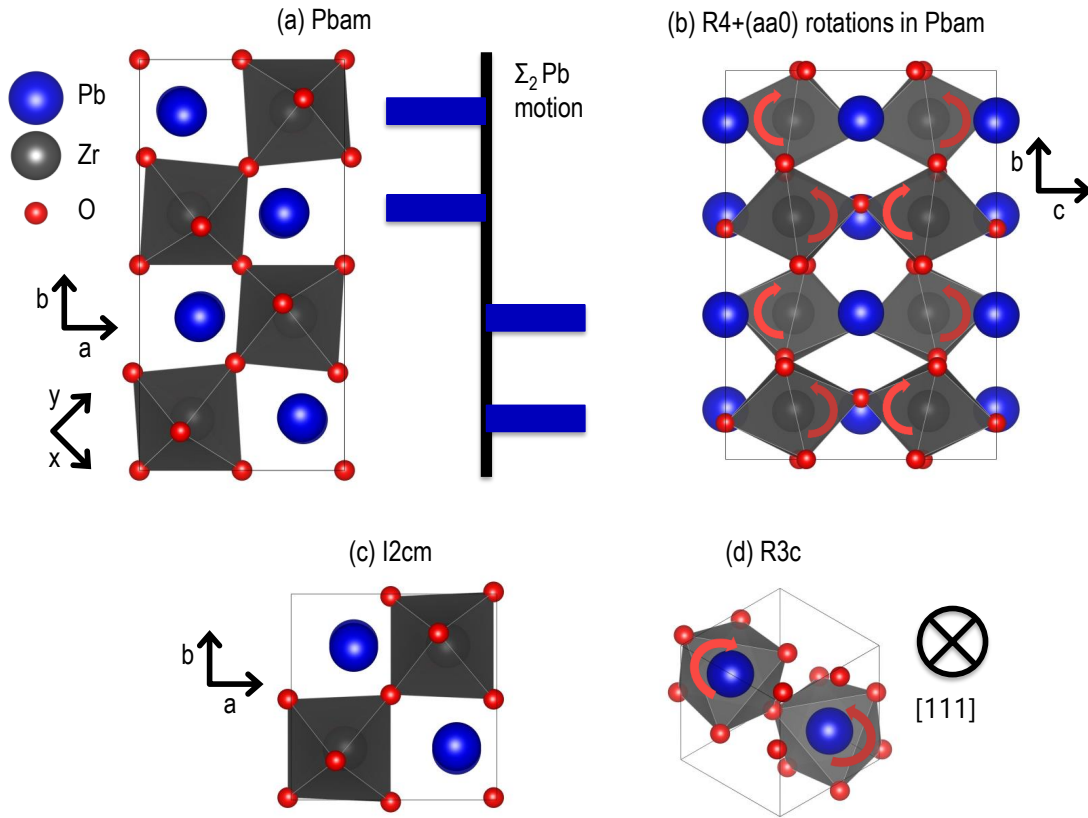


Figure 5.2: The crystal structure of several PbZrO_3 phases. (a) The ground state Pbam structure. The displacements of Pb due to the Σ_2 mode are highlighted. (b) A view of the R_4^+ mode in Pbam . In Glazer notation these rotations are $a^-a^-c^0$. (c) The $I2cm$ structure. (d) The $R3c$ structure.

ments were made in the 1990's which fully resolved the ground state crystal structure as Pbam [89, 79, 80]. The Pbam structure, shown in Figure 5.2(a), is a distorted perovskite structure with symmetry established by a combination of two primary order parameters: Σ_2 and R_4^+ . These order parameters are known to couple trilinearly to the S_4 mode [87], which also has a significant amplitude in the ground state structure. This trilinear coupling exists between the entire Σ and S lines, but only the coupling between the midpoints of these lines has been studied in detail from a theoretical viewpoint [92].

This study begins by addressing two questions: what are the possible metastable polar phases? and how is the nonpolar ground state related to these polar phases? While the ground state structure of PbZrO_3 is well established, a direct experimental determination of a metastable polar phase has not been performed. The phase diagram of $\text{PbZr}_{1-x}\text{Ti}_x\text{O}_3$ [83, 94] suggests that R3c is a metastable polar phase because it is stabilized at small x . The energy of the R3c and Pbam phases have been calculated using DFT and are very close in energy [89, 91, 92]. While R3c is an obvious candidate for the metastable polar structure, no assumption will be made about what the metastable polar phase is. Group theory was used to identify possible polar phases while density functional theory was used to determine which polar phases are low in energy. Several candidate metastable polar phases were found that may be possible to stabilize using an applied electric field. The relation between the ground state and these low energy polar phases is examined using a combination of group theory and climbing image nudged elastic band method (CI-NEB) calculations. The relationship between Pbam and R3c is unexpectedly simple given the differences in structure apparent in Figure 5.2.

The structural relationship between Pbam and R3c is chemically intuitive and led to the consideration of more complex transition paths between the two phases. This relation also suggests alternate displacement patterns of the Pb cations will be low in energy. An infinite set of low energy structures corresponding to the different displacement patterns was found. Both of these topics will be described in detail before discussing what these results suggest about PbZrO_3 and antiferroelectrics in general.

5.2 Methods

All first principles calculations were performed using projector augmented-wave potentials [47, 45] as implemented in the VASP package [43, 44]. PBEsol pseudopotentials [38] were used for all calculations. A plane-wave cutoff of 500 eV was found to give well converged results and is used throughout. Structural relaxations were considered converged once the Hellman-Feynmann forces were less than 10^{-3} eV/Å.

Several unit cells were used, requiring several k -point grids to be used. A $4 \times 4 \times 4$ k -point grid was used in both the 40 atom $2 \times 2 \times 2$ perovskite cell and in the experimental 40 atom $\sqrt{2} \times 2 \sqrt{2} \times 2$ perovskite cell (shown in Figure 5.2(a)). An approximately equivalent k -point grid was used for larger supercells of the form $\sqrt{2} \times n \sqrt{2} \times 2$ with $20n$ atoms. Convergence tests in each unit cell considered showed each such grid was well converged.

Energy barriers along transition paths were calculated using the CI-NEB method [51]. Transition paths were initialized so that distortions along the transition path are only switched when necessary. Without checking this the transition path can force, for instance, the octahedral rotation pattern to switch through zero and leads to an erroneously high energy barrier.

Space group names, symmetry adapted mode labels, and allowed trilinear couplings were determined using the *ISOTROPY* suite [95]. Symmetry analysis was carried out in terms of irreps but for ease of reading, Glazer notation is used and the direction of polarization is written in terms of the xyz Cartesian coordinate system shown in Figure 5.2(a). This notation can be easily mapped back to irreps, for example P_{xx0} is equivalent to $\Gamma_4^-(a,a,0)$. For clarity, space groups

are labeled with settings corresponding to the Pbam unit cell where possible. A conversion between these settings and their default settings is given in Table 5.1.

Formally, the Σ_2 irrep is twelve dimensional which corresponds to six orientational domains each with two degrees of freedom. A single orientational domain is sufficient to describe the ground state structure of PbZrO_3 . Transition paths were studied from the ground state to a polar state where the Σ_2 mode vanishes. For any of the other orientational domains of the Σ_2 irrep to become relevant, these distortions would need to emerge as a new primary order parameter and subsequently vanish along the transition path. Since the electric field does not couple directly to these degrees of freedom (in contrast with the polar Γ_4^- irrep) this situation is unlikely. Therefore, the orientational domains of Σ_2 have been neglected and Σ_2 is written as a two dimensional irrep throughout, corresponding to a single orientational domain. The remaining dimensions of Σ_2 may be relevant near orientational domain walls but consideration of these domain walls is beyond the scope of this work.

5.3 Search for polar structures

To search for metastable polar structures, phonons of the cubic $\text{Pm}\bar{3}\text{m}$ structure were calculated in a $2 \times 2 \times 2$ perovskite cell and the Pbam unit cell, which is $\sqrt{2} \times 2 \sqrt{2} \times 2$ times the primitive perovskite cell. Instabilities were relaxed into the structure along high symmetry directions (for example, irreps along $(a,a,0)$ but not $(a,b,0)$) for the polar Γ_4^- irrep, the Σ_2 irrep, and octahedral rotations (both R_4^+ and M_3^+). Phonons were calculated in each resulting structure and additional instabilities were relaxed in as before. This process was repeated until a dynam-

ically stable structure was found (or as in many cases a duplicate structure was found). For structures without the Σ_2 irrep, it is possible for multiple domains to be commensurate with the $\sqrt{2} \times 2 \sqrt{2} \times 2$ unit cell - for instance a rhombohedral structure such as R3m can have its polarization axis along either [111] or $[1\bar{1}1]$ which are at different angles relative to any single Σ_2 orientational domain. In other words, the 12 fold degenerate Σ_2 irrep is split by some other irreps. This splitting of Σ_2 was considered throughout the structure search by considering, as necessary, multiple domains of each structure in the $\sqrt{2} \times 2 \sqrt{2} \times 2$ unit cell.

A selection of the structures found with this search is shown in Table 5.1. Each of these structures correspond to a saddle point in the energy landscape but most are not dynamically stable. The relative energetics of structures are in reasonable agreement with previous first principles studies [91] which included a subset of the structures we considered. Pbam is the lowest energy structure found by this search, consistent with it being the observed experimental structure. The relaxed Pbam structure is compared with the low temperature experimental structure in Table 5.2. As expected, the R3c and Pbam structures are very close in energy. None of the relevant structures involve the M_3^+ octahedral rotation so this distortion is omitted from Table 5.1. Many additional structures aside from those in Table 5.1 were found but these do not have any effect on the results discussed here. For completeness, these structures are shown in Table A.1.

Adding a coupling term between the electric field and polarization (ie $\vec{E} \cdot \vec{P}$) to the DFT calculated energies provides an estimate of which structure has the lowest free energy under an applied electric field. A structure that can have the lowest free energy for some electric field could potentially be accessed by an ap-

Table 5.1: Calculated energy relative to the experimental Pbam ground state structure for several structures. Space group names are given using default settings and where possible alternate settings in the Pbam unit cell. The direction of the polar irrep (Γ_4^-), antiphase octahedral rotations (R_4^+), and the Σ_2 irrep are given for each structure. The modified Glazer notation [96] shows the direction of polarization and octahedral rotations. En. A and B are the energy of structure in a fixed unit cell and the fully relaxed unit cell.

Space Group	Alt. Settings	Γ_4^-	R_4^+	Σ_2	Mod. Glazer	Pol. ($\mu\text{C}/\text{cm}^2$)	Vol. ($\text{\AA}^3/\text{f.u.}$)	En. A (meV/f.u.)	En. B (meV/f.u.)
221 Pm $\bar{3}m$					$a_0^0 a_0^0 a_0^0$	0	71.08	278	278
53 Pmma	Pbmm			(0, a)		0	71.25	154	153
140 I4/mcm			(0, 0, a)		$a_0^0 a_0^0 c_0^-$	0	69.72	110	88
99 P4mm		(0, 0, a)			$a_0^0 a_0^0 c_+^0$	71	72.07	110	83
46 Ima2	Ima2	(0, 0, a)	(b, b, 0)		$a_0^- a_0^- c_+^0$	64	71.90	80	68
42 Fmm2		(0, 0, a)	(b, 0, 0)		$a_0^- a_0^0 c_+^0$	60	71.75	68	59
167 R $\bar{3}c$			(a, a, a)		$a_0^- a_0^- a_0^-$	0	69.81	70	59
38 Amm2	C2mm	(a, a, 0)			$a_+^0 a_+^0 c_0^0$	72	72.34	77	54
108 I4cm		(0, 0, a)	(0, 0, b)		$a_0^0 a_0^0 c_+^-$	51	70.74	77	54
74 Imma	Imcm		(a, a, 0)		$a_0^- a_0^- c_0^0$	0	69.78	58	44
55 Pbam	Pbam			(a, a)		0	72.23	62	43
160 R3m		(a, a, a)			$a_+^0 a_+^0 a_+^0$	75	72.61	46	28
57 Pbcm	Pbcm		(a, a, 0)	(0, b)		0	70.32	20	15
46 Ima2	I2cm	(a, a, 0)	(b, b, 0)		$a_+^- a_+^- c_0^0$	57	71.00	18	10
28 Pma2	P2cm	(a, a, 0)	(b, b, 0)	(c, 0)		26	70.64	15	8
161 R3c		(a, a, a)	(b, b, b)		$a_+^- a_+^- a_+^-$	59	71.03	1	0
55 Pbam	Pbam		(a, a, 0)	(b, b)		0	70.68	6	0

Table 5.2: Comparison of relaxed *Pbam* structure to the experimental structure at 10 K from Reference [97] shows excellent agreement.

	Relaxed			Experimental		
	a(Å)	b(Å)	c(Å)	a(Å)	b(Å)	c(Å)
	5.87230	11.77392	8.17769	5.8736	11.7770	8.1909
	x	y	z	x	y	z
Pb 4g	0.7009	0.1234	0	0.6991	0.1228	0
Pb 4h	0.7100	0.1283	0.5	0.7056	0.1294	0.5
Zr 8i	0.2421	0.1244	0.2497	0.2414	0.1248	0.2486
O 4g	0.2758	0.1577	0	0.2756	0.1560	0
O 4h	0.3006	0.0938	0.5	0.3011	0.0956	0.5
O 8i	0.0326	0.2620	0.2816	0.0317	0.2622	0.2798
O 4f	0	0.5	0.2021	0	0.5	0.2026
O 4e	0	0	0.2286	0	0	0.2293

plied field, assuming any energetic barriers can be overcome. Structures which could potentially be reached by an electric field were determined by considering structures in order from the lowest to highest energy and iteratively adding them to a list of potentially field accessible structures. For each structure, an applied electric field, \vec{E} , was assumed to be parallel to the structure's polarization, thereby maximizing the coupling to polarization. The estimated free energy of this structure was compared to that of every structure in the list of potentially accessible structures as a function of electric field amplitude. If the new structure had the lowest free energy for any electric field amplitude it was added to the list of potentially field accessible structures.

The first structure found by this process is R3c, which is added to the orig-

inally empty list of potentially field accessible structures. The next structure to consider is P2cm - its polarization is smaller than the polarization of R3c along the [110] direction, so the free energy of R3c will be lower than that of P2cm for any electric field. In contrast, the I2cm structure can have a lower free energy than R3c for relatively large electric fields oriented along its [110] polarization axis, so I2cm is the second structure added to the list of potentially field accessible structures. For electric fields up to roughly 4 MV/cm in *any* direction the only two polar structures which can be the ground state are R3c and I2cm. Allowing for even higher (potentially unrealistic) electric fields, R3m, C2mm, and P4mm become potentially accessible. This analysis has ignored the energetic barrier between structures which can only make it more difficult to drive a transition between structures so our analysis can safely rule out higher energy structures from further consideration.

At lower energies, it is possible for energy barriers to alter which structures may be accessed with an electric field. For instance if the energy barrier from Pbam to P2cm is small and there is a larger barrier to R3c, it may be possible to stabilize the P2cm structure before the energy barrier to R3c has been overcome. As will be discussed below, this does seem to be the case and P2cm may be accessible for a very narrow range of electric field strength. However, it is not expected that any other structures from Table 5.1 are accessible using an electric field even after accounting for energy barriers.

The Pbam, R3c, and I2cm structures are shown in Figure 5.2. Group-subgroup relations between Pm $\bar{3}$ m, Pbam, R3c, and I2cm structures are shown in the group-subgroup tree in Figure 5.3. Relevant subgroups of these three structures as well as several other structures which can be reached with the Σ_2

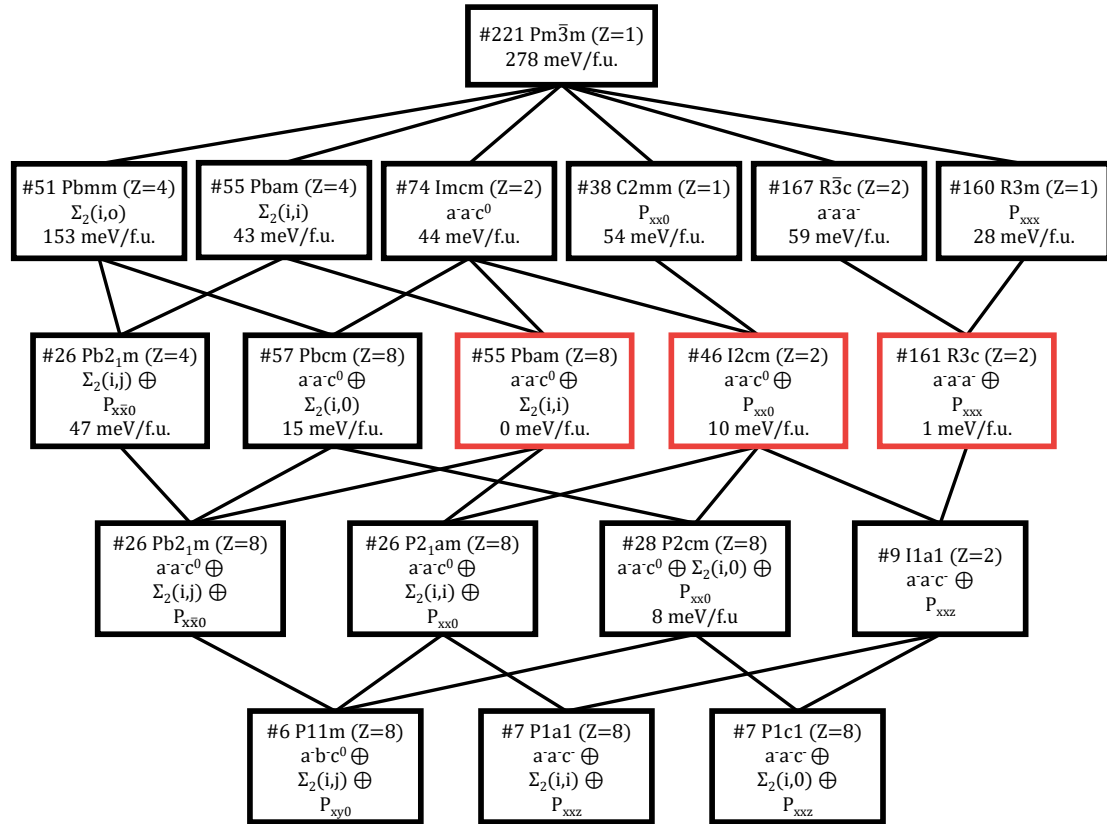
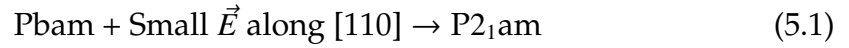


Figure 5.3: Group-subgroup relations between numerous relevant structures. The groups for the ground state and two candidate polar phases are shown in red boxes. The octahedral rotation pattern, polarization direction, and direction of Σ_2 allowed in each structure is given for each group. Energies are given for each group that we found a metastable structure (some structures relax into supergroups).

irrep are also included. The structures shown in this tree will be referenced throughout the rest of this chapter to help demonstrate the relations between various phases.

5.4 Transition path from Pbam to I2cm

Applying an electric field to the Pbam ground state may lead to either I2cm or R3c, as discussed in Section 5.3. Considering an electric field applied along the [110] pseudocubic axis (the a axis in Fig 5.2(a)) is a reasonable starting point as it is aligned with the large Pb cation displacements in Pbam from the Σ_2 distortion. This orientation of electric field is aligned with the polarization of the I2cm structure and should therefore favor it. Applying an electric field to the Pbam structure that is small enough to remain in the linear dielectric regime along this direction should induce a small polarization parallel to the electric field, thereby lowering the symmetry:



For a larger electric field along this direction the I2cm phase will become the most energetically favorable phase based on the analysis in Section 5.3. A trivial transition from Pbam to I2cm could proceed through Imcm, which is a common supergroup of the two structures. This would require the Σ_2 order parameter to switch off completely before the polar mode is induced, which leads to a relatively large energy barrier between the two phases. In contrast a transition path through a common subgroup of Pbam and I2cm would allow the Σ_2 order parameter to switch off as the polar mode increases in amplitude, almost certainly leading to a lower energy barrier. A reasonable guess at the transition path from Pbam to I2cm will therefore pass through P2₁am.

A CI-NEB calculation was performed from Pbam to I2cm with the intermediate structures along the transition path all having P2₁am symmetry. The cal-

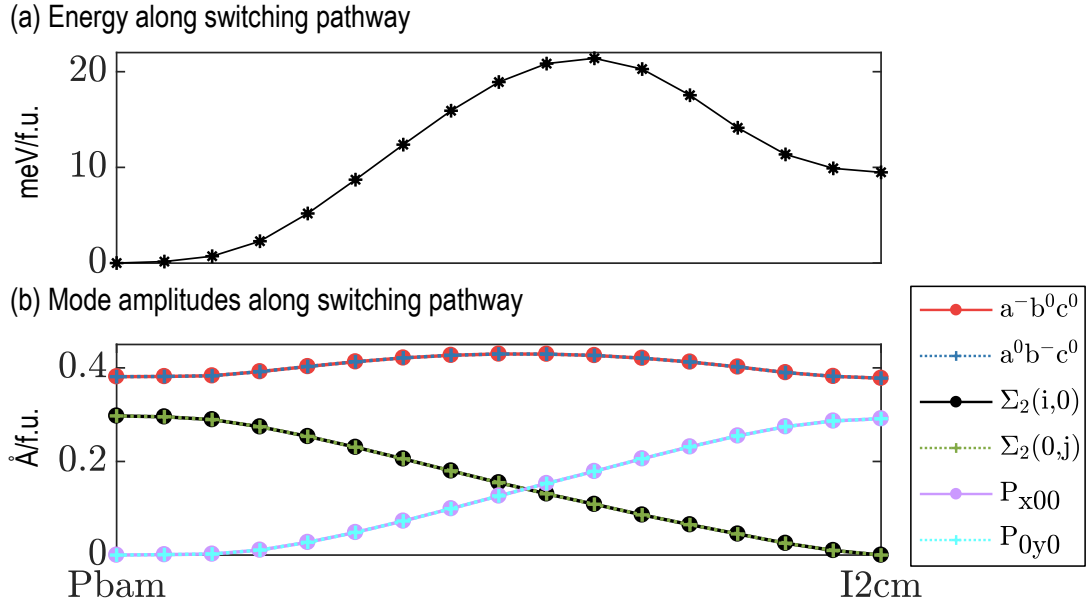


Figure 5.4: Energy and structural details of a transition path between Pbam and I2cm. The horizontal axis is a transition coordinate which merely signifies progression along the transition path. (a) Energy along transition path. (b) Amplitude of relevant distortions along the transition path.

culated energy barrier, shown in Figure 5.4(a), between these two phases is relatively low in energy at 21 meV/f.u. - lower in energy than most of the structures shown in Table 5.1. The evolution of the dominant distortions along this transition path are shown in Figure 5.4(b). The amplitude of the $a^-a^-c^0$ octahedral rotations is nearly identical in the Pbam and I2cm phases and barely changes along the transition path. As the amplitude of the polar Γ_4^- mode increases, the amplitude of the Σ_2 mode decreases until it is removed from the structure entirely.

This transition path represents a reasonable estimate of what may happen when an electric field is applied to the Pbam structure. The electric field couples linearly to polarization through an $\vec{E} \cdot \vec{P}$ term in the free energy. The am-

plitude of Γ_4^- is roughly proportional to \vec{P} so this term in the free energy implies that as the amplitude of \vec{E} is increases, the amplitude of Γ_4^- will increase in the structure. The biquadratic interaction between the Γ_4^- and Σ_2 modes, which has been shown to be repulsive [92], will limit how much Γ_4^- increases (as does a term quartic in the amplitude of Γ_4^-). The repulsive biquadratic term will also cause the amplitude of Σ_2 to decrease as the amplitude of Γ_4^- increases. Once the electric field causes the amplitude of Γ_4^- to become large enough, the system will have evolved into a region where it becomes energetically favorable for the Γ_4^- mode to spontaneously freeze in. In other words, the free energy can be further lowered by the soft Γ_4^- mode (in addition to a further lowering of the $\vec{E} \cdot \vec{P}$ term). This freezing in should happen rapidly, leading to the sharp nonlinearity observed in antiferroelectric hysteresis loops, and corresponds to the "nonpolar to polar" phase transition (quotes because at this point the "nonpolar" phase already has some field induced polarization). Within this picture it is important for both the nonpolar and polar modes (Σ_2 and Γ_4^-) modes to be unstable in the parent structure, otherwise there would be no explanation for the sharp increase in polarization at a critical electric field.

This transition path between Pbam and I2cm is relatively simple. In terms of irreps, the Σ_2 mode is exchanged for Γ_4^- . From a chemical point of view the transition primarily involves a reversal of half of the Pb cation displacements in Pbam. The transition between Pbam and I2cm will be discussed in more detail below, but first the transition from Pbam to R3c will be investigated.

5.5 Path from Pbam to R3c

A hypothetical transition path from Pbam to R3c is not as simple to determine as it was for the Pbam to I2cm transition path. The R3c structure, shown in Figure 5.2(d), is rhombohedral while Pbam is orthorhombic. There is not a simple and obvious path relating these two structures based on symmetry alone. To begin to thinking about the transition between Pbam and R3c it is insightful to think about the relation between I2cm and R3c.

The I2cm structure was found to be unstable during the search for metastable polar structures described in Section 5.3. The instability is a combination of $a^0a^0c^-$ octahedral rotations and a polarization along z. Adding this mode to the I2cm structure lowers the symmetry to I1a1, as can be seen in Figure 5.3. Full relaxation of the I1a1 structure results in one of its supergroups - the R3c structure. Other possible local minima consistent with I1a1 symmetry were searched for by performing relaxations starting from a wide range of initial structures with I1a1 symmetry but in each case the relaxation resulted in the R3c structure. This means the I2cm structure is dynamically unstable towards the R3c structure. A transition from I2cm to R3c is thus purely downhill in energy and can be interpreted as a rotation of the polarization and octahedral rotation axes from [110] to [111] as depicted in Figure 5.5.

The instability of I2cm to R3c means that once Pbam is driven into I2cm using an electric field, R3c can be trivially reached via the instability of I2cm. In other words, any transition path from Pbam to I2cm can also serve as a transition path from Pbam to R3c.

Applying a small electric field along the [111] pseudocubic axis of Pbam

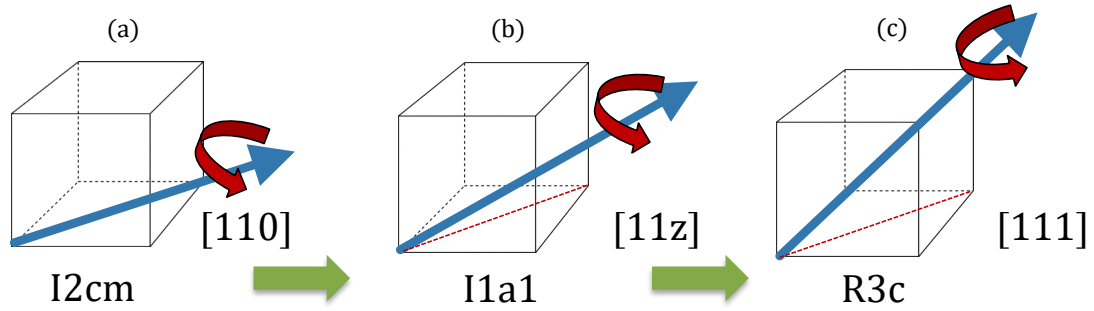


Figure 5.5: Schematic of how the instability of $I2cm$ leads to $R3c$. Red and blue arrows indicate the octahedral rotation axis and the polarization axis respectively. (a) Both axes are constrained along $[110]$, giving $I2cm$ symmetry. (b) Both axes are free to rotate along $[11z]$, giving $I1a1$ symmetry. (c) Both axes are constrained along $[111]$, giving $R3c$ symmetry.

leads to $P1a1$ symmetry. As can be seen in Figure 5.3, $P1a1$ is a common subgroup of both $Pbam$ and $R3c$, though the relation is not as direct as the relation between $Pbam$, $P2_1am$ and $I2cm$. A CI-NEB calculation between $Pbam$ and $R3c$ was performed with intermediate structures having $P1a1$ symmetry and the results are shown in Figure 5.6. The energy barrier is again roughly 21 meV/f.u.

Examination of the mode amplitudes across the transition path shows that neither the $a^0a^0c^-$ octahedral rotations nor the polarization along z have significant amplitude until the energy barrier has been fully overcome. These modes are free to relax in the CI-NEB calculation as the structures formally have $P1a1$ symmetry, however the calculation reveals that it is energetically preferable for these modes to have zero amplitude along most of the transition path. As indicated in Figure 5.6(b), the symmetry of the structure just before these modes begin to have significant amplitude is essentially $I2cm$.

In an electric field induced phase transition from $Pbam$ to $R3c$, an electric

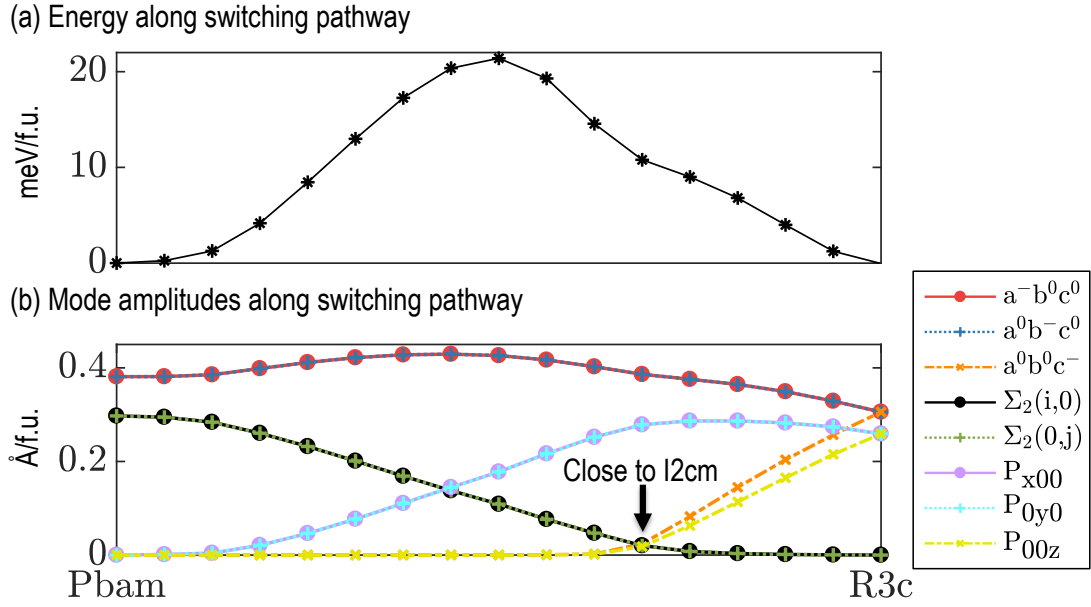


Figure 5.6: Energy and structural details of a transition path between Pbam and R3c. The horizontal axis is a transition coordinate which merely signifies progression along the transition path. (a) Energy along transition path. (b) Amplitude of relevant distortions along the transition path.

field along [111] should induce some polarization along [001] throughout the transition path because of the $\vec{E} \cdot \vec{P}$ term in the free energy. The CI-NEB calculation does not account for this term, but still provides significant insight into how Pbam may transition to R3c. The calculation shows that it is energetically preferable within DFT for the transition path from Pbam to R3c to first pass through I2cm. At this point, the instability of I2cm to R3c allows some additional energy lowering distortions. This means that starting from the Pbam structure, the energy penalty associated with various quartic terms in the free energy of an induced polarization is larger along [001] than [110]. An electric field applied along [111] will therefore induce a smaller polarization along [001] than [110] within the linear dielectric regime.

The combination of the instability between $I2cm$ towards $R3c$ and the relatively simple transition path from $Pbam$ to $I2cm$ reveals that the relationship between $Pbam$ and $R3c$ is not as complicated as one might expect based on their seemingly disparate crystal structures and symmetry.

5.6 Domain boundaries in real samples

Up to this point only the simplest possible transition paths between $Pbam$ and $I2cm/R3c$ where switching occurs simultaneously throughout a single domain crystal have been considered. In real switching processes, switching often occurs in steps or through motion and nucleation of domain boundaries. What can be learned about switching in such multidomain materials? Are these domain boundaries common in $PbZrO_3$? For simplicity, only translational boundaries will be considered.

Translational domains have been observed in $PbZrO_3$ within orientational domains using electron microscopy [98, 85, 99]. Examination of the images taken shows that translational boundaries can occur with density on the order of one per few 100 Å. This is a high density of domain boundaries - on average there are roughly 20 bulk unit cells between the boundaries. Recent studies achieved resolution high enough to extract the displacement of Pb cations away from high symmetry positions within the domain boundaries [85, 99]. In order to describe the distortions observed and explain how this work relates to these domain boundaries, structures are labeled based on the displacement pattern of the b planes of Pb ions. These displacements are parallel to the translational domain boundaries. As an example, a 4,4 displacement pattern corresponds to

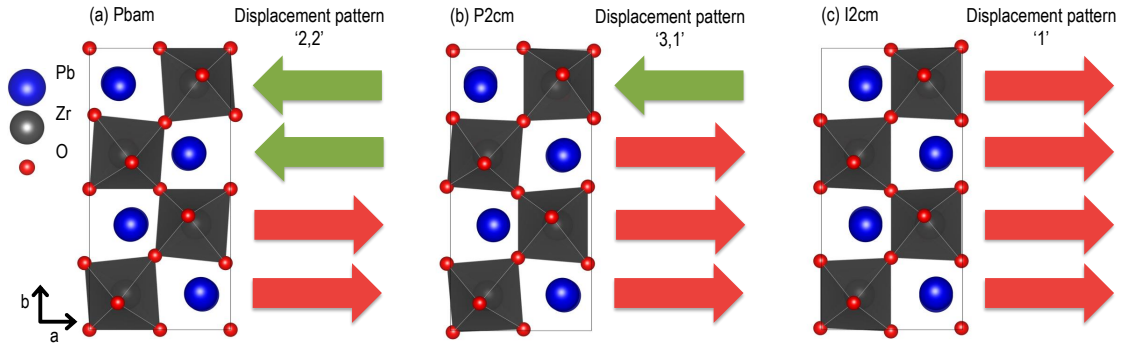


Figure 5.7: The displacement directions of the b planes of Pb ions are shown as arrows for several structures in the same unit cell. These structures can be labeled with a series of integers to denote the number of consecutive planes of Pb ions which displace in the same direction. (a) Pbam, (b) P2cm, (c) I2cm.

4 layers of Pb cations displacing in one direction followed by 4 layers displacing in the opposite direction. Several more examples are shown schematically in Figure 5.7.

Using this notation, the bulk Pbam structure follows a 2,2 pattern. Within the domain boundaries observed with electron microscopy, the extracted Pb displacements involve a 2,1,2,1 pattern which is surrounded by the bulk 2,2 pattern. The observed displacement pattern is ...,2,2,2,1,2,1,2,2,2,... and was interpreted as a π phase shift of the crystal structure across the domain boundary [85, 99].

A periodic structure using only the domain boundary structure can be generated to study this domain boundary. The 2,1,2,1 displacement pattern of Pb cations was frozen into the perovskite lattice along with octahedral rotations, using amplitudes from the relaxed Pbam structure. This results in a 60 atom structure with I2cm symmetry in a $\sqrt{2} \times 3\sqrt{2} \times 2$ unit cell (this structure is dis-

tinct from the I2cm structure discussed above). After relaxation, the 2,1,2,1 displacement pattern is essentially degenerate with the experimentally observed ground state. This very low energy may explain the high density of domain boundaries that have been observed in PbZrO₃.

While the 2,1,2,1 displacement pattern is present at the observed domain boundaries, its slightly larger unit cell makes it challenging to study. The simplest possible domain boundary structure is the 3,1 displacement pattern which must be present at any translational boundary. This is trivial to see by considering a deviation of a single plane of displacements from the 2,2 ground state. Regardless of how the displacements deviate from 2,2, there will be a set of four consecutive displacements which follow the 3,1 pattern when considered on their own and assuming periodicity.

The 3,1 displacement pattern is in fact present four times in the observed 2,1,2,1 domain boundary. One way of seeing this is to note that the observed π phase shift domain boundary could instead be interpreted as two domain boundaries each having a $\pi/2$ phase shift. In this case the displacement pattern becomes ...2,2,2 | 1,2,1 | 2,2,2,... where vertical lines have been inserted to separate regions in the crystal. There is a single bulk unit cell in the center (the 1,2,1 pattern is identical to the 2,2 bulk displacement pattern if one imagines repeating the 1,2,1 pattern periodically). There is a 2,1,2 displacement pattern bracketing each boundary. Selecting any 4 consecutive displacements within this displacement pattern gives the 3,1 pattern after accounting for periodicity. After generating and relaxing the 3,1 displacement pattern, as was done with the 2,1,2,1 pattern, the structure has P2cm symmetry and is 8 meV/f.u. above the ground state (this structure was also found in Table 5.1). The P2cm structure

is shown in Figure 5.7(b).

An atomically sharp domain boundary between Pbam and I2cm will also always have the 3,1 displacement pattern at the boundary, as shown in Figure 5.8. The polar domains in this sketch can grow by reversing the displacement direction of Pb displacements from down to up. Reversing a single Pb displacement at the boundary moves the domain boundary by a single layer and changes the schematic from Figure 5.8(a) to (b). Reversing another Pb displacement shifts the domain boundary by three layers because the next two displacements are already aligned with the polar region and the schematic returns to that of Figure 5.8(a), but shifted by four unit cells.

The 1,1 displacement pattern could be considered as a boundary instead of the 3,1 pattern. Both displacement patterns will be present whenever there is a deviation from the 2,2 pattern and at any boundary between Pbam and I2cm. However, the 1,1 displacement pattern is present (twice) in every primitive unit cell of the Pbam structure with 2,2 displacement pattern, which calls into question whether the 1,1 displacement pattern could be viewed as a domain boundary. The energy of the 1,1 displacement pattern is 27 meV/f.u. above Pbam, higher than the energy barrier between Pbam and I2cm calculated above. Given these observations it seems unlikely that the 1,1 displacement pattern can provide much information about switching so the 3,1 displacement pattern was studied as the simplest possible domain boundary.

The 3,1 displacement pattern also serves as a chemically intuitive candidate for an intermediate state in a multistep switching process between Pbam and I2cm, where the planes of Pb displacements switch independently. Multistep switching has been seen in ferroelectrics such as BiFeO₃ [100] and Ca₃Ti₂O₇

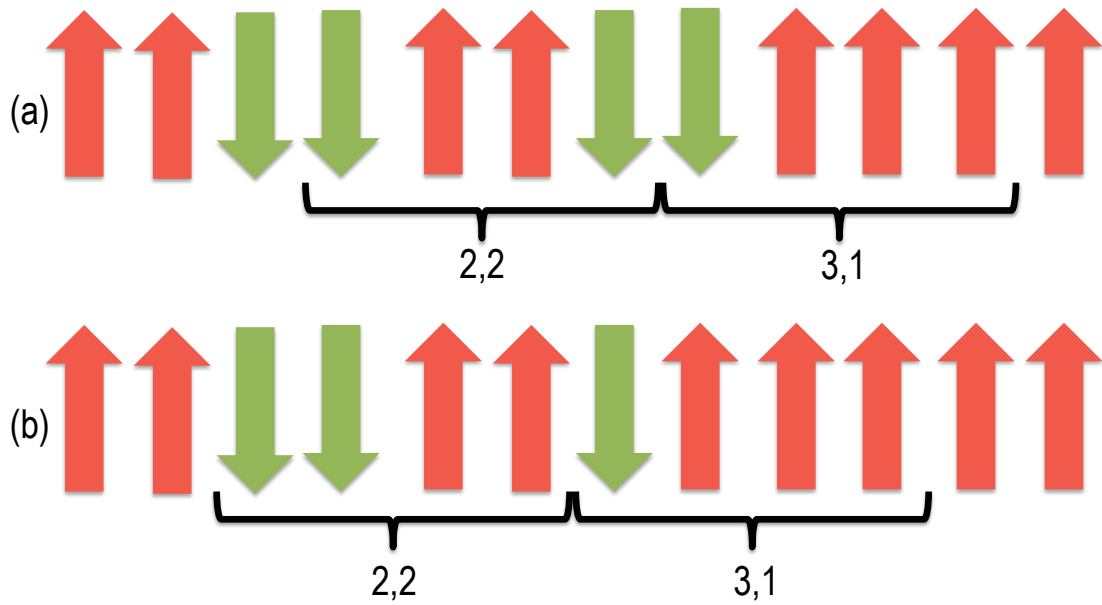


Figure 5.8: Diagrams of Pb displacements near an atomically sharp boundary between a domain of 2,2 displacements, which extend to the left of each diagram, and a polar domain, which extends to the right of each diagram. These are the only possible atomically sharp boundaries. A set of 3,1 displacements near the boundary is highlighted in each case. (a,b) Show the boundary with two and one antialigned Pb displacements adjacent to the polar region.

[101]. In these materials the structures being switched between are equivalent and related by an inversion of the polar mode. Multistep switching of such ferroelectrics can proceed via a rotation of the polar order parameter instead of directly reversing it. The situation is more complicated in PbZrO_3 because a nonpolar order parameter is being exchanged for a polar order parameter rather than simply rotating.

5.7 Domain boundaries and switching

Examining the symmetry of the 3,1 displacement pattern provides some insight into how it may be related to switching. Referring to Figure 5.3, the P11m structure is a common subgroup of Pbam and P2cm (the 3,1 displacement pattern). P11m symmetry can be reached starting from Pbam symmetry by rotating the Σ_2 order parameter away from its (i,i) direction and adding a polarization in the (x,y,0) plane. The symmetries which can be reached by combining $a^-a^-c^0$ octahedral rotations with an arbitrary direction of Σ_2 order parameter are shown in Figure 5.9, with and without a polarization along [110].

A hypothetical electric field induced multistep transition path from Pbam to I2cm could proceed as follows. An electric field applied along [110] to Pbam induces a small polarization lowering the symmetry to P2₁am. The Σ_2 order parameter then rotates from (i,i) to (i,0), passing through P11m symmetry and ending in P2cm symmetry. The Σ_2 order parameter is then turned completely off, leading to I2cm symmetry. P2cm symmetry was shown above to have a low energy metastable structure, so the P2cm structure could serve as an intermediate state along this multistep transition path. The symmetry along this path is drawn in Figure 5.9(b) and the (meta)stable crystal structures along the path are shown in Figure 5.7(a-c).

CI-NEB calculations were performed for transition paths between Pbam/P2cm, P2cm/I2cm, and P2cm/R3c. The energy and amplitude of relevant distortions along these paths are shown in Figure 5.10. The overall energy barrier of the multistep indirect paths between Pbam/I2cm and Pbam/R3c are a couple meV/f.u. lower than the direct path.

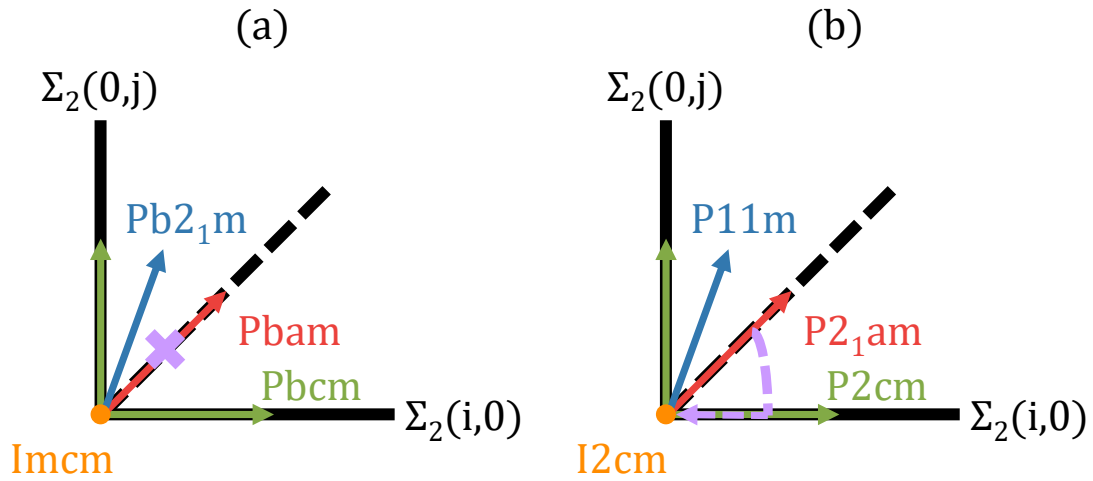


Figure 5.9: Space groups accessible as a function of $\Sigma_2(i, j)$. Rotating by 90 degrees in the (i, j) plane produces an equivalent structure so only the first quadrant is shown. $i=j$, $i=0$, and $i \neq j$ are shown in red, green, and blue respectively. The $i=j=0$ case is shown in orange. (a) Accessible space groups with a $a^-a^-c^0$ octahedral rotations included in the structure. The ground state $Pbam$ structure is indicated with a purple X. (b) Accessible space groups with a $a^-a^-c^0$ octahedral rotations and a P_{xx0} polarization. This mimics applying an electric field along $[110]$ to the phases shown in (a). A possible transition path from $Pbam$ to $P2cm$ to $I2cm$ is shown as the purple dashed line.

The distortions along the transition path from $Pbam$ to $I2cm$ evolve as expected based on symmetry: the Σ_2 order parameter is rotated by turning $\Sigma_2(0, j)$ off while an in plane polarization develops, with the other distortions remaining mostly unchanged. Progressing from $P2cm$ to $I2cm$ is similar - Σ_2 is switched completely off as the in plane polarization increases. The path from $P2cm$ to $R3c$ is again similar, except for the additional P_{00z} and $a^0a^0c^-$ distortions. In this case the out of plane polarization and rotations develop a nonzero amplitude but remain relatively small until the energy barrier between $P2cm$ and $R3c$ has been overcome. This is reminiscent of the direct $Pbam$ to $R3c$ transition path

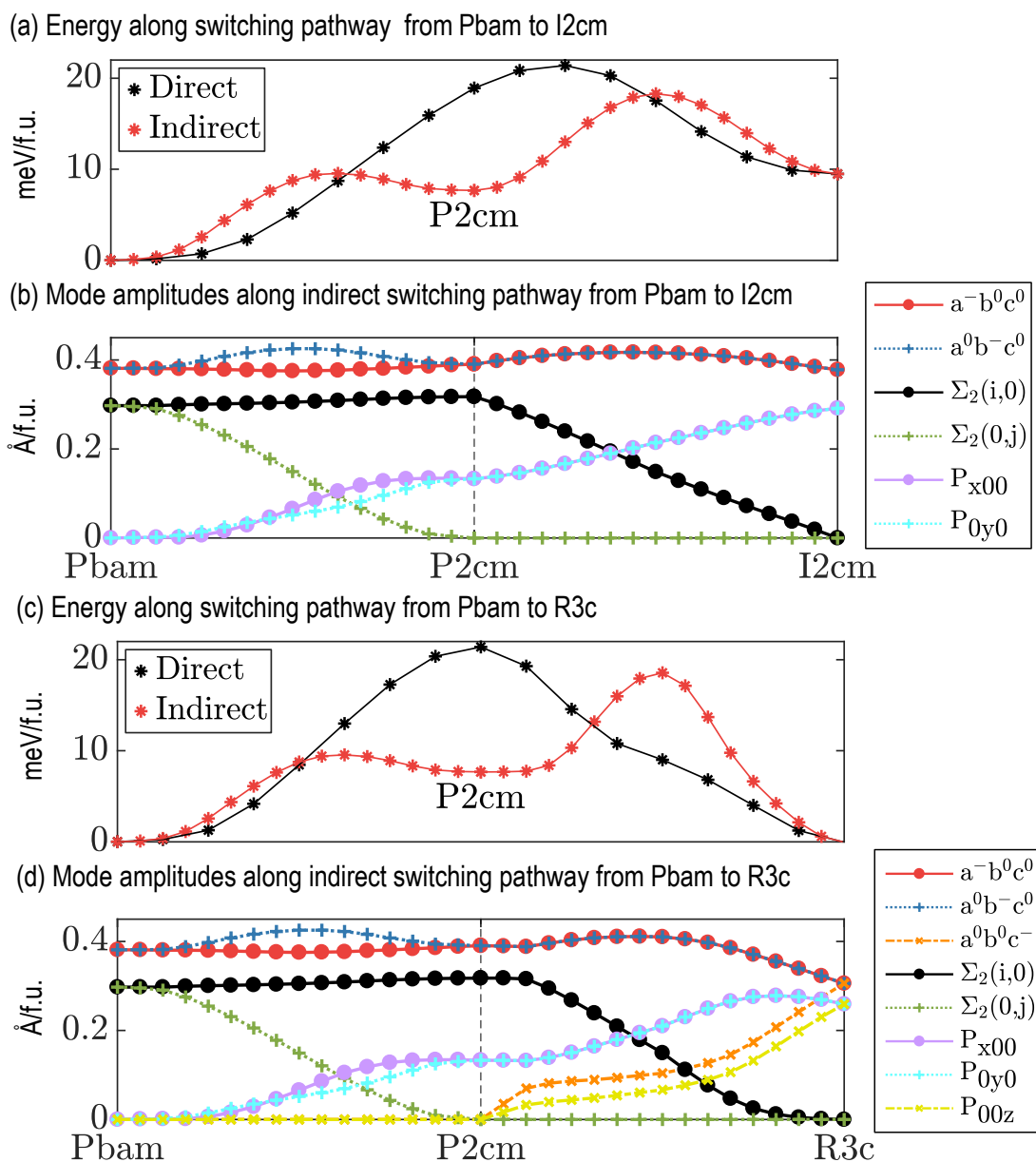


Figure 5.10: Energy and structural details of a multistep transition path between Pbam and I2cm or R3c. The horizontal axis in each plot is a transition coordinate which merely signifies progression along the transition path. (a) Energy along the indirect transition path from Pbam to I2cm. The energy of a direct transition path is included for comparison. (b) Amplitude of relevant distortions along the indirect transition path. (c,d) Same as (a,b) except for a path from Pbam to R3c.

in which the out of plane polarization and rotations are essentially zero until something very close to the I2cm structure is reached. It seems that the out of plane polarization and rotations become more energetically favorable as the in plane Pb displacements become more aligned (ie 1 favors them more than 3,1 which favors them more than 2,2). This idea is explored further in Section 5.8.3.

The various transition paths considered serve as reasonable first approximations for what may happen in a crystal as it is switched. The direct transition path from Pbam to I2cm (or R3c) can be viewed as a simultaneous bulk switching mechanism. The transition path from Pbam to P2cm can be interpreted as the creation of a domain boundary. The transition path from P2cm to I2cm (or R3c) is a reasonably proxy for moving a domain boundary to grow a polar region. The energy barriers for each of these transition paths are similar so it is not obvious any one of these mechanisms will be strongly favored over the others. However, what should really be compared is the electric field required to overcome the energy barrier. This can be estimated by adding an $\vec{E} \cdot \vec{P}$ term to the energy, the electric field needed to drive structure A to structure B is then

$$|\vec{E}| = \frac{U_S - U_A}{\hat{E} \cdot (\vec{P}_S - \vec{P}_A)} \quad (5.2)$$

where \vec{E} , U , and \vec{P} are the electric field, DFT calculated energy, and polarization. Subscripts indicate the structure with S referring to the saddle point structure between A and B . This equation sets the free energy of structure A and S equal, so that the energy barrier from A to B is exactly canceled by the $\vec{E} \cdot \vec{P}$ term. Once this happens the system is free to relax into structure B and further lower its energy.

The estimated electric field required to overcome the energy barrier along each of the transition paths considered is given in Table 5.3. Counter intuitively,

Table 5.3: Estimated electric field strength in MV/cm required to overcome energy barriers along each transition path.

Transition path	$\vec{E} \parallel [110]$	$\vec{E} \parallel [111]$
Pbam to I2cm	1.38	1.69
Pbam to R3c	1.40	1.71
Pbam to P2cm	1.27	1.55
P2cm to I2cm	1.53	1.88
P2cm to R3c	1.67	1.45

the field required to switch from Pbam to R3c is larger along [111] than [110]. This happens because the transition path effectively passes through I2cm so the polarization of the saddle point structure is also along [110], which has a weaker coupling to fields oriented along [111].

Within this approximation, the difference in electric field required to overcome the direct and indirect paths are within roughly 10%. This small difference suggests the indirect and direct paths are roughly equally favorable under an applied electric field. The energy barrier between Pbam and P2cm always requires the smallest electric field to overcome, regardless of electric field direction which may mean the P2cm phase can be stabilized within a narrow range of electric field amplitudes.

With these ideas in mind, some statements can be made about how switching may proceed by imagining a single orientational domain of PbZrO_3 . Switching may occur via any combination of: motion of preexisting domain boundaries, creation and motion of domain boundaries, or single phase switching. Each of these mechanisms should become active at roughly the same electric field. Since there are multiple paths for switching to take place, switching should be robust

to the effects of defects. For instance if a domain wall is pinned by some defect, the rest of the sample should still be able to switch just as readily using the other switching mechanisms.

5.8 Are there other low energy structures?

Based on the structure of P2cm and its low energy, it is natural to wonder whether other displacement patterns of the Pb cations are also low in energy. As discussed above, it is possible to label such structures with a series of integers. A structure was constructed for each unique displacement pattern commensurate with an 80 atom unit cell or smaller (of the form $\sqrt{2} \times n \sqrt{2} \times 2$ times the primitive perovskite cell). Starting from the cubic Pm $\bar{3}$ m structure each Pb cation was displaced by an amplitude equal to that of the Pb displacements in the relaxed Pbam ground state, while following the specific displacement pattern. $a^-a^-c^0$ octahedral rotations were also added to the structure, with amplitude equal to that of the relaxed ground state. The resulting 24 structures were each relaxed and the resulting energies are shown in Figure 5.11. In each case the relaxed structure maintained its initial displacement pattern and is a distinct structure. Most of these structures have energy between that of the Pbam and I2cm structures.

The alternate displacement patterns combined with $a^-a^-c^0$ octahedral rotations leads to several different space groups which can allow a large number of degrees of freedom in the structure. To gain insight into which of these degrees of freedom, the distortions in the relaxed structures were closely examined using an expansion of the free energy.

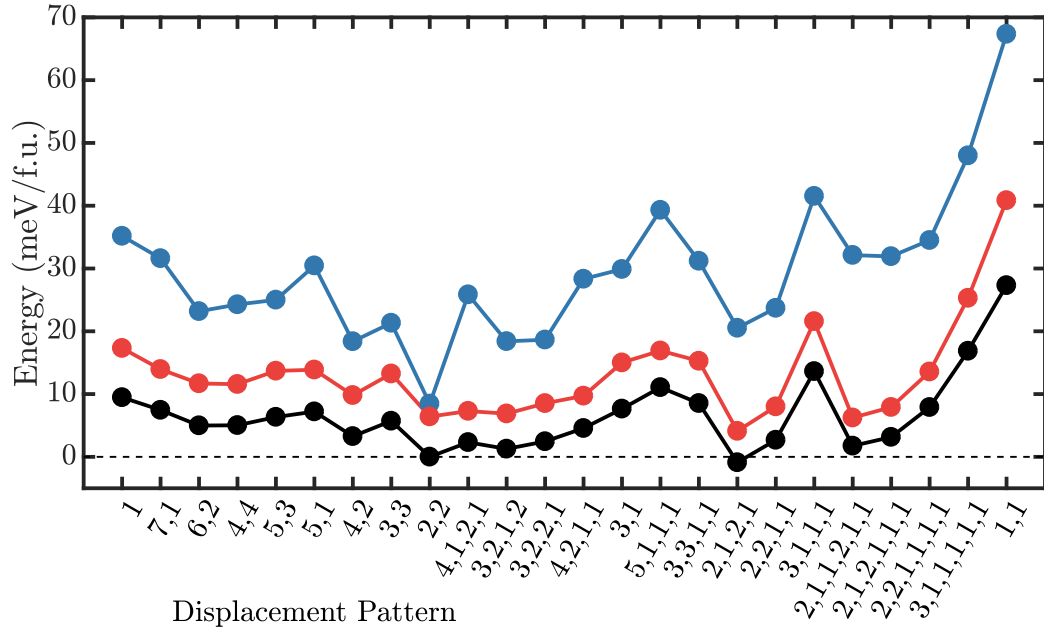


Figure 5.11: Energetics of structures with various displacement patterns. Lines are included for ease of reading but have no physical significance. Black, red, and blue points are the energy of fully relaxed, relaxed in fixed cubic unit cell, and of an unrelaxed structure generated based on the structural model.

5.8.1 Free energy couplings

Using the cubic $Pm\bar{3}m$ perovskite structure as a high symmetry reference structure, an expansion of the free energy admits many terms which involve even powers of the symmetry adapted modes. Second order terms involve only a single symmetry adapted mode and can have a positive or negative coefficient, depending on whether a mode can lower the energy of $Pm\bar{3}m$. The fourth order terms can involve either one or two symmetry adapted modes, being proportional to either Q_A^4 or $Q_B^2 Q_C^2$. In $PbZrO_3$, the coefficients of these fourth order terms were all found to be positive. Based on these even terms alone, the energy landscape for a single symmetry adapted mode is relatively simple - it

is either a harmonic minima or a double well with two local minima at nonzero amplitude.

The perovskite structure, however, also admits a number of trilinear couplings in the free energy between symmetry adapted modes. Such couplings have been shown to stabilize ground state structures [102, 103] and can be used to design and understand ferroelectric materials [6, 7, 104]. An allowed trilinear coupling involving the Σ_2 and S_4 branches can be determined using *ISOTROPY* [95]

$$\mathcal{F} \propto Q_{R_4^+} Q_{\Sigma_2^k} Q_{S_4^{1/2-k}}, \text{ for } 0 < k < 1/2 \quad (5.3)$$

where Q_{\square} is the amplitude of the \square distortion in a structure and the superscripts on the Σ_2 and S_4 indicate the position along the Σ or S lines. These couplings are allowed in each of the displacement patterns considered, often with several terms entering the free energy. For instance, the 2,1,1,2,1,1 displacement pattern requires a mixture of $\Sigma_2^{1/8}$ and $\Sigma_2^{3/8}$ modes and therefore allows a pair of the above trilinear terms in the free energy. The trilinear coupling between these branches has been noted elsewhere [87] and the $k = \frac{1}{4}$ in Eq. (5.3) coupling has been credited with stabilizing the experimental structure [92].

5.8.2 Structural model

A structural model was developed which accurately predicts these structures and demonstrates which degrees of freedom are most important. The model is built on two dominant structural motifs that are present in each low energy structure: (1) the displacement of Pb cations and (2) $R_4^+(a,a,0)$ octahedral rotations. The amplitude of $R_4^+(a,a,0)$ octahedral rotations is nearly identical in each

of the relaxed displacement patterns. The Pb cation displacements are always approximately the same magnitude and the specific ordering does not have a large effect on the energy as long as the displacement is along the rotation axis. These two structural motifs fully establish the symmetry of each structure, which allows a more detailed structural model to be made by using symmetry arguments to determine the amplitudes of more subtle structural distortions.

Starting from these two distortions it is possible to accurately predict the amplitude of every other distortion involved in the trilinear couplings given in Equation 5.3 (there are several degrees of freedom allowed by the Σ_2 and S_4 distortions). The energies of a structure following each displacement pattern was calculated for various sets of degrees of freedom to show the relative importance of each set and to explain how the structural model works. The development of this model uses ideas similar to Reference [105] which relates the various structures observed in $\text{PbZr}_{1-x}\text{Ti}_x\text{O}_6$ using symmetry analysis. For simplicity, all structures discussed in this section are constrained to the relaxed cubic unit cell. Unit cell relaxation does not significantly alter these results.

The first ingredient in the structural model is the displacement of Pb ions. Allowing only the Pb ions to displace in PbZrO_3 raises the energy relative to $\text{Pm}\bar{3}\text{m}$ except in the 1 displacement pattern, as shown by the yellow points in Figure 5.12, consistent with the self force constant of Pb ions being positive [106]. Adding octahedral rotations to these structures lowers the energy by about 145 meV/f.u., *independent* of the displacement pattern, as shown by the purple points in Figure 5.12.

The majority of Pb motion in the experimental Pbam structure is contained in the $\Sigma_2^{1/4}$ mode and is directed along the a axis. The symmetry of this distortion

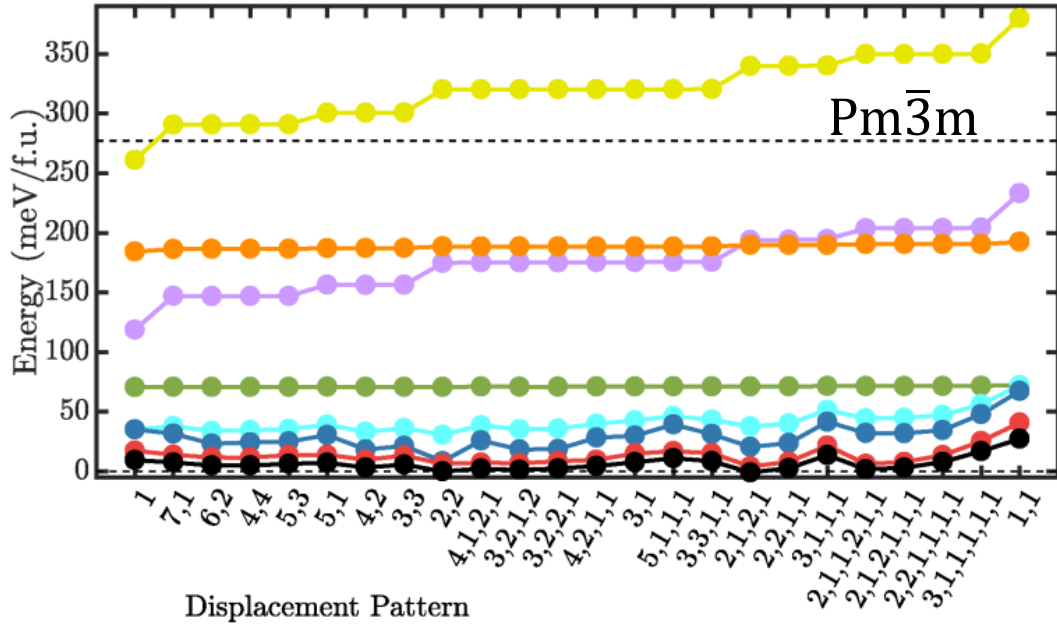


Figure 5.12: Calculated energies for various elements of the structural model relative to the cubic $Pm\bar{3}m$ ground state structure. From high to low energy the curves are: only Pb displacing, Pb/Zr/O displacing against each other, Pb displacing and R_4^+ , Pb/Zr/O displacing against each other and R_4^+ , full estimate of Σ_2^k and R_4^+ , full estimate of Σ_2^k and $S_4^{(1/2)-k}$ and R_4^+ , relaxed structure in fixed cubic unit cell, and the fully relaxed structure (yellow, orange, purple, green, light blue, dark blue, red, and black respectively).

also allows the apical oxygen and Zr ions to displace along the a axis. The model assumes that within each b plane the Pb and Zr ions move against the apical oxygen ions by an amount equal to that in the experimental structure, with the direction dictated by the Pb displacement pattern. The energies of these distortions with and without octahedral rotations are shown by the green and orange points in Figure 5.12, again showing the displacement pattern is independent of the octahedral rotations.

The Σ_2 mode also allows for M_2^+ and M_3^+ like distortions. These distortions

involve the equatorial oxygen atoms which are located halfway between each b plane of Pb cations. The amplitudes of these distortions were determined by writing the amplitude of Σ_2 distortions along b as a Fourier series. The coefficients of this series were defined so that the series would reproduce each particular Pb displacement pattern (Γ_4^- and M_5^- , which can be viewed as endpoints of the Σ line, are included as terms in the Fourier series to have a complete basis set for the Pb displacements). The amplitude of the resulting Fourier series halfway between each b plane of Pb ions was used to set the amplitude of distortions of the equatorial oxygen ions relative to the experimental Pbam structure. The inclusion of these two distortions in the model leads to the energies shown in light blue in Figure 5.12, significantly lowering the energy for each off-centering pattern (except for the 1,1 pattern which is unchanged by symmetry). This approach treats the multiple modes allowed by the Σ_2 mode as a single distortion wave with amplitude defined by the displacement pattern of Pb ions. This approach differs from the usual effective Hamiltonian approach which would average the displacements of adjacent b planes to determine the motion of equatorial oxygen atoms. In general, this Fourier series approach produced lower energy structures that were closer to the relaxed structures than this averaging method.

By assuming the trilinear coupling has the same strength along the entire Σ line, the S_4 distortions can be determined using Eq. (5.3) because the amplitude of R_4^+ is fixed and the amplitude of Σ_2^k is set by the displacement pattern. Each $Q_{S_4}^{1/2-k}$ is therefore determined by $Q_{\Sigma_2^k}$ which are simply related to the coefficients of the Fourier series. Inclusion of these distortions completes the structural model and results in the energies shown in dark blue in Figure 5.12. On average the model yields structures that are within 23 meV/f.u. of the relaxed ground

state, which is 271 meV/f.u. below the $Pm\bar{3}m$ reference structure, *without any relaxation*. The structural model accurately captures structural distortions that account for about 90% of the energy drop away from the cubic structure, emphasizing the dominant nature of the R_4^+ , Σ_2 , and S_4 modes in $PbZrO_3$. As this model is based on a reciprocal space description of the distortions and has considered points throughout the Brillouin zone, the structural model demonstrates that $PbZrO_3$ has a low energy structure for an arbitrary displacement pattern of Pb ions.

The structural model is based on irreps which are defined in reciprocal space and can therefore generate a structure for an arbitrary displacement pattern defined in real space. The model was used to generate the 152 possible additional unique displacement patterns commensurate with 100 or 120 atom unit cells ($n=5$ or 6). Each of these structures was relaxed and gave results similar to that of the smaller unit cells considered above: many very low energy structures. The model significantly accelerated the relaxation process because the structures generated by the model are close to the relaxed structure. Based on this, the structural model could prove useful when attempting to perform structural refinements based on diffraction data by providing a good estimate of the structure for a given displacement pattern.

5.8.3 Are these structures stable?

Based on the instability of the $I2cm$ structure, it is natural to think the other displacement patterns may also exhibit instabilities. Zone center phonon calculations were performed for each of the relaxed displacement patterns shown in

Fig. 5.12 to check for instabilities. Detailed examination of the phonon calculations revealed that every displacement pattern considered has two phonons which involve either $a^0a^0c^-$ or $a^0a^0c^+$ octahedral rotations with frequency below 35 cm^{-1} . The $a^0a^0c^-$ octahedral rotations tend to be softer and many of the displacement patterns are not dynamically stable with respect to this distortion.

The instability of various displacement patterns towards $a^0a^0c^-$ octahedral rotations can be understood by focusing on displacement patterns of the form nm with $m \leq n$. In each of these structures n is the maximum number of consecutively aligned displacements Pb ions and in the limit $n \rightarrow \infty$ these displacement patterns all become the 1 displacement pattern. Phonons were calculated for every unique nm displacement pattern that could be simulated in a 120 atom or smaller unit cell. The lowest frequency $a^0a^0c^-$ phonon in each nm type structure varies linearly with $1/n$ as shown in Fig. 5.13. This relation can be justified by noting that the coherence of $a^0a^0c^-$ octahedral is interrupted along the b axis when adjacent Pb ion displacements are antialigned. Thus for larger n the $a^0a^0c^-$ octahedral rotations become more favorable as there is more space in the structure for the rotations to occupy before their coherence is broken. While this instability is strongest in the 1 displacement pattern, similar instabilities exist in the other displacement patterns with large regions of aligned Pb displacements.

These instabilities are not directly accounted for in the structural model but can be easily relaxed into any of the structures by adding a small $a^0a^0c^-$ octahedral rotation. The instabilities are not very strong and do not lower the energy of any displacement pattern by a large amount. The strongest instability is in the 1 displacement pattern and lowers the energy by roughly 10 meV/f.u. (the energy difference between I2cm and R3c). The overall trend observed in Fig-

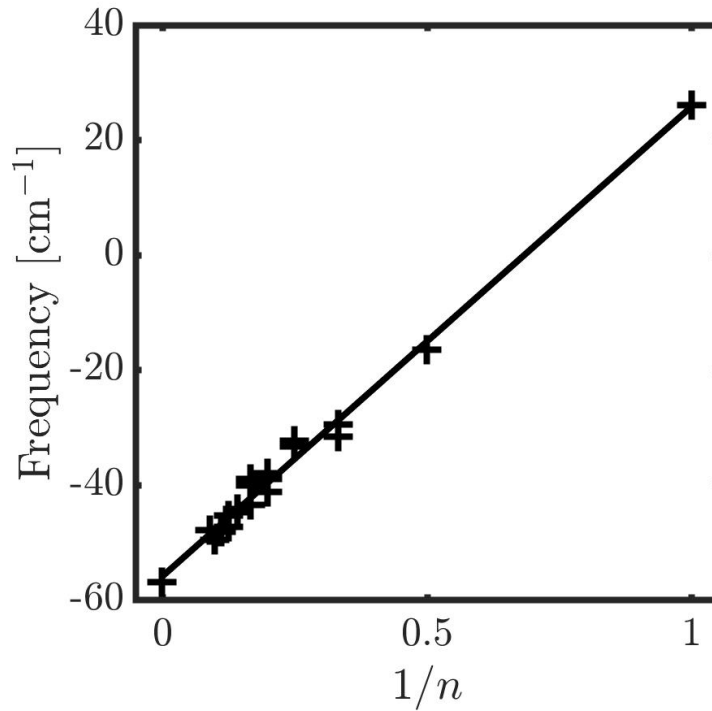


Figure 5.13: Frequency of the most unstable phonon involving $a^0a^0c^-$ in structures with displacement pattern of the form nm . Phonon calculations were performed in unit cells equivalent to that of the fully relaxed cubic cell. The 1 displacement pattern is treated as $n = \infty$. Black line is linear fit to all data points.

Figure 5.11 is not changed by these instabilities - the displacement patterns are all close in energy with or without this instability.

5.8.4 Quantifying the flatness of the energy landscape

The energy landscape of PbZrO_3 is relatively flat with respect to the displacement patterns, as shown in Figure 5.12. A zoomed in view of the energies of structures with only Pb/Zr/O displacing in each displacement pattern is shown in Figure 5.14. These energies vary with the displacement pattern but there are

several clear plateaus where the energy is effectively degenerate within the precision of the calculations. By defining a domain wall as anywhere two adjacent displacements are antialigned, the number of domain walls per layer can be calculated as the length of a displacement pattern name divided by its sum (the 4,2 pattern thus has $2/(4+2)=1/3$ domain walls per layer).

The number of domain walls per layer is linearly related to the energy of structures with Pb/Zr/O displacing against each other, showing there is a constant energy cost for each domain wall in the structure. The slope of the line in Figure 5.14 is roughly $8 \text{ layer meV} \times \text{layers/f.u.} \times \text{domain walls}$ which is equivalent to $4 \text{ meV/domain wall}$ because there are 2 formula units in each layer.

Similar plots can be made for structures that include $a^-a^-c^0$ as well as Pb/Zr/O displacing against each other. These domains are much more relevant to PbZrO_3 because the octahedral rotations are included. Octahedral rotations were excluded in Figure 5.14 in order to better demonstrate the distinct plateaus. With rotations included the resulting slope is $0.8 \text{ meV/domain wall}$, making the energy differences between plateaus nearly as small as the energy precision from these calculations. This slope provides some quantification of how flat the energy landscape is in PbZrO_3 .

Several simple calculations were performed for AZrO_3 materials to calculate an equivalent energy cost of a domain wall in these materials. The internal coordinates for the structures in each case were identical to the structures used in PbZrO_3 - that is Pb was simply change to another element. Two unit cells were used: the PbZrO_3 unit cell and a relaxed AZrO_3 unit cell. The resulting energies are shown for each set of calculations in Figure 5.15.

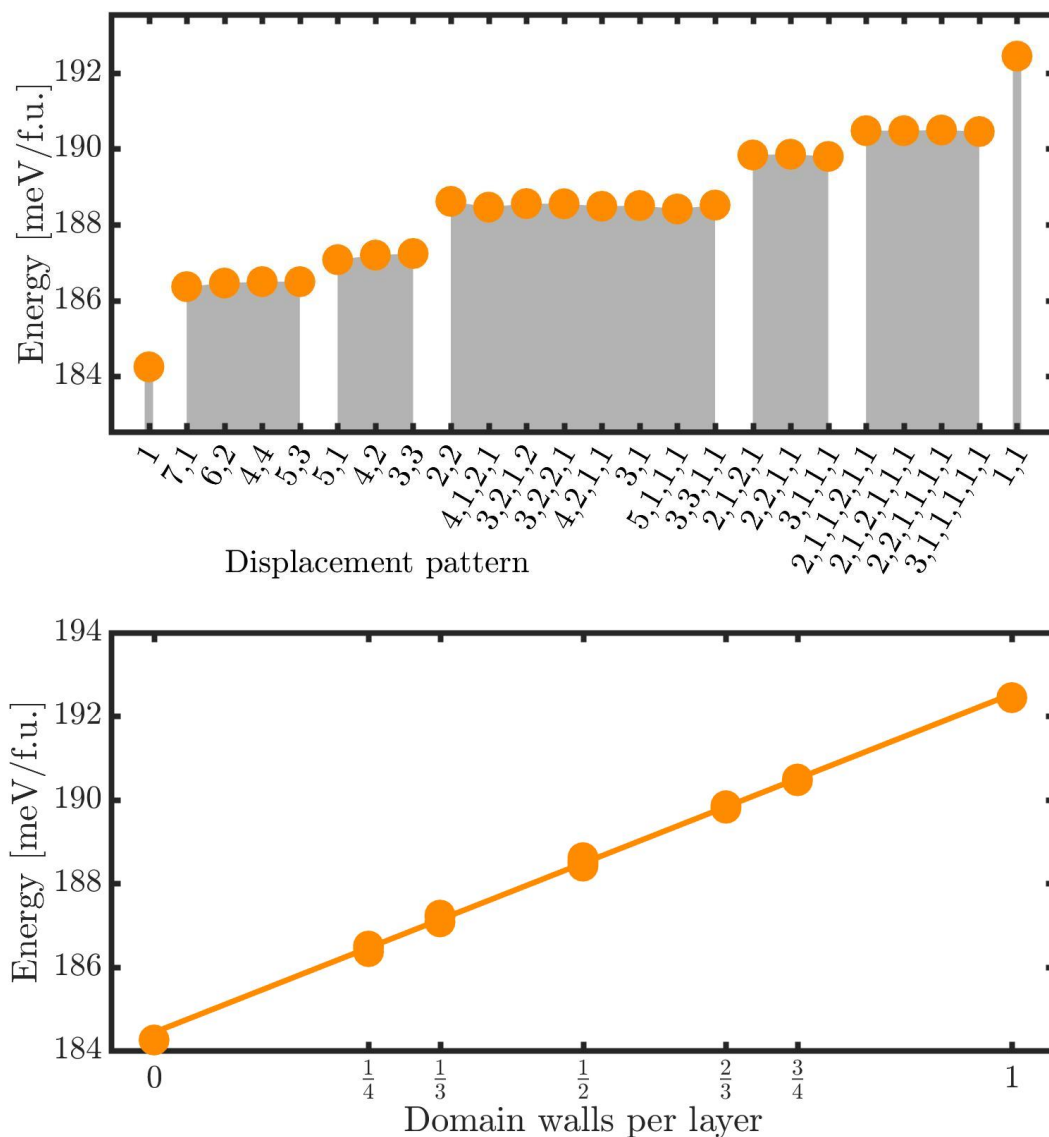


Figure 5.14: The energies of structures with Pb/Zr/O displacing in various displacement patterns. Shaded regions in the upper plot highlight displacement patterns with effectively degenerate energies. The shaded regions each have a distinct number of domain walls per layer. The number of domain walls per layer is linearly related to the energy, as shown in the lower plot.

There is no reason that the energies of these structures must exhibit a linear relationship between the number of domain walls per layer and energy, but in each case the relationship is approximately linear. The energy cost per domain wall decreases as A changes from Ba to Sr to Pb to Ca to Mg. This trend means domain walls become more favorable for smaller A site cations, consistent with tolerance factor arguments that predict nonpolar structures to be preferable for smaller A site cations.

The trend in slope suggests a possible defining feature of antiferroelectricity. Of the materials considered, antiferroelectricity is only observed in PbZrO_3 in which the energy cost per domain wall is small but slightly positive. Among other things, this means PbZrO_3 has a nonpolar ground state structure and a polar structure slightly higher in energy. Finding other materials which have a similarly small and positive energy cost per domain wall may lead to other antiferroelectrics. Since the energy cost per domain wall seems to follow what is expected from basic tolerance factor arguments, tuning the energy cost to roughly zero should be possible. Ensuring that these structures are accessible experimentally will likely prove challenging as these structures are generally not the ground state in $A\text{ZrO}_3$. The energies of the structures considered in $A\text{ZrO}_3$ are not always stable and can even raise the energy relative to $\text{Pm}\bar{3}\text{m}$. While this does not provide a simple path towards designing new antiferroelectrics, future work along this line of thinking is warranted.

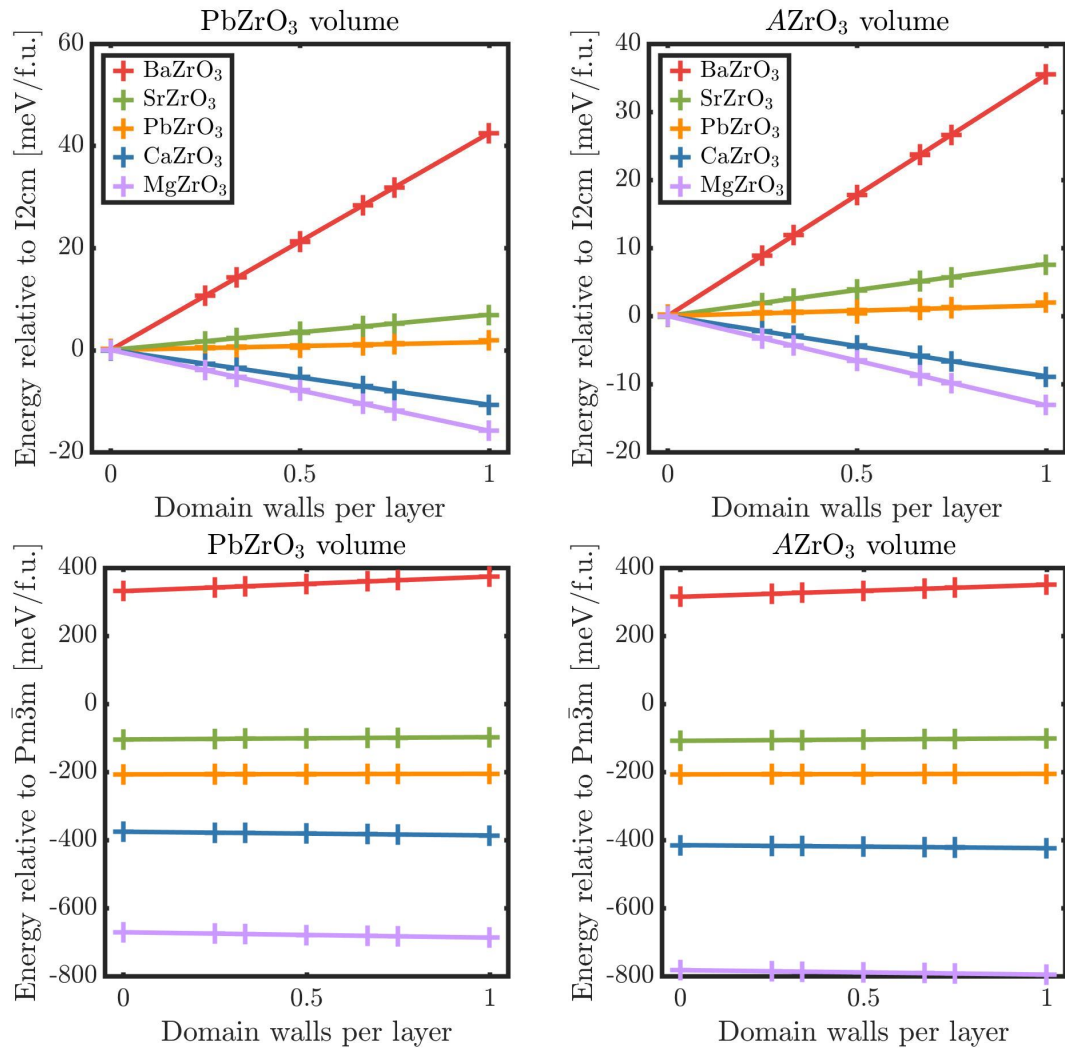


Figure 5.15: The energies of $AZrO_3$ in two kinds of unit cells. Energies are given with respect to both $I2cm$ and $Pm\bar{3}m$. Best fit lines are included for the 24 displacement patterns considered in each case.

5.8.5 Possible implications of structural model

Based on the structural model, there is an infinite set of low energy structures in PbZrO_3 . Preliminary calculations have revealed this flat energy landscape seems to be a special feature of the energy landscape in PbZrO_3 that is not present in other non antiferroelectric perovskite materials. This suggests a flat energy landscape may be a signature of antiferroelectricity but more work is needed to study this possibility. If found to be a defining feature of antiferroelectricity it would open the door to designing new antiferroelectric materials by forcing a material to have this kind of energy landscape, potentially through chemical substitution or hydrostatic pressure.

CI-NEB calculations were performed for transition paths between several of the structures with alternate displacement patterns which could potentially be relevant for switching from Pbam to I2cm or R3c . These paths are similar to the indirect paths considered in Figure 5.10, but with more planes of Pb cations involved. The energy barrier was found to always be lower when reversing a single plane of displacements at a time, but the electric field to overcome these barriers does not significantly change. These calculations in larger unit cells show that there is nothing special about that migration barriers we calculated in the primitive 40 atom unit cell. The actual transition path may proceed by reversing the displacements of individual planes of Pb cations over arbitrarily short or long length scales.

The existence of these low energy structures within DFT suggests that these structures may exist in experimental samples of PbZrO_3 . Indeed, the lowest energy structure found has the 2,1,2,1 displacement pattern - not Pbam - which has been observed as a domain boundary [85]. This displacement pattern appears to

be stabilized within these calculations over the experimental Pbam ground state due to an underestimation of the volume which is known to occur when using PBEsol. An unsolved pressure induced phase in PbZrO₃ [81, 82] is thought to be orthorhombic and polar [81] which is consistent with the I2cm symmetry of the 2,1,2,1 displacement pattern. Calculating an average modulation wave vector for the 2,1,2,1 displacement pattern (which mixes Σ_2 at the $k = [\frac{1}{3}\frac{1}{3}0]$ point and Γ_4^-) gives $[110] \times 0.281$ - very close to the wave vector which generates the incommensurate and "non-cubic non-modulated" phases observed under pressure [88]. A random mixture of these displacement patterns could appear as incommensurate phase, which have been seen observed in pure PbZrO₃ [78, 88] and many PbZrO₃ based materials [107, 108, 84, 109]. These incommensurate phases have been attributed to commensurate stripes of varying lengths [84] being stabilized by various dopants. These results show that while such structures are very low in energy in pure PbZrO₃, there are many other low energy structures that are not simply stripes of nearly the same length (such as 4,1,2,1).

5.9 Summary

The effects of applying an electric field to the Pbam ground state of PbZrO₃ were considered using first principles calculations. The R3c structure was found to be low in energy and should be accessible using an electric field, as expected based on previous experimental and theoretical work. The I2cm structure also has low energy and may be reachable using an electric field aligned with its [110] polarization. Direct transition paths from Pbam to I2cm or R3c were found to be essentially identical, with the transition from Pbam to R3c passing through I2cm. This happens because the polarization and octahedral rotation axes prefer

to remain aligned with [110] until a significant [110] polarization is developed, as happens in the I2cm structure. The I2cm structure itself is unstable towards a rotation of the polarization and octahedral rotation axes from [110] towards [111] and allowing this degree of freedom to relax into the structure leads to R3c. The previously unclear structural relationship between Pbam and R3c can be simply interpreted as an alignment of the [110] displacements in Pbam, resulting in I2cm which is unstable to R3c.

Calculations of indirect transition paths in which each plane of Pb cation displacements reverses independently revealed no particular preference for the indirect path over the direct path where all Pb displacements reverse simultaneously. These indirect paths are still relevant to switching processes as they can be viewed as simple representations of the creation and motion of domain boundaries that are known to exist in real samples. The energy barriers along the indirect and direct transition paths can be overcome with approximately the same electric field, suggesting that the reversal of Pb displacements in a real sample can occur over arbitrary length scales and should be relatively insensitive to defects.

It was also demonstrated that there are many low energy structures in PbZrO_3 corresponding to different displacement patterns of the Pb cations along [110]. The low energy structures we found may have been seen in previous experimental work but have not been recognized. Future work on PbZrO_3 and related materials should consider the existence of these structures which may help interpret results. This kind of flat energy landscape may be a characteristic feature of antiferroelectrics. If so, any material with a nonpolar ground state that can be viewed as a stacking of polar regions that also has a low en-

ergy cost per domain wall should have an overall energy landscape similar to PbZrO_3 and is therefore a candidate antiferroelectric.

CHAPTER 6
COMPUTATIONAL STUDIES OF Ln_2NiO_4

6.1 Motivation

The $Ln_2NiO_{4+\delta}$ series of materials has been studied for possible use in solid oxide fuel cells (SOFC), where Ln is a lanthanide cation (La, Pr, Nd, etc.). In particular, this class of materials may be used as a cathode in a SOFC which must serve several purposes. It must be able to split gaseous O_2 molecules at its surface, absorb the oxygen ions, and transport the oxygen ions through it. The cathode must also be able to conduct electrons. $Ln_2NiO_{4+\delta}$ naturally absorbs oxygen ions when placed in an oxygen rich environment and is known to be metallic [110, 111]. The value of δ can be greater than 0.25 [112]. These materials also allow oxygen ions to diffuse through them and are therefore good candidates for use as a cathode in a SOFC.

One of the limiting factors for using $Ln_2NiO_{4+\delta}$ as a cathode in a SOFC is the relatively high temperature required for ionic transport - around 700 K for $Ln=La$ [113]. Operating a SOFC device at this temperature introduces numerous problems including degradation of the device over time and increased operating costs to maintain the high temperature. High temperature is required for operating most known SOFC cathodes and there is an active search for a cathode that can operate at lower temperatures [111].

The operating temperature for a cathode in a SOFC is usually determined by the limiting activation energy for oxygen ion migration (which may be the activation energy for ionic transport through the cathode or reduction of oxygen

at the surface of the cathode). The diffusion rate will vary as $\exp(-E_a/k_B T)$ with E_a being the activation energy, k_B being the Boltzmann constant and T being temperature. Reducing E_a thus reduces the temperature required for the device to operate. The initial focus of this study was to understand what controls the activation energy of ionic migration in $Ln_2NiO_{4+\delta}$ so that it might be reduced. Ln was restricted to La, Pr, and Nd which should be sufficient to study trends in the Ln series with minimal computational cost.

6.2 Previous work on Ln_2NiO_4

La_2NiO_4 forms in one of several space groups as a function of temperature: $I4/mmm$ for $800\text{ K} < T$, $Cmca$ for $80\text{ K} < T < 800\text{ K}$, and $P4_2/nm$ for $T < 80\text{ K}$ [114], each of which is an $n=1$ Ruddlesden-Popper structure. These space group labels will be used to identify the specific crystal structure, for instance the $I4/mmm$ structure. Each of the structures is shown in Figure 6.1. The $Cmca$ and $P4_2/nm$ structures can both be viewed as distorted forms of the high symmetry $I4/mmm$ structure. Both low temperature structures are reached by adding an X_3^+ distortion to the $I4/mmm$ structure. $Cmca$ allows $X_3^+(a0)$ and $P4_2/nm$ allows $X_3^+(aa)$. The $P4_2/nm$ structure may actually be an average structure over local regions of the structure which have $Pccn$ symmetry on a local scale (which allows $X_3^+(ab)$ distortions) [114]. The X_3^+ irrep allows several forms of antiphase octahedral rotations about the a and b (in plane) axes. Using Glazer notation, $Cmca$ and $P4_2/nm$ allow $a^-a^-c^0$ and $a^-b^0c^0$ rotations in each perovskite layer respectively. In a modified Glazer notation that specifies the phase of the rotations between adjacent perovskite layers, these are $\Phi\Phi0/\Phi\Phi0$ and $0\Phi0/\Phi00$ [115].

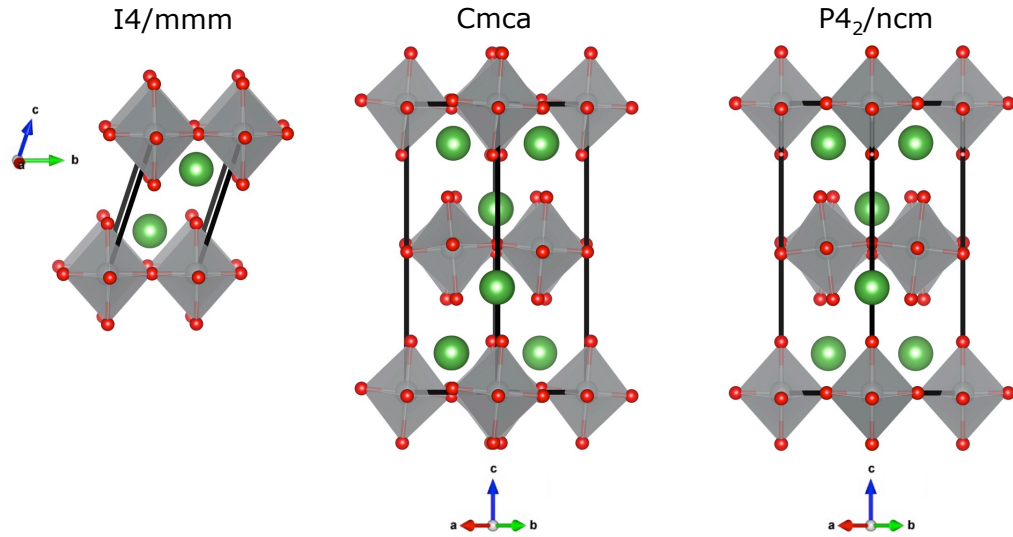


Figure 6.1: The crystal structure of La_2NiO_4 . Green, gray and red spheres represent La, Ni and oxygen respectively. NiO_6 octahedra are shown as a shaded gray region.

The structure of Pr_2NiO_4 and Nd_2NiO_4 varies with temperature similarly to La_2NiO_4 except the $I4/mmm$ structure has not been observed at high temperature [116, 117, 118]. A transition into $I4/mmm$ above 1500 K and 1896 K has been predicted by extrapolation for Pr_2NiO_4 and Nd_2NiO_4 [116, 118] but never observed because these materials melt before reaching such high temperatures. The transition between $P4_2/ncm$ and $Cmca$ occurs at 115 K and 130 K for Pr_2NiO_4 and Nd_2NiO_4 .

The Ln cation prefers to have a formal valence of 3+ and the oxygen anions prefer a formal valence of 2-, leaving the Ni cation with a valence of 2+ in $Ln_2\text{NiO}_4$. The Ni^{2+} cation therefore has an electron configuration of $3d^8$. The La, Pr and Nd variants exhibit an antiferromagnetic ordering of the $3d^8$ electrons on the Ni cations below 330 K, 325 K, and 320 K respectively [114, 116, 118]. The spins order antiferromagnetically within each plane of Ni cations, as shown in

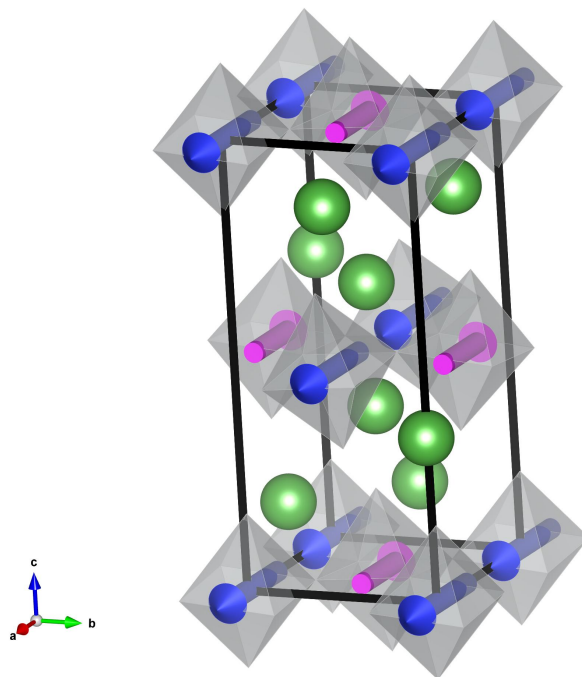


Figure 6.2: The magnetic ordering of spins on the Ni ions in Ln_2NiO_4 . Green spheres represent La and the shaded gray regions are NiO_6 octahedron. Spins in opposite directions are shown as blue and purple arrows centered on each Ni ion. The crystal structure is identical to the $P4_2/nm$ structure shown in Figure 6.1.

Figure 6.2. An additional ordering of the 4f electrons on Pr and Nd is also observed at very low temperatures. The spin ordering of the 4f electrons is somewhat more complicated, having noncollinear spins, but is mostly antiferromagnetic [116, 118].

6.3 Previous work on $\text{Ln}_2\text{NiO}_{4+\delta}$

Ln_2NiO_4 is known to absorb oxygen from air at high temperature, leading to $\text{Ln}_2\text{NiO}_{4+\delta}$ [119]. The amount of excess oxygen can be significant, with δ be-

ing 0.25 [120, 121, 122] or even slightly higher [112]. Excess oxygen can be removed from the structure by heating a sample under vacuum [123]. When $\delta = 0$ these materials are charge transfer insulators [124] but as δ is increased holes are added into the electronic structure and these materials become metallic [114].

The addition of excess oxygen to the crystal structure significantly complicates the crystal structure. Several phase diagrams have been reported as a function of δ and temperature. In some cases the phase diagram consists of the same structures as the stoichiometric material, though the lattice parameters and transition temperature between phases changes with δ [125, 126, 127]. More complicated phase diagrams have been reported in which the excess oxygen forms staged (meaning the excess oxygen is only present in every n^{th} rock salt layer) or 3D ordered phases [128, 129]. In both cases excess oxygen was found to suppress the octahedral rotations in the $P4_2/nm$ or $Cmca$ structures - either by reducing their amplitude [130] or reducing the transition temperature out of $I4/mmm$ [129].

Numerous studies have been performed to determine the structure of $Ln_2NiO_{4+\delta}$, and in many cases some ordering of the excess oxygen atoms was observed [112, 120, 121, 122, 130, 131, 132, 133, 134, 135, 136, 137]. This ordering can lead to an ordering of holes and spins [136] and can form stripes [137]. The electron beam in a transmission electron microscope was seen to alter the ordering pattern [133]. Both commensurate and incommensurate modulations have been observed [112]. The specific ordering can vary, even for the same value of δ , suggesting that several ordering patterns can be locally stable under any particular set of conditions [122]. The excess oxygen can also be completely disordered; an order-disorder transition was observed in the Pr variant at 720

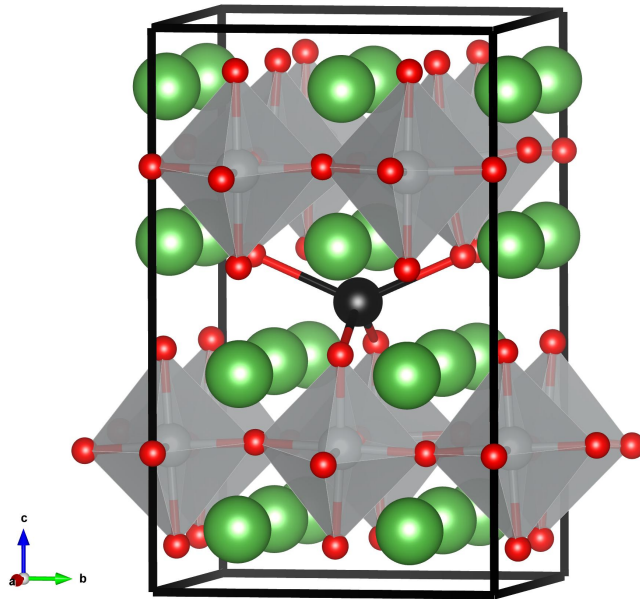


Figure 6.3: Example crystal structure with a single excess oxygen atom in the unit cell. Green, gray, red, and black spheres represent Ln , Ni, oxygen, and the excess oxygen. Shaded gray regions are NiO_6 octahedra. The excess oxygen atom is tetrahedrally coordinated by Ln ions. The excess oxygen atom also repels the four oxygen atoms closest to it, shown as bonds here, due to the Coulomb interaction.

K [130, 135]. Phase separation has also been observed, in which a sample with overall $\delta = 0.07$ separated into regions with smaller and larger δ [125].

While the exact arrangement of excess oxygen atoms is not known, neutron diffraction has shown that the excess oxygen is located in the rock salt layer [138, 139]. The excess oxygen atom is tetrahedrally coordinated by 4 nearest neighboring oxygen atoms as well as 4 nearest neighbor Ln cations. A diagram of this location is shown in Figure 6.3.

Nuclear density measurements made using neutron powder diffraction have

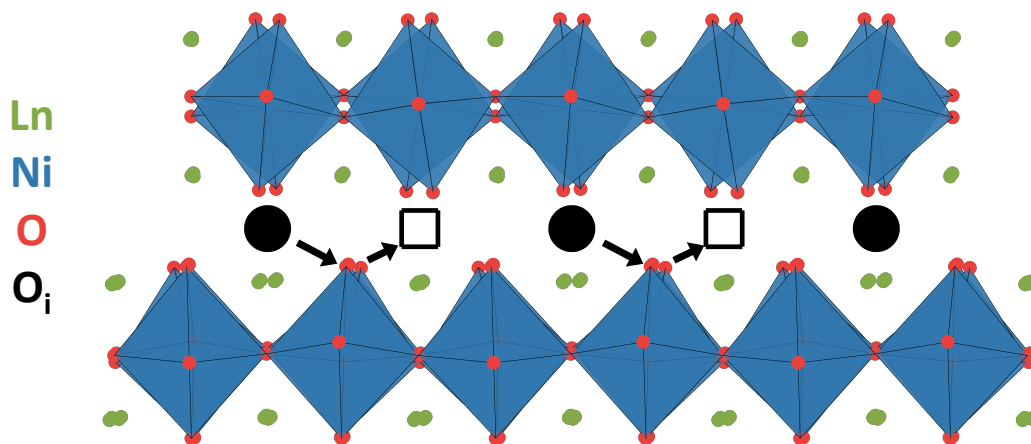


Figure 6.4: Schematic of interstitialcy mechanism. Green, red, and black spheres represent Ln , oxygen, and the interstitial oxygen. Shaded blue regions are NiO_6 octahedra. Unoccupied interstitial sites are shown as empty squares. The interstitial oxygen takes the place of another oxygen, which simultaneously moves to an unoccupied adjacent interstitial site as indicated by arrows.

shown a continuous distribution of oxygen atoms between the interstitial site shown in Figure 6.3 and the four nearest neighbor oxygen atoms [140]. This suggests the excess oxygen atoms move around the crystal structure by exchanging positions with other oxygen atoms. This interstitialcy mechanism is also seen using molecular dynamics simulations [141, 142], neutron scattering to observe highly anisotropic displacements of the oxygen atoms [143, 144, 145], and nuclear magnetic resonance spectroscopy [146]. A schematic showing this interstitialcy mechanism is given in Figure 6.4.

The activation energy for oxygen ion migration in $La_2NiO_{4+\delta}$ has been measured as 0.85 eV [147] or 0.59 eV [146] in ceramics, 0.88 eV in a single crystal [148], 0.19 eV in a thin film [149], and 0.54 eV in a polycrystalline sample [113]. These measurements can be performed using isotopic $^{16}O/^{18}O$ exchange and

secondary ion mass spectroscopy [148]. Molecular dynamics has predicted an activation energy of 0.51 eV [141]. Density functional theory predicted a migration barrier of 1.06 eV [150]. There is currently no clear explanation for why there is such a large range of experimental activation energies. It is possible that different arrangements of excess oxygen, which are known to occur and are highly sensitive to experimental conditions, lead to very different activation energies.

Past theoretical work has shown that the energy barrier for oxygen ion migration in $Ln_2NiO_{4+\delta}$ is strongly correlated with the tendency for Ln_2NiO_4 or $LnNiO_3$ to be distorted by octahedral rotations [150]. This correlation suggests the octahedral rotations are involved in ionic transport but does not explain how. The migration path of oxygen ions breaks and reforms Ni-O bonds in the material so it was suggested that electronic structure, particularly of the Ni cations, may also be involved in ionic transport [150]. The presence of oxygen interstitials has been related to local rocking of NiO_6 octahedron using nuclear magnetic resonance spectroscopy [146]. Two important questions remain open about these materials: whether ionic migration is limited by some ordering of the excess oxygen ions and if high concentrations of excess oxygen can lead to a stiffening of the lattice and its octahedral rotation distortions, thereby causing an increase in the migration barrier [111, 151]. This study begins with these ideas and questions in mind. Particular focus will be given to the arrangement of excess oxygen in $Ln_2NiO_{4+\delta}$ and how it can be simulated using periodic boundary conditions.

6.4 Simulating excess oxygen

Defects in a crystal structure can be simulated using periodic boundary conditions by using a large unit cell to minimize the interaction of a defect with its periodic images. The interaction of a defect with its periodic images is determined by the choice of unit cell. In cases where defects are not expected to interact significantly, the unit cell can be chosen to be very large to minimize these interactions. In the case of $Ln_2NiO_{4+\delta}$, however, δ can be so large that these effects are unavoidable. When $\delta=0.25$, there is one excess oxygen atom in every 4 unit cells of Ln_2NiO_4 . With this much excess oxygen in the crystal structure the shortest distance between an excess oxygen atom and its images in *any* supercell will be at most a single unit cell of Ln_2NiO_4 . Given the high density of excess oxygen and the experimental observation that the excess oxygen atoms can arrange in an ordered pattern, attempting to treat the excess oxygen atoms as noninteracting defects would be incorrect - the excess oxygen should be treated as part of the crystal structure.

A completely disordered arrangement of excess oxygen atoms could be efficiently represented using supercells and special quasirandom structures [152]. An arbitrary ordered arrangement of excess oxygen atoms could be represented using a supercell corresponding to the particular ordering pattern. If the arrangement followed some set of rules - perhaps the excess oxygen atoms must be more than 3 Å apart - the number of possible arrangements could be significantly reduced and would be said to be have a correlated disorder. Since the specific arrangement of excess oxygen atoms depends on numerous factors experimentally, it is likely the arrangement of excess oxygen is partially ordered and may follow a correlated pattern. A systematic approach is therefore needed

to simulate various possible excess oxygen arrangements.

Regardless of the actual arrangement, a supercell based approach is needed to study the crystal structure. Methods have been developed for this purpose [153, 154, 155] but have mainly been used to study metallic alloys or semiconductors [156]. In these relatively simple systems, the Coulomb energy of given arrangement of atoms can be used to determine if the arrangement is reasonable and worth considering [156] with more accurate methods, such as density functional theory. These supercell methods have not been widely used to study complex oxides, such as $Ln_2NiO_{4+\delta}$, which are generally larger and more complicated, making them more computationally demanding to study than alloys. This work addresses how the supercell approach can be used to study $Ln_2NiO_{4+\delta}$.

6.4.1 Generating arrangements of excess oxygen

Excess oxygen atoms are located within the rock salt layers, based on neutron diffraction experiments [138, 139]. Within the primitive unit cell of the high symmetry $I4/mmm$ structure there are two equivalent sites that the excess oxygen atoms could occupy, as shown in Figure 6.5. These two sites are periodic with the $I4/mmm$ lattice so an arbitrary fully ordered arrangement of excess oxygen atoms can be represented within a supercell of the primitive $I4/mmm$ unit cell.

By representing excess oxygen in a supercell the lattice vectors will, by definition, determine the periodicity of arrangement of oxygen atoms. By placing multiple oxygen atoms in relative proximity within the same supercell, periodic

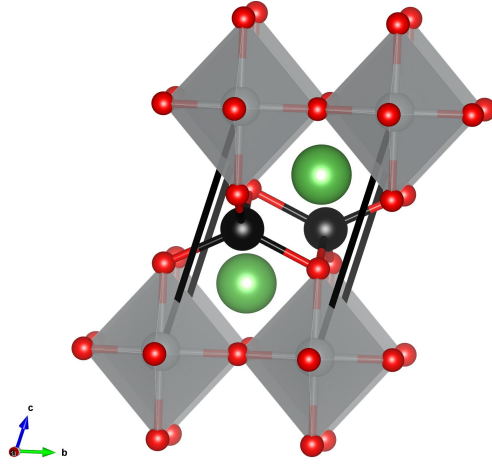


Figure 6.5: The primitive unit cell for an $I4/mmm$ $n=1$ Ruddlesden-Popper structure. Green, gray, red, and black spheres represent La, Ni, oxygen, and the two possible sites for excess oxygen in this unit cell respectively. NiO_6 octahedra are shown as a shaded gray region.

clusters of excess oxygen may be simulated. In order to represent an arbitrary periodic arrangement of excess oxygen, an arbitrary supercell can be defined using an integer matrix \mathbf{S} and lattice vectors for a primitive unit cell

$$\begin{pmatrix} a_{s,1} & a_{s,2} & a_{s,3} \\ b_{s,1} & b_{s,2} & b_{s,3} \\ c_{s,1} & c_{s,2} & c_{s,3} \end{pmatrix} = \begin{pmatrix} S_{11} & S_{12} & S_{13} \\ S_{21} & S_{22} & S_{23} \\ S_{31} & S_{32} & S_{33} \end{pmatrix} \begin{pmatrix} a_{p,1} & a_{p,2} & a_{p,3} \\ b_{p,1} & b_{p,2} & b_{p,3} \\ c_{p,1} & c_{p,2} & c_{p,3} \end{pmatrix} \quad (6.1)$$

where \vec{a} , \vec{b} , \vec{c} are the lattice vectors of the primitive or supercell as indicated by subscripts [157, 158]. For any given \mathbf{S} , the resulting lattice vectors do not uniquely represent the corresponding lattice; there are infinitely many repre-

sentations of the same lattice. \mathbf{S} may be translated into Hermite normal form

$$\begin{pmatrix} S_{11} & S_{12} & S_{13} \\ 0 & S_{22} & S_{23} \\ 0 & 0 & S_{33} \end{pmatrix} \quad (6.2)$$

where $0 < S_{ii}$, $0 \leq S_{1,2} < S_{2,2}$, and $0 \leq S_{1,3}, S_{2,3} < S_{3,3}$. The Hermite normal form gives a standard form for any lattice [158].

The determinant of \mathbf{S} determines how many primitive unit cells are in the supercell. By placing N excess oxygen atoms in a supercell, the concentration of excess oxygen becomes $\delta = N/|\mathbf{S}|$. The Hermite normal form for representing \mathbf{S} provides a route to generate arbitrarily shaped supercells for a given δ and N . The determinant of \mathbf{S} is the product of its diagonal elements and must be equal to N/δ . There is a finite number of diagonal elements that are easily enumerated which produce a given determinant. For any set of diagonal elements, the off diagonal elements can be enumerated using the definition of the Hermite normal form. Thus for a fixed N/δ there is a finite number of supercells which can be used to represent an ordered arrangement of excess oxygen atoms.

The supercells produced by this process can be very irregular, with the lengths of the lattice vectors varying widely and/or angles between the lattice vectors being far from 90° (the same is true for the resulting reciprocal lattice). This can cause practical problems in the implementation of DFT. For instance, a denser integration grid may be needed to adequately sample reciprocal space when the reciprocal lattice vectors are irregular. The Lenstra-Lenstra-Lovász basis reduction algorithm [159] was used to mitigate this issue. This algorithm takes a set of lattice vectors and translates them into a set of vectors that are as short and close to orthogonal as possible without changing the lattice.

For a given supercell defined by S there are multiple possible arrangements of the excess oxygen atoms. Within the Ruddlesden-Popper structure, there are $2|S|$ positions for excess oxygen. There are $(2|S|)!/(2|S| - N)!$ possible ways to place N atoms on these positions. This number can be reduced by symmetry - translational symmetry alone reduces it by a factor of $2|S|$. Regardless of symmetry, the number of possible arrangements grows rapidly with N .

Initially, clusters of excess oxygen (that is, $N > 1$) will be ignored in favor of placing a single excess oxygen atom in a supercell. This assumption not only reduces the number of structures to consider, it also reduces the size of supercells which need to be considered, significantly lowering the computational burden.

6.4.2 Choice of stoichiometric structure

After generating an arrangement of excess oxygen atoms the stoichiometric part of the structure must be added to the supercell. As a starting point, this could be taken to be any of the structures observed in Ln_2NiO_4 : $I4/mmm$, $Cmca$, or $P4_2/nm$. All of the interstitial positions are equivalent in the $I4/mmm$ and $Cmca$ structures, as shown in Figure 6.5 and Figure 6.6. The $P4_2/nm$ structure, however, has two inequivalent interstitial positions as seen in Figure 6.6. This means that there can be two symmetrically distinct ways to combine $P4_2/nm$ with an arrangement of interstitial oxygen atoms.

Combining the $Cmca$ or $P4_2/nm$ structure with an arbitrary arrangement of excess oxygen atoms often requires the use of a larger unit cell than when the $I4/mmm$ structure is used because not all supercells of $I4/mmm$ are not commensurate with these structures. When needed, supercells were constructed to

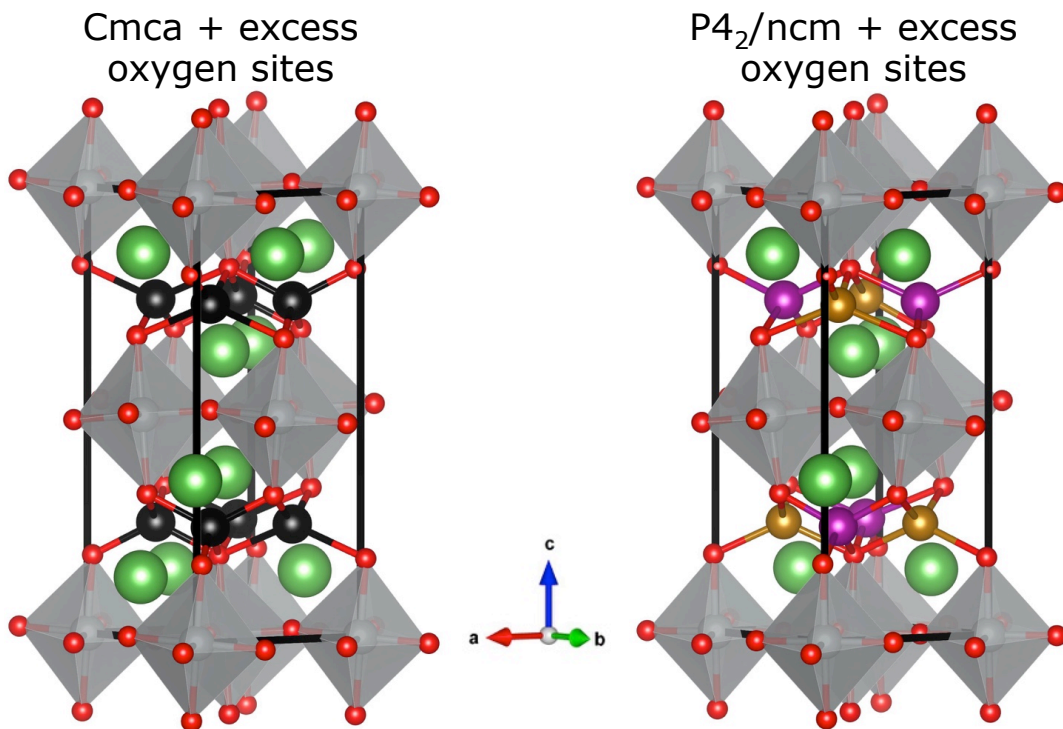


Figure 6.6: The primitive unit cell for the $Cmca$ and $P4_2/nm$ structures with possible interstitial sites shown. Green, gray, and red spheres represent La, Ni, oxygen. NiO_6 octahedra are shown as a shaded gray region. The possible excess oxygen sites are shown in black for $Cmca$ and gold/purple for $P4_2/nm$. In $Cmca$ these sites are equivalent but in $P4_2/nm$ these sites have two slightly different environments, and are differentiated here by color.

be commensurate with either $Cmca$ or $P4_2/nm$ and a particular arrangement of excess oxygen atoms. This was done by searching for a supercell specified by S' that is a supercell of both the excess oxygen atoms and $Cmca$ or $P4_2/nm$. This search can be done by enumerating supercells of increasing size, as before, of the $Cmca$ or $P4_2/nm$ structure until an adequate supercell is found.

The $I4/mmm$ structure was usually used as the parent structure to keep the size of supercells to something manageable within density functional theory.

Using the $I4/mmm$ structure is consistent with the high temperature phase of $\text{La}_2\text{NiO}_{4+\delta}$, which seems reasonable as the devices of interest operate at high temperature. Further, relaxed structures were checked for instabilities within density functional theory so any structures that would have been found while using Cmca or $\text{P4}_2/\text{ncm}$ as the parent structure will still be found, provided the unit cell is commensurate with the X point of $I4/mmm$. Due to the cheap computational cost of classical potentials, described in Section 6.10, each of the three structures was used as a parent structure for calculations.

6.5 Parameters of density functional theory calculations

The PBEsol exchange-correlation functional was used throughout. The pseudopotentials included valence electrons as follows: $5s^25p^65d^16s^2$ for La; $3p^63d^84s^2$ for Ni; and $2s^22p^4$ for O. The pseudopotentials for Pr and Nd were constructed to freeze some of the 4f electrons into the core under the assumption that the cation has a formal valence of 3+. In both cases this leaves 11 valence electrons. These pseudopotentials were used in order to avoid complications that can arise due to the electronic structure of 4f orbitals. These orbitals are not expected to have a significant effect on the properties of interest here, especially because the operating temperature is far above the magnetic ordering temperature of the 4f electrons.

Calculations were spin-polarized and assumed ferromagnetic ordering of spins on the Ni sites. The actual spin ordering is antiferromagnetic in the stoichiometric material [114, 116, 118] but differs in $\text{Ln}_2\text{NiO}_{4+\delta}$. In $\text{La}_2\text{NiO}_{4.17}$ the spins follow a striped ordering at temperatures below 20 K [137]. At the operat-

ing temperature of the devices of interest, these spins are not ordered. However, spin-polarization is known to cause important changes to properties such as the lattice constants, and some spin ordering must be used once spin-polarization is allowed. Ferromagnetic ordering is the simplest ordering to use and has been used with success previously in similar materials [160, 161]. Further, attempting to accurately solve for the magnetic structure in each of the crystal structures considered would require large supercells in many cases, and therefore be computationally infeasible.

A Hubbard U of 4.0 eV was applied to the Ni 3d electrons. Smaller values of U incorrectly make the stoichiometric Ln_2NiO_4 metallic. A Hubbard U of 5.4 eV was applied to the La 4f electrons, following the value determined by Scheffler for Ln_2O_3 [162]. This value was determined to make LDA+U better match with much more accurate GW calculations. Without including this +U on the La 4f orbitals, these unoccupied orbitals lie just above the Fermi energy. This is almost certainly wrong - these orbitals are much higher in energy in other lanthanum oxides, such as La_2CuO_4 and $LaCuO_3$ [163]. Similar corrections have been used in Ln_2O_3 [162] and $LaTiO_3$ [164].

A 600 eV plane wave cutoff was used and relaxations were considered converged once the force on each atom reached 1 meV/Å. A $6 \times 6 \times 2$ Monkhorst-Pack mesh was used for unit cells of size approximately $5.5\text{Å} \times 5.5\text{Å} \times 12.4\text{Å}$, which is commensurate with $P4_2/nm$, $Cmca$, and $I4/mmm$. A different mesh was used as necessary for each supercell considered. Due to the number of unit cells considered, convergence tests were done based on the total energy of $I4/mmm$ with a single excess oxygen atom added. The mesh used in each cell was dense enough to converge this total energy to within 5 meV/Ni.

6.6 Is the charge state of excess oxygen O^{2-} ?

Oxygen atoms are sometimes observed in charge states other than O^{2-} . These charged states are not always reproduced by density functional theory without biasing the calculations towards them. To test for such charged states, various permutations of these tests were run: adding a large $+U$ on the excess oxygen, moving some Ni cations towards/away from the excess oxygen atom, and adding a large $+U$ to these nearest Ni. In the cases where a large $+U$ was used, the resulting wave functions were saved and used to start a new calculation without the additional $+U$. This biases the new calculation towards the initial wave functions (instead of starting from random wave functions) and usually results in a solution similar to the calculation with a large $+U$ but with an energy that can be directly compared to other calculations¹.

In all cases tested, the charge state of excess oxygen was O^{2-} . This is consistent with previous results which showed O^{2-} to be more stable than O^- in $La_2NiO_{4+\delta}$ [161].

6.7 Calculation of formation energies

Formation energies were calculated using Equation 6.3 which follows the methodology used in References [161] and [165].

$$E_{\text{formation}} = E_{Ln_2NiO_{4+\delta}} - E_{Ln_2NiO_4} - \delta\mu_O \quad (6.3)$$

This equation simply adjusts for the chemical potential of excess oxygen atoms through the $\delta\mu_O$ term. The energy of the $P4_2/nm$ structure was used for the

¹Calculations with different values of $+U$ result in energies that cannot be compared.

energy of Ln_2NiO_4 . The chemical potential of oxygen was calculated as

$$\mu_O = \frac{1}{2}(E_{O_2} + \Delta h_{O_2}^0) \quad (6.4)$$

where $\Delta h_{O_2}^0$ is a corrective term added to the energy of an O_2 molecule calculated within density functional theory. This term is a simple way to partially correct the binding energy of an O_2 molecule within the GGA [166]. To calculate $\Delta h_{O_2}^0$, an uncorrected formation energy was calculated for several nontransition metal oxides. A linear fit of between experimentally measured formation energies and the calculated formation energies reveals an approximately rigid shift between the calculated and experimental values. $\Delta h_{O_2}^0$ is simply the magnitude of this shift and with the various calculation parameters and pseudopotentials in use here, was calculated as -0.011 eV/ O_2 . With this correction, μ_O was calculated as -4.61 eV/O and is treated as a constant throughout. This value is comparable with the previously calculated -4.38 eV/O [161]. More complicated corrections exist which account for temperature and pressure effects [160] but were not considered here as the primary focus is on trends in the energy rather than absolute values.

6.8 Effect of simulation cell on formation energy

Formation energies were calculated for $\delta=1/8$ and $1/4$ for each Ln . The arrangement of excess oxygen atoms in each case had a single excess atom per unit cell. For $\delta=1/8$, 30 arrangements of excess oxygen atoms were considered while all 12 unique arrangements were considered for $\delta=1/4$. Several $\delta=1/8$ arrangements were omitted because the arrangement was highly artificial and clearly going to result in a high energy. An example of one of these excluded structures

is a $1 \times 1 \times 8$ supercell of the primitive I4/mmm lattice. This places all of the interstitial ions in every 8th rock salt layer, resulting in a high Coulomb energy that cannot be mitigated by lattice distortions.

The arrangement of excess oxygen atoms was combined with the I4/mmm structure and relaxed. The unit cell for each arrangement was constrained to be consistent with the relaxed I4/mmm unit cell to neglect the effect of unit cell relaxation. Unit cell relaxation was considered in several cases and did not qualitatively change these results, as shown in Figure B.1. The stability of each relaxed structure was checked by calculating the Hessian². Any instabilities found were relaxed into the structure. When multiple instabilities were present, each was relaxed in separately and the lowest energy structure was used to calculate the formation energy. The calculated formation energies for these structures are shown in Figure 6.7.

Formation energies for defects are usually positive, but the calculated formation energies are mostly negative. This makes sense as Ln_2NiO_4 naturally absorbs excess oxygen. Previous studies on $La_2NiO_{4+\delta}$ have also found negative formation energies [161].

Clearly there is a large range of possible formation energies for the values of δ considered. While some of the higher energy arrangements could have been expected to be higher in energy based on Coulomb arguments alone, no obvious pattern was found which could predict low energy arrangements. Even ignoring these higher energy arrangements, there is still a significant range of formation energies possible. The difference in formation energy between the

²Structures with only the identity operator for symmetry (space group P1) were not checked for stability because there should not be any distortion which can lower the energy from a saddle point with P1 symmetry.

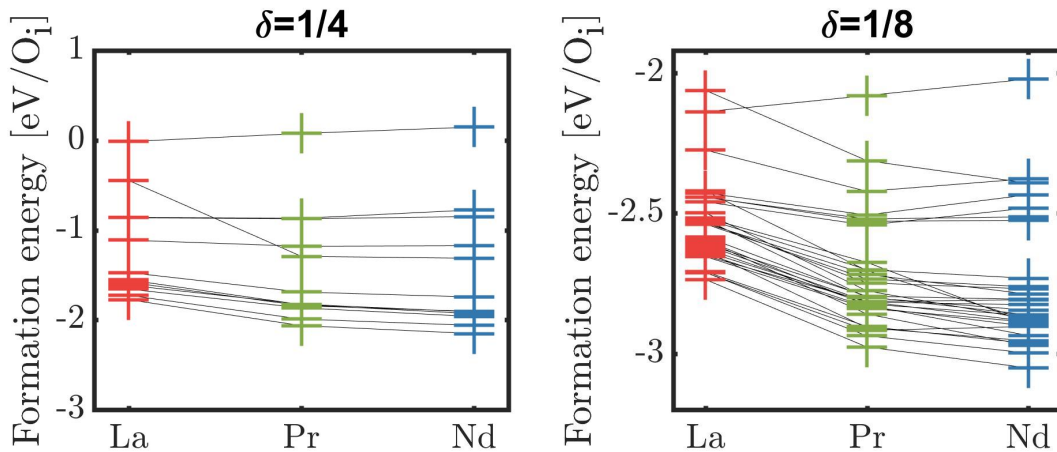


Figure 6.7: Calculated formation energies for $Ln_2NiO_{4.25}$ and $Ln_2NiO_{4.125}$. Energy is given in eV per excess oxygen atom (O_i). Excess oxygen arrangements are connected by a thin black line across the three Ln .

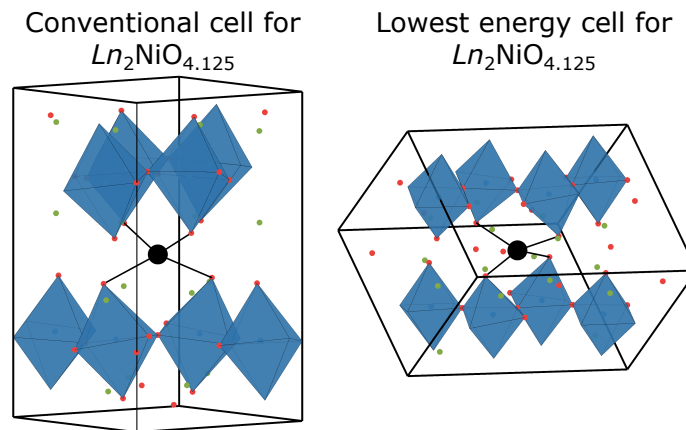


Figure 6.8: Two possible unit cells for $Ln_2NiO_{4.125}$. Green, blue, red, and black spheres represent Ln , Ni, oxygen, and excess oxygen.

lowest energy unit cell and a conventional unit cell (which has been used to study these materials [104, 161]) for $La_2NiO_{4.125}$ is 315 meV/ O_i . Figure 6.8 shows these two unit cells for comparison.

A detailed study of formation energies for $\delta < 1/8$ was only performed for $La_2NiO_{4+\delta}$. This is because both the number of possible structures and the num-

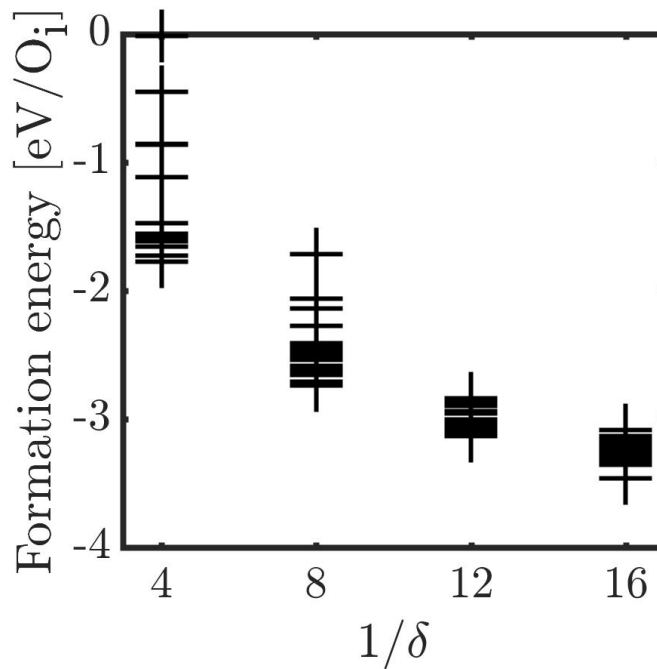


Figure 6.9: Formation energies for $\text{La}_2\text{NiO}_{4+\delta}$.

ber of atoms in a supercell ($1+7/\delta$) grows rapidly as δ decreases. Approximately 30 oxygen arrangements were considered for $\delta = 1/12$ and $1/16$. The resulting formation energies are shown in Figure 6.9.

Two trends are evident in Figure 6.9. First is that the formation energy generally increases as δ increases - this indicates La_2NiO_4 will absorb some oxygen, but unsurprisingly there is a limit to how much is absorbed. Second is that the spread of energies increases with δ , indicating that the exact arrangement of excess oxygen atoms is less important for small δ . This makes sense as the system *must* enter a dilute limit for small enough δ . This trend is also likely in part due to how oxygen arrangements were selected for $\delta = 1/12$ and $1/16$ - these calculations were performed to search for low energy structures. The relaxed structures were chosen by generating every possible arrangement and arbitrarily selecting a subset that did not have very high Coulomb energies.

6.9 Activation energy of ionic migration

The activation energy for oxide ion migration is what ultimately determines the rate of oxygen ion diffusion. The activation energy can be written as a sum of the energy barrier for oxide ion migration and the formation energy.

$$\begin{aligned} E_{\text{activation}} &= E_{\text{migration}} + E_{\text{formation}} \\ &= E_{\text{migration}} + E_{\text{Ln}_2\text{NiO}_{4+\delta}} - E_{\text{Ln}_2\text{NiO}_4} - \delta\mu_{\text{O}} \end{aligned} \quad (6.5)$$

The formation energies for various arrangements of excess oxygen were calculated in Section 6.8. The energetic barrier for oxide ion migration was calculated for many of the excess oxygen arrangements using the climbing image nudged elastic band method (CI-NEB) [51, 52]. This method calculates the energy barrier between two structures, hereafter the initial and final structures. The intermediate structures between the initial and final structures will be referred to as the migration path. The initial and final structures were assumed to be identical by symmetry so that the migration path corresponds to a translation of oxygen through the lattice without changing the crystal structure. More complicated migration paths which change the remainder of the crystal structure, or even the ordering of excess oxygen, are possible but were not considered.

The initial structure is simply one of the relaxed structures. Generating the final structure must be done carefully. The interstitialcy mechanism shown in Figure 6.4 requires the original interstitial oxygen atom to move onto an apical oxygen site while that apical oxygen moves onto an unoccupied interstitial site. If the initial structure were simply translated to create the final structure, the interstitial atom would incorrectly move in a direct line and not exchange with an apical oxygen. The correct exchange of oxygen atoms was accounted

for by swapping the interstitial ion with the correct apical oxygen in the final structure³.

Simply shifting the initial structure to create the final structure is not always correct, even after correctly swapping oxygen atoms. This can be seen by considering the conventional unit cell shown in Figure 6.8. This structure has an octahedral rotation pattern similar to that of $P4_2/nm$ as well as various distortions induced by the excess oxygen (put another way, this arrangement of excess oxygen combined with $I4/mmm$ has an instability). These octahedral rotations (the instability) should not be switched between the initial and final structures. If these distortions were switched it would amount to forcing the octahedral rotations to turn off along the switching pathway (formally this distortion would go from $X_3^+(aa)$ to $X_3^+(00)$ to $X_3^+(\bar{a}\bar{a})$). Similar issues can happen with other arrangements of excess oxygen though the distortions are more complicated in lower symmetry structures. In general there are two kinds of distortions: those due to the excess oxygen and those associated with the stoichiometric Ln_2NiO_4 material. Only the distortions due to the excess oxygen should change significantly along the migration path.

The final structure was created using the following process to avoid switching distortions unnecessarily. First the initial structure was shifted. Symmetry operations corresponding to all combinations of 45° rotations about x , y , and z directions (x and y are oriented 45° between the in plane Ni-O bonds of $I4/mmm$ and z is along the out of plane Ni-O bond) and mirror planes containing the z axis. The position of the interstitial was left unchanged by placing it at the origin prior to applying these operations (any mirror planes contained origin). In

³The correct apical oxygen can be determined by finding the apical oxygen closest to the midpoint between the initial and final interstitial oxygen positions.

many cases this rotated structure does not contain the same lattice points due to a rotation of the lattice - these structures are ignored. The remaining shifted and rotated structures were compared to the initial structure by systematically mapping all ions (except the interstitial ions) onto corresponding ions in the initial structure. The distance between the initial structure and each of the shifted and rotated structures was calculated as a sum of the distance between each ion. The shifted and rotated structure with the lowest distance to the initial structure was used as the final structure. This ensures that the minimum amount of distortions are changed between the initial and final structures.

In many cases the excess oxygen arrangement breaks the tetragonal symmetry of the crystal structure and there are two distinct migration pathways that can be taken. These two pathways correspond to motion of the excess oxygen along two distinct in plane directions that are 90° apart. An example of this is given in Figure 6.10. The opacity of NiO_6 octahedra is determined by how distorted an octahedron, which highlights the localized distortions near each excess oxygen atom. The local environment of the excess oxygen atom is similar along the a and b axes, with each direction having a highly distorted octahedron as the nearest neighbor. However, the environment varies significantly at longer range between these two directions. Moving away from an excess oxygen along the a axis, only the first octahedron is highly distorted. Moving along the b axis, in contrast, the first two octahedra are highly distorted. These distinct migration directions were considered and can result in significantly different energy barriers.

Migration barriers were calculated as a function of δ for $\text{La}_2\text{NiO}_{4+\delta}$. These barriers were calculated on lattices constrained to the lattice parameters of the

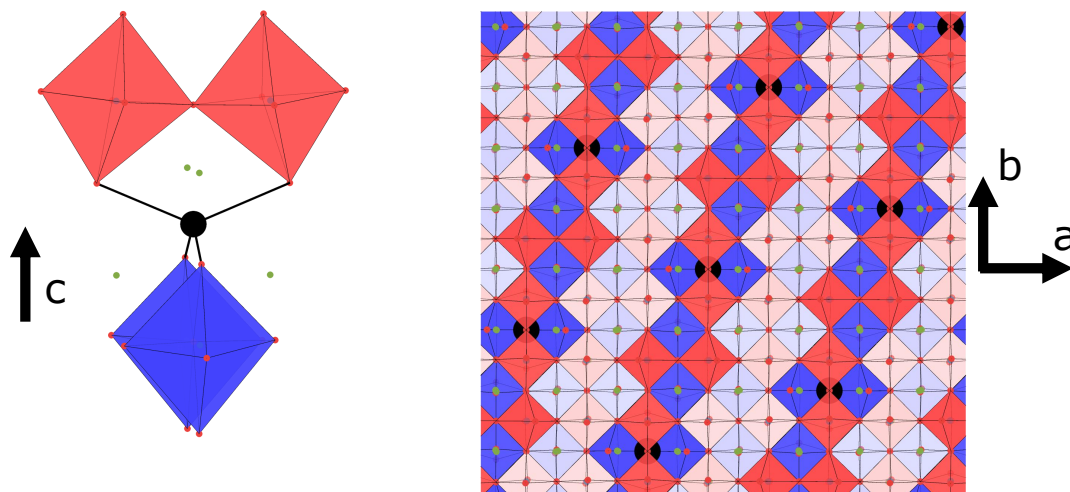


Figure 6.10: The crystal structure in the vicinity of an excess oxygen atom and a large supercell of the lowest energy $\text{La}_2\text{NiO}_{4.125}$ structure shown in Figure 6.8. Green, blue, red, and black spheres represent La, Ni, oxygen, and the excess oxygen. Shaded regions are NiO_6 octahedra; red and blue shading indicate that an octahedron is in the upper or lower layer respectively. The opacity of each octahedron is set by how distorted an octahedron is relative to a uniform octahedron. Only two perovskite layers are shown in the supercell.

relaxed $I4/mmm$ lattice to remove any differences due to unit cell relaxation. Unit cell relaxation was considered in several cases and did not qualitatively change these results, as shown in Figure B.2. Migration barriers for each excess oxygen arrangement considered for $\delta=1/4$ and $1/8$ were calculated. In the larger unit cells with $\delta=1/12$ or $1/16$, only around 10 migration barriers were calculated due to high computational cost. The resulting barriers and activation energies are shown in Figure 6.11.

For higher densities of excess oxygen there is a large range of migration barriers and activation energies, as was seen in the formation energies. As δ decreases the activation energies tend to become closer in energy, suggesting there

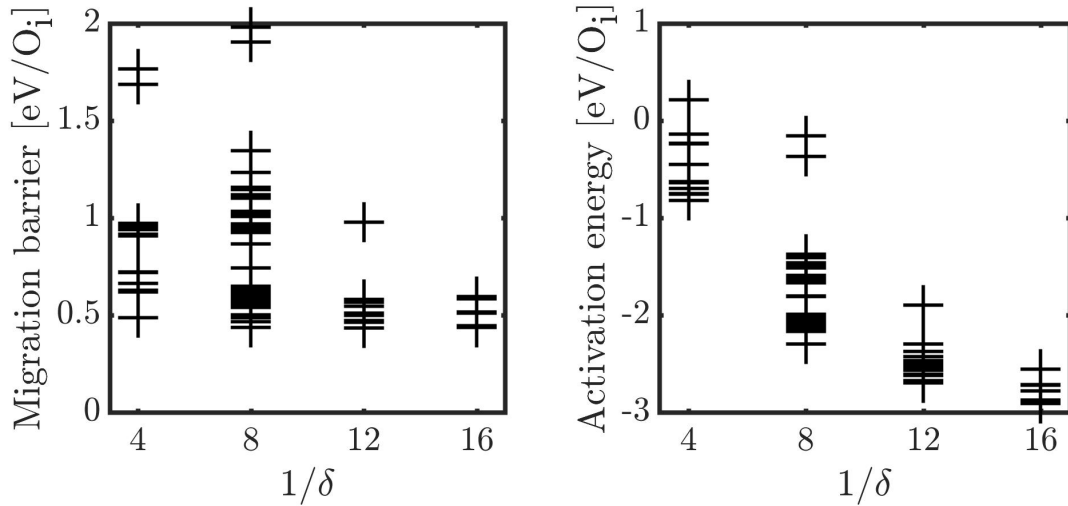


Figure 6.11: Migration barriers and activation energies for $\text{La}_2\text{NiO}_{4+\delta}$.

is a dilute regime when δ is much less than $1/8$. The lowest formation energy structure with $\delta=1/8$, shown in Figures 6.8 and 6.10, allows two distinct migration paths by symmetry. The migration barrier along these two paths are 0.44 and 0.74 eV respectively. In contrast, the migration barrier in the conventional $\delta=1/8$ unit cell is significantly higher at 0.96 eV. The activation energies for these three migration paths are -2.30, -1.99, and -1.46 eV respectively.

Migration barriers were also calculated as a function of Ln for $Ln_2\text{NiO}_{4.125}$. The resulting barriers and activation energies are shown in Figure 6.12. The two points with migration barriers around 2 eV for $Ln=\text{La}$ were not calculated for Pr or Nd. Broadly, the migration barriers tend to decrease as the ionic radius of Ln decreases (La to Nd). Simultaneously, there appears to be a larger spread in the activation energies.

The lines drawn across Ln in Figure 6.12 connect points with the same arrangement of excess oxygen in the initial structure. The two lines differ in the

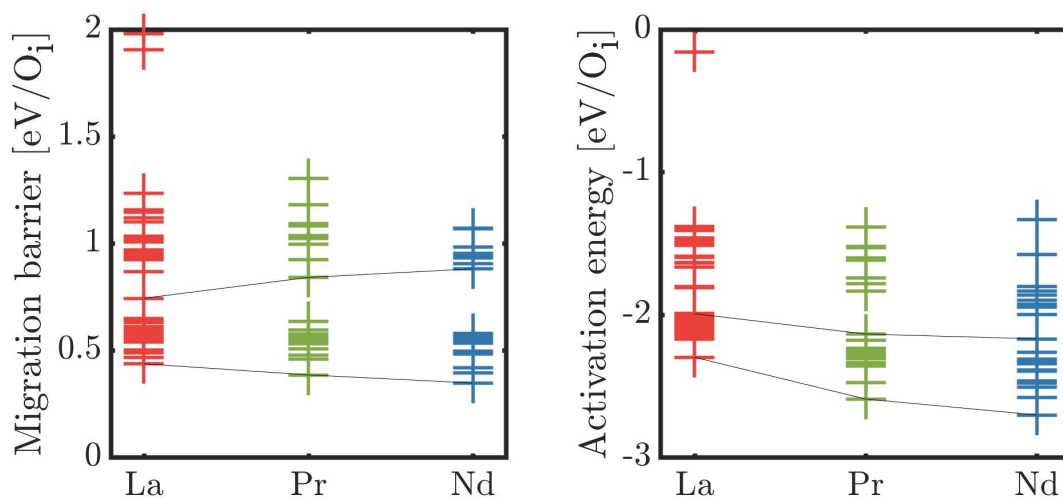


Figure 6.12: Migration barriers and activation energies for $Ln_2NiO_{4.125}$. Black lines connect points corresponding to the lowest energy excess oxygen arrangement. Two such lines are drawn, corresponding to ionic transport along the two symmetrically distinct in plane directions.

direction of oxygen migration; the initial and final structures in the CI-NEB calculations for each line are identical aside from a net shift/rotation of the lattice. This set of migration paths is highlighted for several reasons: the excess oxygen arrangement has the lowest formation energy for each Ln , one of the migration directions yields the lowest energy migration path for each Ln , and the trend in the migration barrier across Ln has opposite sign depending on the direction of oxygen migration. The difference in trends suggests there are multiple factors which control the migration barrier and vary in different ways with Ln . That these opposite trends occur in the same unit cell reemphasizes that great care needs to be taken when simulating $Ln_2NiO_{4+\delta}$.

The frequency of octahedral rotations has previously been shown to be related to the migration barriers [104]. It is well known that open space within

a crystal structure is conducive to ionic transport, so in an attempt to explain the trends in migration barriers the volume of several complex polyhedra centered on the mobile oxygen atoms was calculated. The polyhedra considered included a mixture of cations and oxygen atoms on their vertices. This should account for any mechanism which leads to an excess volume around the mobile oxygen atoms. The main expected sources of excess volume are the octahedral rotations and differences in the unit cell volume across Ln . The polyhedra were determined in the highest energy structure along each migration path, that is the transition state or saddle point structure.

The polyhedron which best explains the trends in migration barriers has the 5 Ln and 8 apical oxygen atoms closest to the two mobile ions on its vertices. An example of this polyhedron and how its volume effects migration barriers is shown in Figure 6.13. Several unit cells define two or more Ln vertices of this polyhedron to be identical due to periodic boundary conditions. This pins these vertices in place and confines the volume of the polyhedron. These unit cells tend to have higher migration barriers but do not follow the same trend as other unit cells and are treated as outliers in Figure 6.13.

The points included in the best fit line in Figure 6.13 can be further subdivided into sets which constrain other sets of vertices to be identical. Doing so leads to several clusters of points. In this way, the migration barriers can usually be explained on a case by case basis but treating each data point as a special case is not a satisfactory way to explain the trends in migration barriers. Further, while a smaller Ln_5O_8 volume for any individual Ln tends to have a higher migration barrier, this volume decreases with the barrier as Ln changes from La to Pr to Nd. Thus a single explanation for the migration barriers in $Ln_2NiO_{4.125}$

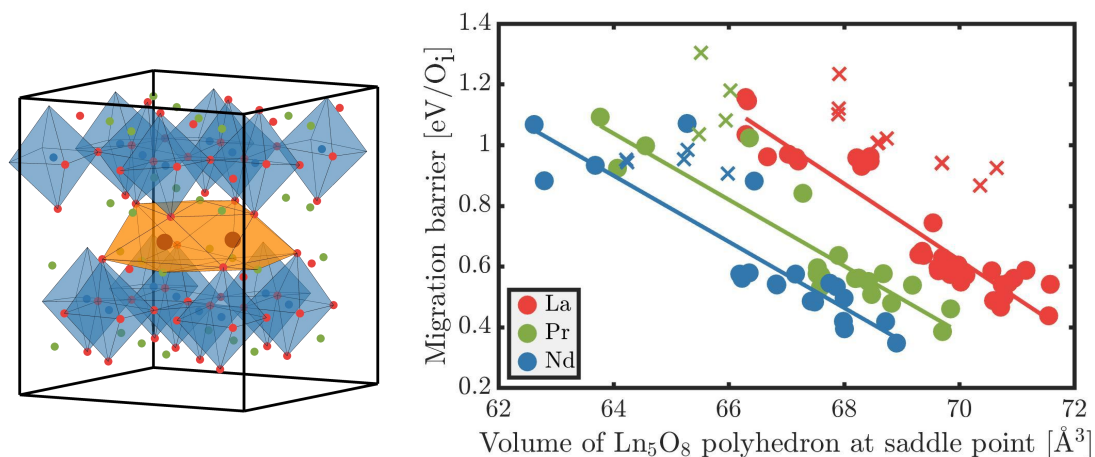


Figure 6.13: Example of Ln_5O_8 polyhedron. Shaded orange and blue regions are the Ln_5O_8 polyhedra and NiO_6 octahedra. Green, red, blue, and black spheres represent Ln , oxygen, Ni, and the mobile oxygen atom. The migration barrier as a function of the Ln_5O_8 volume is also shown. Best fit lines are given for each Ln . Points shown as 'x' have unit cells which define two or more of the Ln vertices on the Ln_5O_8 polyhedron to be the same atom due to periodic boundary conditions. These points are treated as outliers and excluded from the best fit line.

remains elusive.

The arrangement of excess oxygen was shown to have a significant effect on the formation energy, migration barrier, and activation energy but a clear explanation for how and why this happens has not been found. The exact arrangement of excess oxygen is neither perfectly ordered nor completely known experimentally. If the experimental arrangement of excess oxygen was better known, it may be possible to better understand what controls the migration barrier in these materials. Several computational tests were performed in an attempt to better classify the experimental arrangement of excess oxygen. These tests required either many thousands of structures to be relaxed or extremely large unit cells with thousands of atoms - neither of which are practical to consider

with density functional theory. Simple classical potentials were used instead, as described in Section 6.10. Sections 6.11 and 6.12 discuss how structures with multiple excess oxygen atoms per unit cell were considered. Section 6.13 then describes how the classical potentials were used to investigate phonon broadening due to the arrangement of excess oxygen in these materials.

6.10 Classical potentials

Classical potentials are significantly less computationally expensive than density functional theory, a typical calculation takes seconds rather than days. These calculations are cheap enough that all of the possible excess oxygen atom arrangements can be considered with up to $N=2$ excess oxygen atoms per unit cell. Classical potentials also allow much larger unit cells to be considered, enabling a the calculation of phonon dispersion in large supercells as explained in Section 6.13.

The classical potential used was a Buckingham pair potential. The total energy of this potential combines the Coulomb energy with a short range interaction between each pair of ions [141, 142]:

$$E = \sum_{j>i} \sum_i \left[\frac{q_i q_j}{4\pi\epsilon_0 r_{ij}} + A_{ij} \exp\left(\frac{-r_{ij}}{\rho_{ij}}\right) - \left(\frac{C_{ij}}{r_{ij}^6}\right) \right] \quad (6.6)$$

where i and j index the ions, q_i is the charge of ion i , r_{ij} is the distance between ions i and j , and A_{ij} , ρ_{ij} , and C_{ij} are parameters of the Buckingham potential. The parameters used are taken from References [141] and [142] and are given in Table 6.1. These parameters are limited to $Ln=La$ or Pr and both have been specifically used to study $Ln_2NiO_{4+\delta}$. While Buckingham pair potentials exist for $Nd^{3+}-O^{2-}$, a set of parameters consistent with the La and Pr potentials used

Table 6.1: Parameters used in Buckingham potentials, from References [141] and [142].

Ion pair	A_{ij}/eV	$\rho_{ij}/\text{\AA}$	$C_{ij}/\text{eV \AA}^6$
$\text{La}^{3+}-\text{O}^{2-}$	2119.79	0.3459	23.25
$\text{Pr}^{3+}-\text{O}^{2-}$	2025.54	0.3427	13.85
$\text{Ni}^{2+}-\text{O}^{2-}$	905.40	0.3145	0.00
$\text{O}^{2-}-\text{O}^{2-}$	9547.96	0.2072	32.00

here that have been used to study $\text{Nd}_2\text{NiO}_{4+\delta}$ was not found. Thus $\text{Nd}_2\text{NiO}_{4+\delta}$ was not studied using classical potentials.

The charge of each ion was assumed to be its formal valence state. When $\delta \neq 0$ the unit cell therefore has a net charge. A uniform background charge is applied in the unit cell in order to maintain overall charge neutrality.

Classical potential calculations were performed using the General Utility Lattice Program (GULP) [167]. This program can calculate or minimize energy and can also calculate the Hessian of a crystal structure.

6.11 Energetics of $\text{Pr}_2\text{NiO}_{4+\delta}$ using Buckingham potentials

Excess oxygen arrangements were enumerated with $N = 2$ for $\delta = 1/4$. Each arrangement was placed into a unit cell commensurate with the X point of $I4/mmm$ (so that each arrangement was commensurate with $P4_2/nm$ and $Cmca$). The resulting unit cells could have as many as $N = 8$ excess oxygen atoms. The arrangements were combined with each of the parent structures - $I4/mmm$, $P4_2/nm$, and $Cmca$ - and relaxed. No attempt was made to avoid du-

plicating symmetrically identical structures due to the low computational cost of these calculations. The resulting distribution of energies was similar for each parent structure, though the lowest energy structure for a particular arrangement could be any of the three parent structures.

Excess oxygen arrangements were also generated with $N = 2$ and $\delta = 1/5$, $1/8$, and $1/10$. These were only combined with the $P4_2/nm$ parent structure. This choice of parent was made to ensure each supercell allowed the X_3^+ octahedral rotations. The energies of each of the structures after relaxation are shown in Figure 6.14. In some cases the relaxation failed and the resulting structure was unphysical, with groups of atoms nearly on top of each other. Such cases were omitted from plots.

For each δ considered, there is a small number of structures with very low or high energies and a large number of structures with similar energies in between. The higher energy structures tend to arrange all of the excess oxygen into a single rock salt layer with several empty rock salt layers between the occupied layer. An obvious pattern in the low energy structures was not found. Energetically degenerate structures are usually identical by symmetry, as is the case for the lowest energy structure with $\delta = 1/4$.

6.12 Multiple excess oxygen atoms per cell using density functional theory

The energies shown in Figure 6.14 were used to help select several $\text{Pr}_2\text{NiO}_{4.25}$ structures to consider with density functional theory. Several of the lowest en-

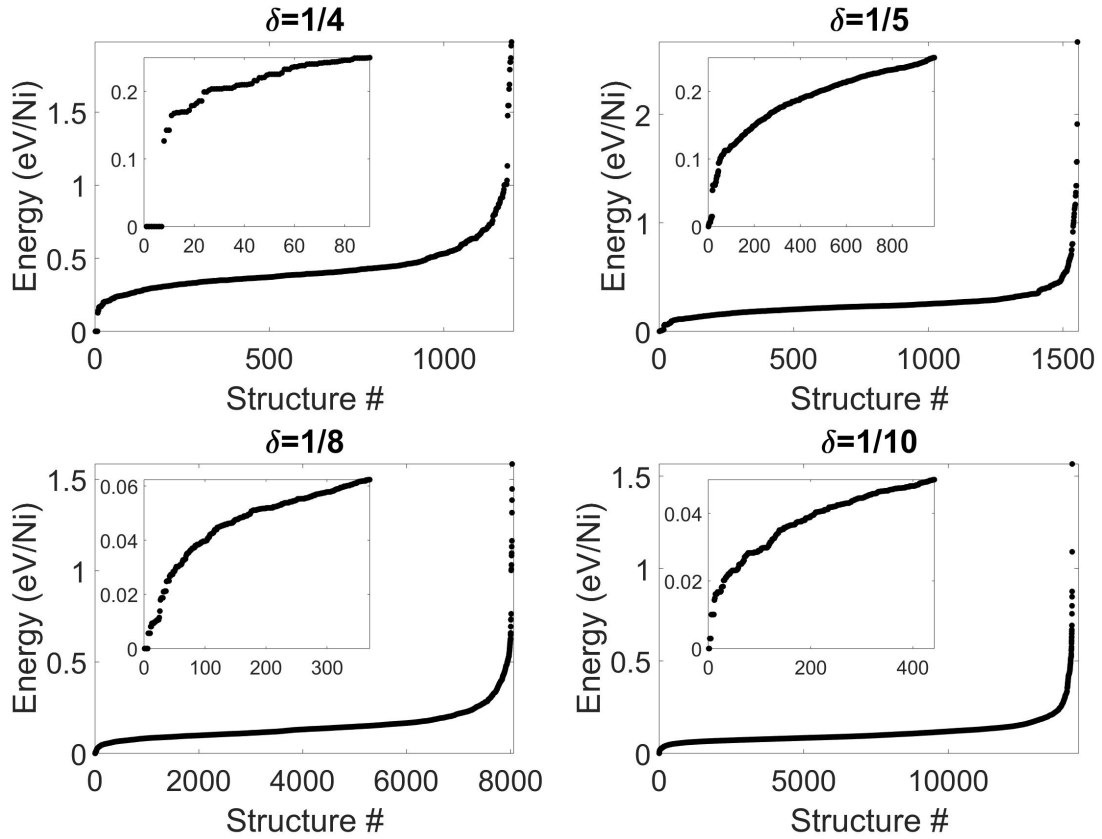


Figure 6.14: Energies of $\text{Pr}_2\text{NiO}_{4+\delta}$ after relaxation using Buckingham pair potentials. The structure # was determined by sorting the relaxed energies. The zero of energy for each δ is taken as the lowest energy structure. Insets highlight the low energy structures.

ergy structures were chosen as well as a random mix of higher energy structures for comparison. Excess oxygen arrangements with $N=2$ or 4 were chosen⁴. These structures were relaxed using density functional theory, as before. The relaxations were performed at the lattice constants of $I4/mmm$ so that a direct comparison could be made with previous results calculated with $N = 1$.

Based on experience in studying metallic alloys [156], it may be expected that

⁴Structures with $N = 8$ have 232 atoms which would be a very expensive calculation for the purposes here and were therefore excluded.

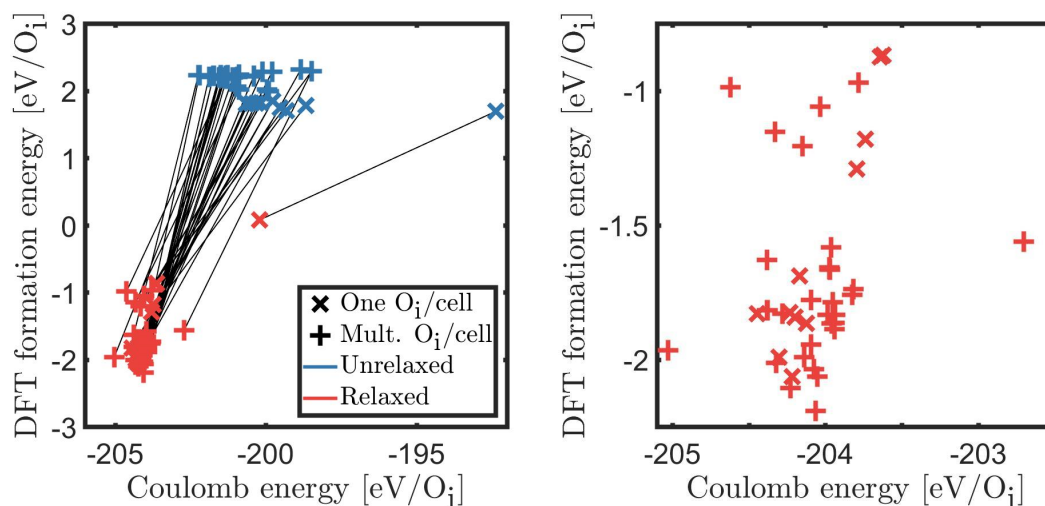


Figure 6.15: Density functional theory and Coulomb energies of $\text{Pr}_2\text{NiO}_{4.25}$ with various arrangements of excess oxygen. Blue points are the energy of an arrangement combined with the $I4/mmm$ structure before any relaxation. Red points are after relaxation. Lines connect points before and after relaxation. The plot to the right is zoomed in on the low energy relaxed structures and omits connecting lines for clarity.

Coulomb repulsion will dictate the arrangement of excess oxygen atoms. This does not seem to be the case - the Coulomb energy of an arrangement before and after relaxation is not linearly related to the formation energy as calculated within density functional theory, even in the case of $N=1$. A plot summarizing this point is given in Figure 6.15.

Evidently other factors, such as structural distortions can play a significant role in stabilizing a particular arrangement. These effects are partially captured by the short range interactions in the Buckingham potential. A plot showing the relationship between the energy of structures relaxed with Buckingham potentials and structures relaxed with density functional theory is shown in Figure 6.16. The relationship between Buckingham and density functional theory

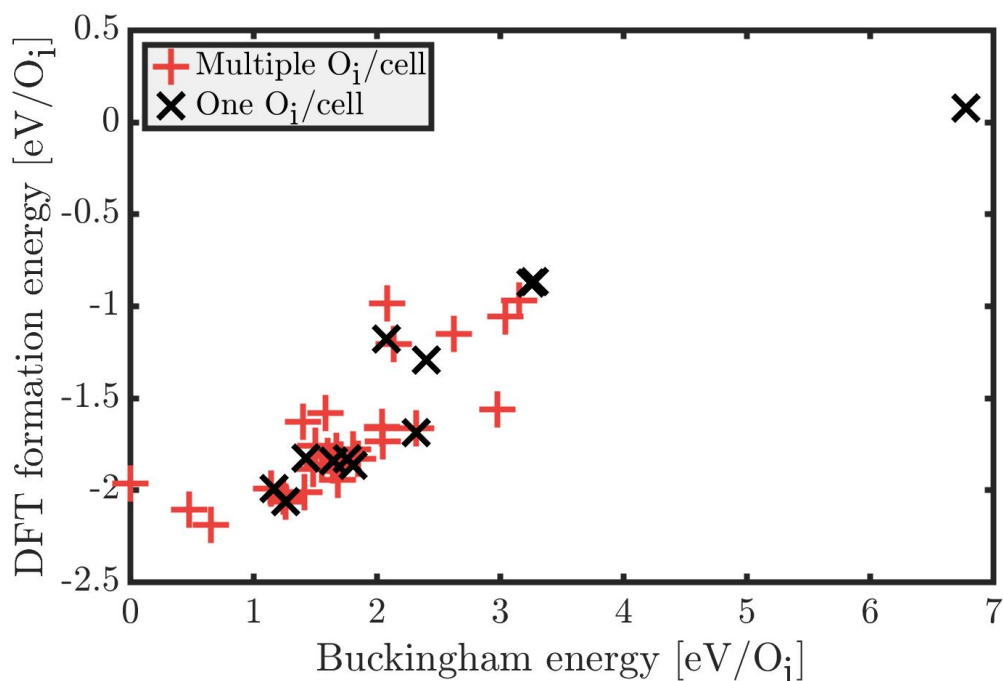


Figure 6.16: Density functional theory and Buckingham potential energies of $\text{Pr}_2\text{NiO}_{4.25}$ with various arrangements of excess oxygen. Red '+' symbols have $N = 2$ or 4 , black 'x' symbols have $N = 1$.

energies isn't perfect, as expected, but there is a clear correlation between the two. It should therefore be possible to use Buckingham potentials as a screening tool to select which excess oxygen arrangements to consider with density functional theory.

The lowest formation energy $\text{Pr}_2\text{NiO}_{4.25}$ structure considered has $N=4$ and is roughly 0.1 eV/O_i lower in energy than any other structure. The structure, shown in Figure 6.17, has excess oxygen atoms arranged in a pattern which induces octahedral rotations in a complex, but coherent pattern (meaning the expected rotations due to each excess oxygen atom 'interfere' constructively). Other low energy structures tend to also have some kind of coherent pattern of

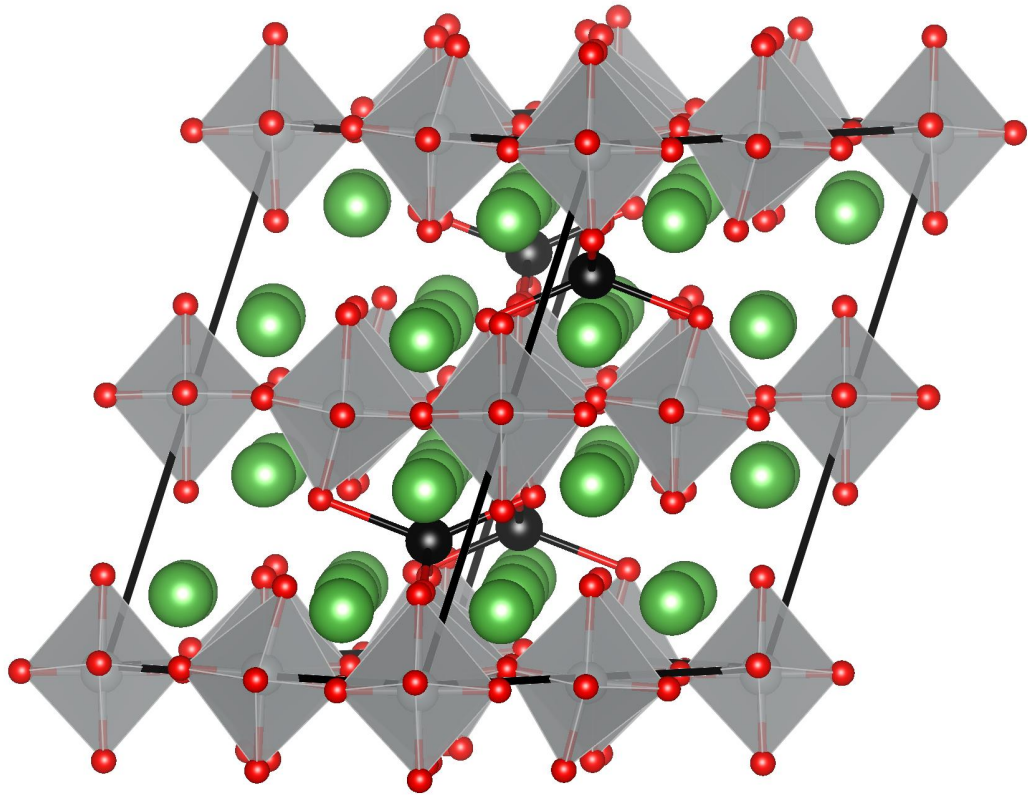


Figure 6.17: The lowest energy $\text{Pr}_2\text{NiO}_{4.25}$ structure. Green, gray, red, and black spheres represent Ln , Ni, oxygen, and the excess oxygen. Shaded gray regions are NiO_6 octahedra.

rotations as well, highlighting the importance of structural distortions.

Calculating migration barriers for arrangements with $N > 1$ is far more complicated because the migration path may take several steps with each excess oxygen atom in the unit cell moving independently, potentially in different (and distinct) directions. A single migration barrier calculation was attempted with $N=2$ in which both excess oxygen atoms moved simultaneously along the same direction. In this case the initial and final structures were identical by symmetry, which would not be the case if the ions moved in different directions or independently. After several steps of relaxation the migration path had relaxed

into what appeared to be a multiple step process in which the two ions moved one at a time. The CI-NEB algorithm is not designed to handle such multiple step energy barriers in one calculation so the calculation never converged (multiple step transitions should be treated as multiple independent CI-NEB calculations). Due to these complications, full consideration of migration barriers with $N > 1$ is left for future work.

6.13 Phonons in $Ln_2NiO_{4+\delta}$

The addition of excess oxygen atoms to the Ln_2NiO_4 crystal structure will alter its phonon dispersion. These changes can be treated as a perturbation and compared with phonons of Ln_2NiO_4 to gain insight into how the excess oxygen effects the phonon dispersion. Analyzing these changes may help quantify the arrangement of excess oxygen atoms.

The supercell lattice dynamics (SCLD) method was recently developed to quantify the phonon dispersion of a crystal structure with some static disorder [168, 169]. The arrangement of excess oxygen in a real sample of $Ln_2NiO_{4+\delta}$ is almost certainly disordered to some extent so the SCLD method was used to study the phonon dispersion of $Ln_2NiO_{4+\delta}$.

6.13.1 Supercell lattice dynamics method

A phonon dispersion can be measured experimentally using inelastic neutron scattering. This experiment measures the change in momentum and kinetic energy of neutrons scattering from a crystal structure to determine the momentum

and energy of phonons using conservation laws. In contrast, the SCLD method directly computes the energy of each phonon and determines the points in reciprocal space that contribute to each phonon using a Brillouin zone unfolding method. The energies are determined from the eigenvalues of the dynamical matrix (the Hessian matrix scaled by the mass of each atom) and converted into a frequency ω . The eigenvectors of the dynamical matrix are Fourier transformed to determine how much each wave vector \mathbf{k} contributes to the eigenvector.

The SCLD method is based on a dynamical matrix calculated in real space using a large supercell containing N_{cells} primitive unit cells of a parent structure. The atoms in each primitive cell are indexed by j while each primitive cell is indexed by ℓ . Based on the dynamical matrix, a function $\rho(\mathbf{k}, \omega)$ can be defined which corresponds to the expected count frequency of inelastically scattered neutrons with momentum \mathbf{k} and energy ω [168, 169]

$$\rho(\mathbf{k}, \omega) = \sum_j \sum_v \frac{\delta(\omega - \omega_v)}{N_{\text{cells}}} \sum_\alpha \left| \sum_\ell \mathbf{e}_{v,\ell,j,\alpha} e^{-2\pi i \mathbf{k} \cdot \mathbf{r}_{j\ell}} \right|^2 \quad (6.7)$$

where v indexes the eigenvectors \mathbf{e} and eigenvalues ω_v of the dynamical matrix, α runs over Cartesian directions, and $\mathbf{r}_{j\ell}$ is the position of ion j in primitive cell ℓ . The innermost sum of Equation 6.7 is a Fourier transform of specific components of the eigenvector, corresponding to the same atom in each primitive unit cell. This essentially picks out the amount of atomic vibrations along a direction α involving a particular atom j in the primitive unit cell at wave vector \mathbf{k} . The rest of the equation sums all the distinct contributions to get a single value for $\rho(\mathbf{k}, \omega)$. The contribution to ρ from a specific set of atoms j may be computed by omitting the sum over j in this equation, which can prove useful for interpreting

the phonon dispersion.

As written, Equation 6.7 will result in a phonon dispersion discretized in \mathbf{k} which is consistent with the standard phonon dispersion calculation method. The standard method for calculating a phonon dispersion multiplies the dynamical matrix by a phase factor of $\exp(i\mathbf{k} \cdot \mathbf{r})$ and diagonalizes at arbitrary \mathbf{k} to generate the dispersion [170]. The SCLD method differs from the standard method by averaging $\rho(\mathbf{k}, \omega)$ over equivalent \mathbf{k} in reciprocal space in order to average over equivalent domains in a disordered structure, as would occur in a real material. The method further averages $\rho(\mathbf{k}, \omega)$ over different crystal structures to mimic a disordered structure.

For a single crystal structure without any disorder in it (that is simply a large supercell of a crystal structure), Equation 6.7 can be reduced to

$$\rho(\mathbf{k}, \omega) = \sum_{\mathbf{v}} \delta(\omega - \omega_{\mathbf{v}}) \delta(\mathbf{k} - \mathbf{k}_{\mathbf{v}}) \quad (6.8)$$

This can be seen by noting that Fourier transform of any nondegenerate eigenvector of the primitive unit cell will result in zero except for a single $\mathbf{k}_{\mathbf{v}}$. When the Fourier transform is not zero the remaining sums will yield one⁵. In this case the value of $\rho(\mathbf{k}, \omega)$ must be a nonnegative integer.

The set of wave vectors relative to the parent structure, \mathbf{k}_p , commensurate with the supercell used to calculate the dynamical matrix determines which values of \mathbf{k} can be directly used to compute $\rho(\mathbf{k}, \omega)$. These wave vectors were determined by scanning over integer values of wave vectors in the supercell, \mathbf{k}_s , and solving for the corresponding \mathbf{k}_p in Equation 6.9, where \mathbf{S} is the supercell

⁵In the case of d -fold degenerate eigenvectors the total contribution of the degenerate eigenvectors to ρ at equivalent \mathbf{k} will be d , though the contributions from each eigenvector may be spread over several equivalent wave vectors.

matrix relating the primitive cell to the supercell. The search was terminated once N_{cells} different \mathbf{k}_p were found (many may be equivalent by symmetry).

$$\begin{pmatrix} \mathbf{k}_{s,1} \\ \mathbf{k}_{s,2} \\ \mathbf{k}_{s,3} \end{pmatrix} = \begin{pmatrix} S_{11} & S_{12} & S_{13} \\ S_{21} & S_{22} & S_{23} \\ S_{31} & S_{32} & S_{33} \end{pmatrix} \begin{pmatrix} \mathbf{k}_{p,1} \\ \mathbf{k}_{p,2} \\ \mathbf{k}_{p,3} \end{pmatrix} \quad (6.9)$$

Each atom in the supercell must be mapped onto a corresponding atom in the primitive parent cell. When the supercell is undistorted this is trivial - each atom in the supercell is a periodic image of an atom in the primitive cell. In distorted structures, each atom in the supercell is projected into the primitive parent cell using the parent unit cells periodic boundaries. A nearest neighbor matching scheme was then used to map each atom onto one of the parent structure's atoms. Excess oxygen atoms were treated separately, effectively being assigned a distinct j from other atoms.

Following References [168] and [169], $\rho(\mathbf{k}, \omega)$ can be visualized by defining a matrix

$$P_{ij} = \int_{\omega_i}^{\omega_i + \delta\omega} \rho(\mathbf{k}_j, \omega) d\omega \quad (6.10)$$

The rows and columns of \mathbf{P} correspond to bins of frequency and wave vectors. This matrix corresponds to a discretized phonon dispersion and visualizing it with color indicating its value will be referred to as the SCLD phonon dispersion. The discretization of frequency is set by $\delta\omega$ and is somewhat arbitrarily defined to yield satisfactory visualizations. The value of \mathbf{P} corresponds to the degeneracy of phonon branches. For instance the acoustic mode at Γ will have a value of three because there are always three translation phonons with zero frequency, unless another phonon branch also happens to have nearly zero fre-

quency at Γ .

6.13.2 Demonstration of SCLD method

The SCLD method was implemented using both the $I4/mmm$ and $P4_2/nm$ structures as a parent structure. Once the overall method is implemented, all that differs when using a different parent structure is: the set of allowed \mathbf{k} in a given supercell, which \mathbf{k} are equivalent, and how ions are mapped onto primitive cells. The size of the supercell dictates the resolution in reciprocal space. Unit cells with several thousand atoms are required to achieve even a low resolution for the Ruddlesden-Popper phases of interest. Therefore, Buckingham potentials were used instead of density functional theory to calculate the dynamical matrices required for SCLD.

To demonstrate the SCLD method in the Ruddlesden-Popper phases, the dynamical matrix of the $I4/mmm$ and $P4_2/nm$ structures of La_2NiO_4 were calculated and analyzed. The SCLD phonon dispersions for these structures with standard phonon dispersions calculated with Buckingham potentials overlaid are shown in Figures 6.18 and 6.19. The paths through reciprocal space were determined using SeeK-path [171]. The path for $I4/mmm$ involves some points with positions that depend on ratios of the lattice constants and are therefore not simple ratios. Such points are not commensurate with any reasonably sized supercell and thus had to be omitted from consideration.

The agreement between the SCLD and standard phonon dispersions is perfect aside from two discrepancies. First, the discretization of the SCLD dispersion is very coarse and misses some fine details in the dispersion. This can be

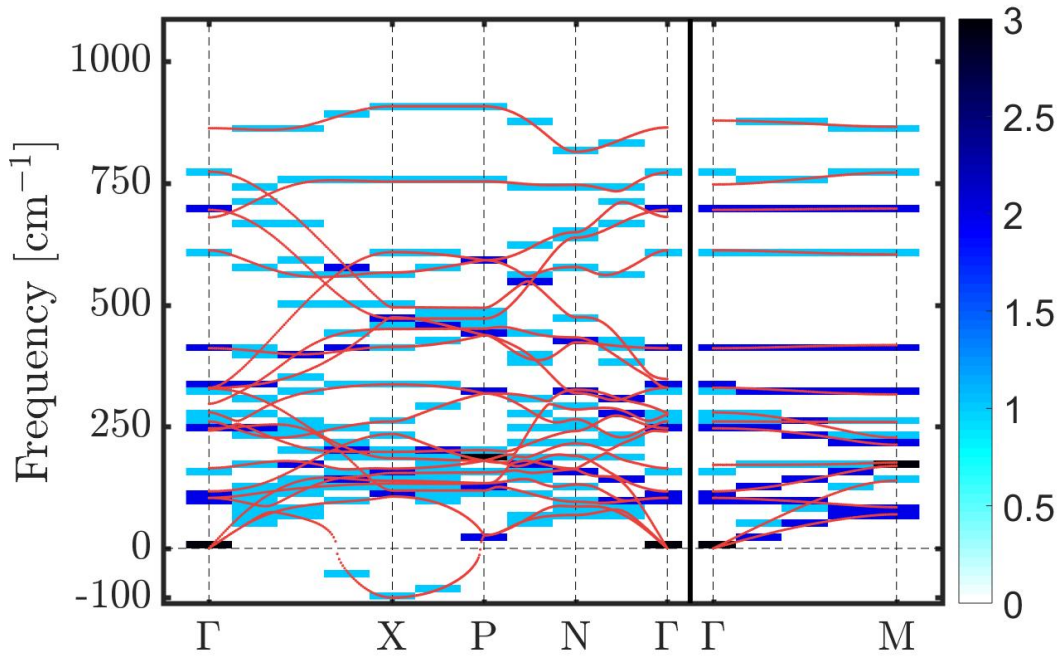


Figure 6.18: The SCLD phonon dispersion of I4/mmm using I4/mmm as the parent structure. The standard phonon dispersion of I4/mmm is overlaid in red.

seen at low frequencies along the $\Gamma - X$ or $Z - X$ lines in Figure 6.19, where the actual phonon dispersion has slight dips in frequency. The SCLD method would capture these if a larger supercell was used to make the discretization finer. The second difference comes from LO-TO splitting, which alters the frequencies at Γ [170]. The standard phonon dispersion includes a correction for LO-TO splitting while the phonon dispersion from the SCLD method does not. The materials of interest are metallic so LO-TO splitting was not usually included in calculations. Nonetheless, the LO-TO splitting correction can be used within SCLD and then the phonon frequencies match the standard calculation at Γ . The SCLD method therefore reproduces the standard phonon dispersions as well as can be expected, signifying the implementation of SCLD is working.

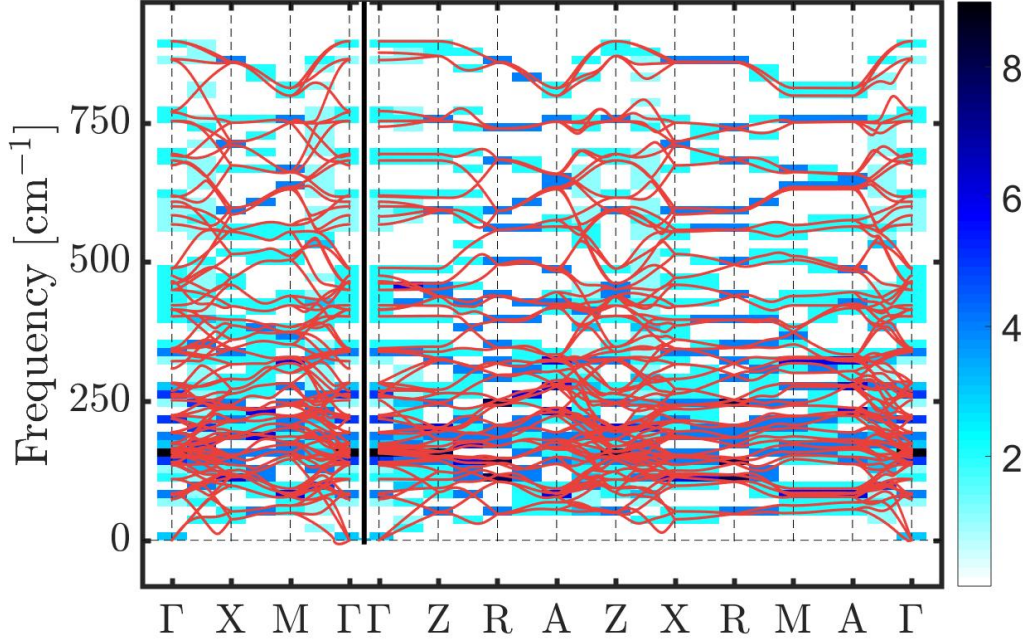


Figure 6.19: The SCLD phonon dispersion of $P4_2/ncm$ using $P4_2/ncm$ as the parent structure. The standard phonon dispersion of $P4_2/ncm$ is overlaid in red.

Several other checks can be performed to ensure the SCLD method was properly implemented. As discussed above, $\rho(\mathbf{k}, \omega)$ must be an integer when there is no disorder in the crystal structure. This was confirmed for the dispersions calculated in Figures 6.18 and 6.19. More generally an integral of ρ over all wave vectors and frequencies must result in the total number of degrees of freedom in the supercell, $3n_{\text{atoms}}N_{\text{cells}}$ where n_{atoms} is the number atoms in a primitive cell. This relation holds even in the case of noninteger n_{atoms} , which is the case when $\delta \neq 0$. Another sum rule holds for any \mathbf{k}

$$\int_{-\infty}^{\infty} \rho(\mathbf{k}, \omega) d\omega = 3n_{\text{atoms}} \quad (6.11)$$

These sum rules were checked whenever the SCLD method was used to help ensure the calculations were performed correctly.

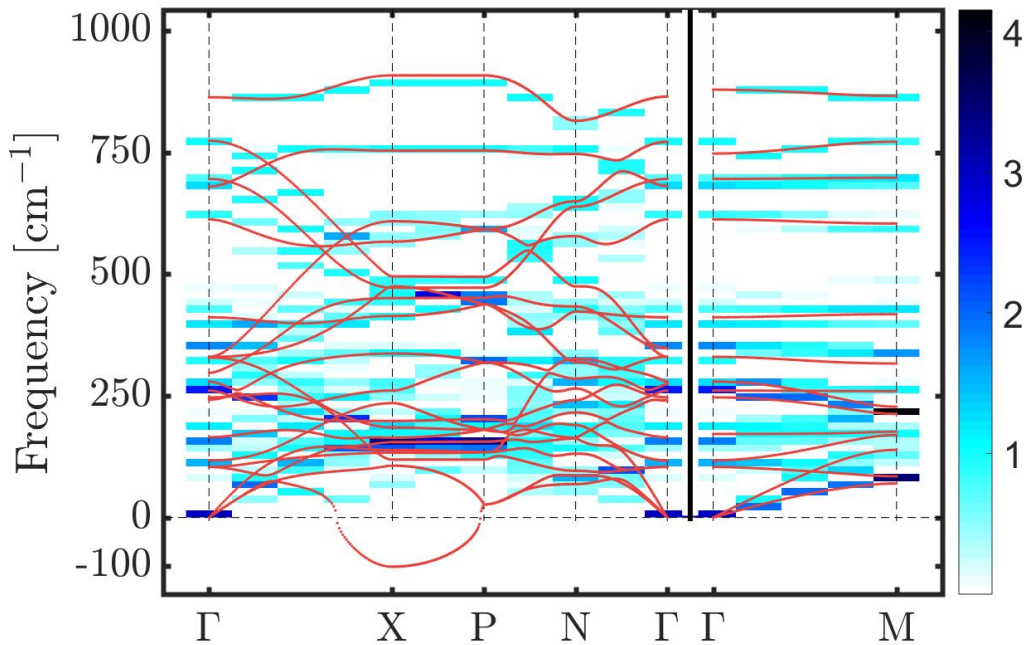


Figure 6.20: The SCLD phonon dispersion of $P4_2/ncm$ using $I4/mmm$ as the parent structure. The SCLD phonon dispersion is identical to that of Figure 6.19 except it has been unfolded into the $I4/mmm$ Brillouin zone. The standard phonon dispersion of $I4/mmm$ is overlaid in red.

The dynamical matrix of $P4_2/ncm$ was also analyzed using $I4/mmm$ as the parent structure. This effectively treats $P4_2/ncm$ as having some disorder relative to $I4/mmm$. Of course this structure is not truly disordered - it can be reached via an X_3^+ distortion from $I4/mmm$ so the structure is ordered, but in a larger cell than $I4/mmm$. Since this structure is not fully ordered within the $I4/mmm$ unit cell, ρ is not restricted to integer values, as evident in the phonon dispersion shown in Figure 6.20.

6.13.3 Analyzing individual wave vectors

While the visualization of P_{ij} is sufficient to get a basic idea of changes in the phonon dispersion relative to a simple parent structure, when there are more than a few phonon branches in the parent structure it quickly becomes challenging to interpret. This can be seen in Figure 6.20 - there are about 10 phonon branches in the I4/mmm parent structure within the frequency range of around 100-200 cm^{-1} on the $X - P$ line. Even if none of these branches crossed, the discretization in ω would make it very challenging to understand how these branches differ in the I4/mmm and P4₂/ncm structures. The SCLD method has thus far only been used in relatively simple systems [168, 169, 172] so some additional ideas were needed to analyze the significantly more complex Ruddlesden-Popper structures.

To better understand the phonon dispersion it is helpful to focus on a single wave vector at a time. The ρ function can also be broadened using some function of finite width, $F(\omega)$, rather than binning delta functions. Mathematically this amounts to convolving ρ with F :

$$\begin{aligned} Z(\mathbf{k}, \omega) &\equiv \int_{-\infty}^{\infty} \rho(\mathbf{k}, \omega') F(\omega - \omega') d\omega' \\ &= \sum_j \sum_v \frac{F(\omega - \omega_v)}{N_{\text{cells}}} \sum_{\alpha} \left| \sum_{\ell} \mathbf{e}_{v,\ell,j,\alpha} e^{-2\pi i \mathbf{k} \cdot \mathbf{r}_{j\ell}} \right|^2 \end{aligned} \quad (6.12)$$

$F(\omega)$ was taken to be a normalized Gaussian with a full width at half maximum of 20 cm^{-1} . Neutron cross sections were adjusted for by multiplying Equation 6.12 by σ_j in order to make a more direct comparison with experiment. Using this definition the phonon dispersion can be easily visualized at any wave vector and should be similar to what would be measured in an inelastic neutron scattering experiment. An example of Z calculated at the X point

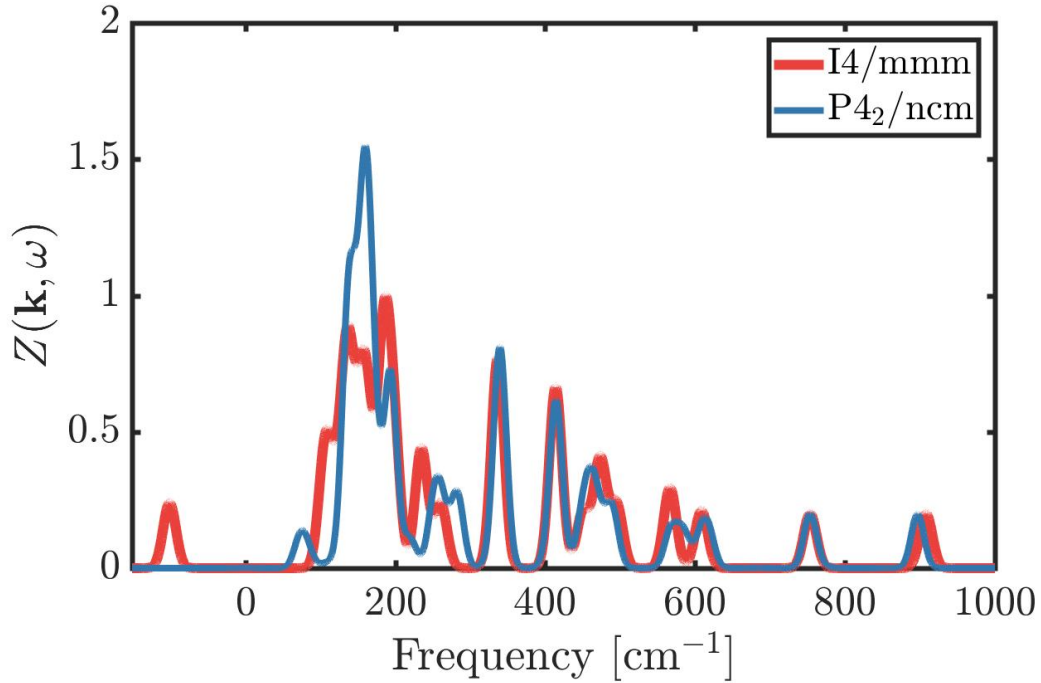


Figure 6.21: $Z(\mathbf{k} = X, \omega)$ for La_2NiO_4 in the $I4/mmm$ and $P4_2/ncm$ structures, using $I4/mmm$ as the parent structure.

of Figure 6.20 is given in Figure 6.21. This gives another view of the phonon dispersion that can help understand changes in the dispersion. For instance the numerous peaks just below 200 cm^{-1} in $I4/mmm$ actually shift closer together in $P4_2/ncm$ to create what appears to be a single larger peak, which is not as evident in Figure 6.20.

An atom projected version of $Z(\mathbf{k}, \omega)$ can be calculated by selecting a single (or set of) j rather than summing over all j in Equation 6.12. Considering the oxygen contributions to $Z(\mathbf{k} = X, \omega)$ leads to the plot in Figure 6.22. The negative frequency phonon in $I4/mmm$ is seen to be mostly oxygen motion and appears to split into two peaks below 200 cm^{-1} in $P4_2/ncm$. This is precisely what is expected - the unstable phonon in $I4/mmm$ is the doubly degenerate X_3^+

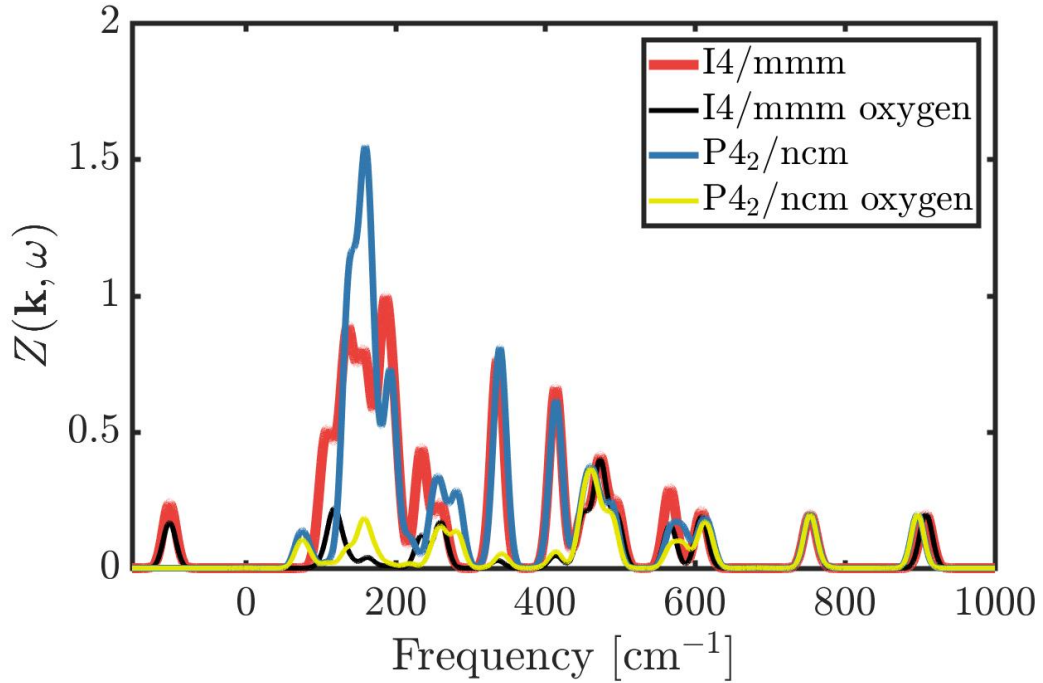


Figure 6.22: $Z(\mathbf{k} = X, \omega)$ for La_2NiO_4 in the $I4/mmm$ and $P4_2/ncm$ structures, using $I4/mmm$ as the parent structure. The contribution from only oxygen ions to Z is also shown.

octahedral rotation mode which leads to $P4_2/ncm$.

6.13.4 Ordered and disordered excess oxygen arrangements

Dynamical matrices were calculated and analyzed with SCLD for several random arrangements of excess oxygen atoms in $\text{Pr}_2\text{NiO}_{4.25}$ to demonstrate the effect ordering of the excess oxygen has on the phonon dispersion. These arrangements were generated in the large supercell being used for SCLD and cannot be represented using a smaller unit cell and should therefore be a reasonable approximation to disorder of the excess oxygen. $Z(\mathbf{k} = M, \omega)$ is shown in Fig-

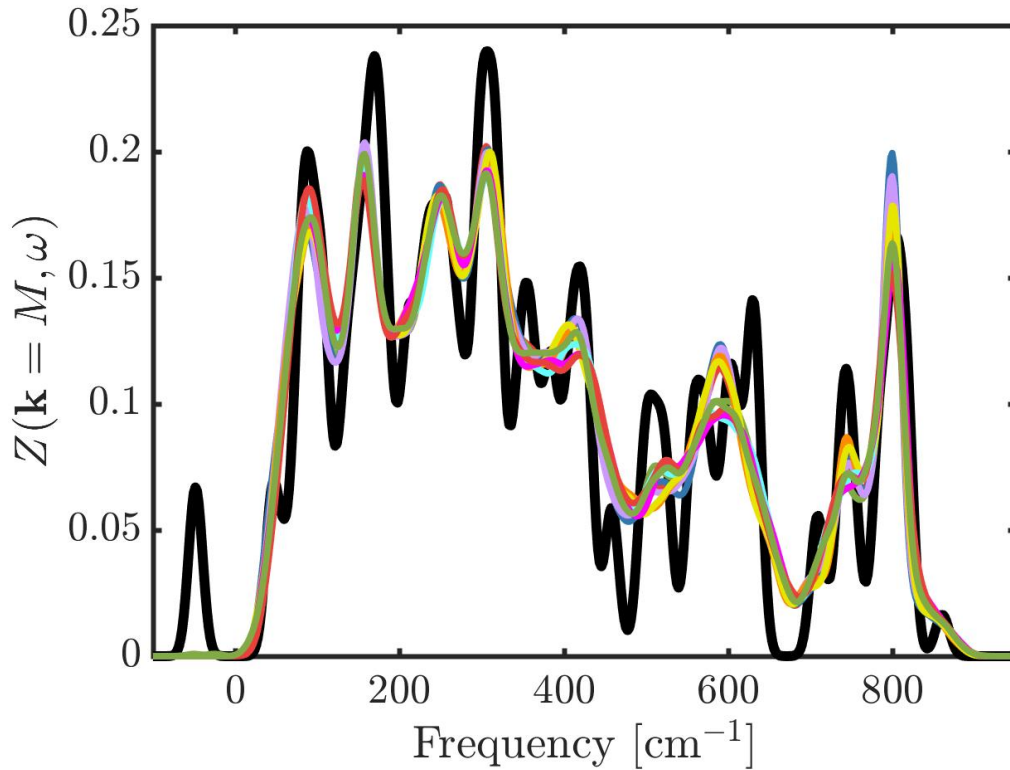


Figure 6.23: $Z(\mathbf{k} = M, \omega)$ for several $\text{Pr}_2\text{NiO}_{4.25}$ structures using $P4_2/nm$ as the parent structure. The black line is for a structure with a fully ordered arrangement of excess oxygen. Colored lines correspond to several random arrangements of excess oxygen.

Figure 6.23 for each of these random arrangements in various colors. As expected for a structure without ordering, the various peaks tend to be quite broad. These random arrangements of excess oxygen also all have very similar phonon dispersions, even at other wave vectors not shown here.

For comparison, $Z(\mathbf{k} = M, \omega)$ is shown in black for one of lowest energy (within density functional theory) $\text{Pr}_2\text{NiO}_{4.25}$ structures. This ordered arrangement produces a clearly distinct phonon dispersion with much sharper peaks in Z . The differences are not just in peak widths. There are additional peaks

in the ordered structure which are entirely absent from the randomly ordered structures, for instance the instability and the peak around 600 cm^{-1} .

6.13.5 Phonons in $\text{Pr}_2\text{NiO}_{4.25}$

The SCLD method was used to calculate phonon dispersions for 23 arrangements of excess oxygen in $\text{Pr}_2\text{NiO}_{4.25}$. Pr was used over La owing to its smaller ionic radius and corresponding tendency for larger distortions which are easier to study. The oxygen arrangements used include each arrangement with one excess oxygen atom per cell as well as several of the lower energy arrangements with multiple excess oxygen atoms per cell. Rather than averaging ρ across these structures, the average was weighted by a Boltzmann factor of $\exp(-E/k_B T)$. A weighted average was used to allow multiple excess oxygen arrangements while accounting for the significant difference in formation energies in these structures. The temperature used was 700 K, chosen as the temperature required for high oxygen ion mobility in these materials [113]. The resulting averaged phonon dispersion is shown in Figure 6.24. Despite the extremely complex phonon dispersion, it can be seen that several phonon instabilities were induced by the excess oxygen. These instabilities are most evident along the $M-A$ line but exist elsewhere in reciprocal space. The parent structure, $\text{P4}_2/\text{ncm}$, does not have any instabilities so these instabilities must be induced by the excess oxygen.

The form of the Buckingham potential in Equation 6.6 can be modified to adjust the influence of excess oxygen on the crystal structure in a continuous manner. This was done by introducing a parameter b to the potential which

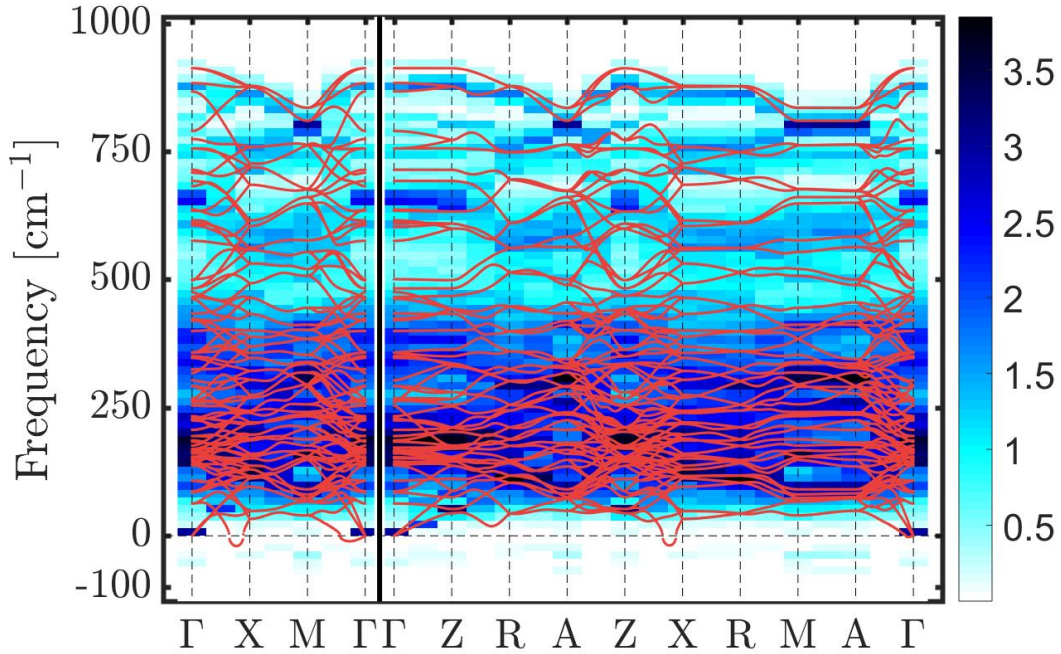


Figure 6.24: The averaged SCLD phonon dispersion of 23 $\text{Pr}_2\text{NiO}_{4.25}$ structures using $\text{P4}_2/\text{nm}$ as the parent structure. The standard phonon dispersion of $\text{P4}_2/\text{nm}$ is overlaid in red.

varies between 0 and 1. The charge q_j of excess oxygen atoms as well as any of the parameters A_{ij} and C_{ij} involving excess oxygen were multiplied by b . The resulting potential is given in Equation 6.13. In this equation α and β index excess oxygen atoms while i and j index all other kinds of atoms, including other oxygen atoms. The b parameter linearly scales any contribution to the total energy involving the excess oxygen atoms so when $b=0$ the excess oxygen atoms have no effect on the crystal structure⁶. By slowly reducing the influence of excess oxygen, the phonon modes which are softened by the excess oxygen can be identified.

⁶Formally this introduces a zero frequency phonon branch throughout reciprocal space because the excess oxygen are completely noninteracting. This branch was removed from all plots for clarity.

$$\begin{aligned}
E = & \sum_{j>i} \sum_i \left[\frac{q_i q_j}{4\pi\epsilon_0 r_{ij}} + A_{ij} \exp\left(\frac{-r_{ij}}{\rho_{ij}}\right) - \left(\frac{C_{ij}}{r_{ij}^6}\right) \right] + \\
& \sum_j \sum_\alpha \left[\frac{(bq_\alpha)q_j}{4\pi\epsilon_0 r_{\alpha j}} + bA_{\alpha j} \exp\left(\frac{-r_{\alpha j}}{\rho_{\alpha j}}\right) - \left(\frac{bC_{\alpha j}}{r_{\alpha j}^6}\right) \right] + \\
& \sum_{\beta>\alpha} \sum_\alpha \left[\frac{(bq_\alpha)(bq_\beta)}{4\pi\epsilon_0 r_{\alpha\beta}} + bA_{\alpha\beta} \exp\left(\frac{-r_{\alpha\beta}}{\rho_{\alpha\beta}}\right) - \left(\frac{bC_{\alpha\beta}}{r_{\alpha\beta}^6}\right) \right]
\end{aligned} \tag{6.13}$$

Dynamical matrices were calculated as a function of b for the lowest energy $\text{Pr}_2\text{NiO}_{4.25}$ structure which has an instability induced by the excess oxygen atom and only one excess oxygen atom per unit cell. The structure was relaxed before calculating the dynamical matrix. The starting structure for the relaxation was linearly interpolated between the relaxed $b=1$ structure and the $\text{P4}_2/\text{ncm}$ structure to ensure the $b=0$ dynamical matrix is exactly the same as the dynamical matrix when the excess oxygen atoms are actually removed from the system.

The low frequency region of $Z(\mathbf{k} = M, \omega)$ and the contributions from each set of elements are shown in Figure 6.25. Clear trends are evident as a function of b . The instability slowly increases in frequency as b is decreased. This mode is mostly due to Pr and oxygen, though the neutron cross section of Pr is smaller than either Ni or oxygen so the actual distortion associated with this mode is mostly Pr motion. The instability can be traced back to a phonon with frequency around 75 cm^{-1} in the $\text{P4}_2/\text{ncm}$ structure. While the excess oxygen atom induces this instability, it is not directly involved in the mode.

Phonon frequencies were calculated using density functional theory at the M point of $\text{P4}_2/\text{ncm}$ for the same structure analyzed in Figure 6.25. Several phonon frequencies soften in this structure relative to $\text{P4}_2/\text{ncm}$, but do not become unstable. Analyzing these phonon modes did not lead to any obvious

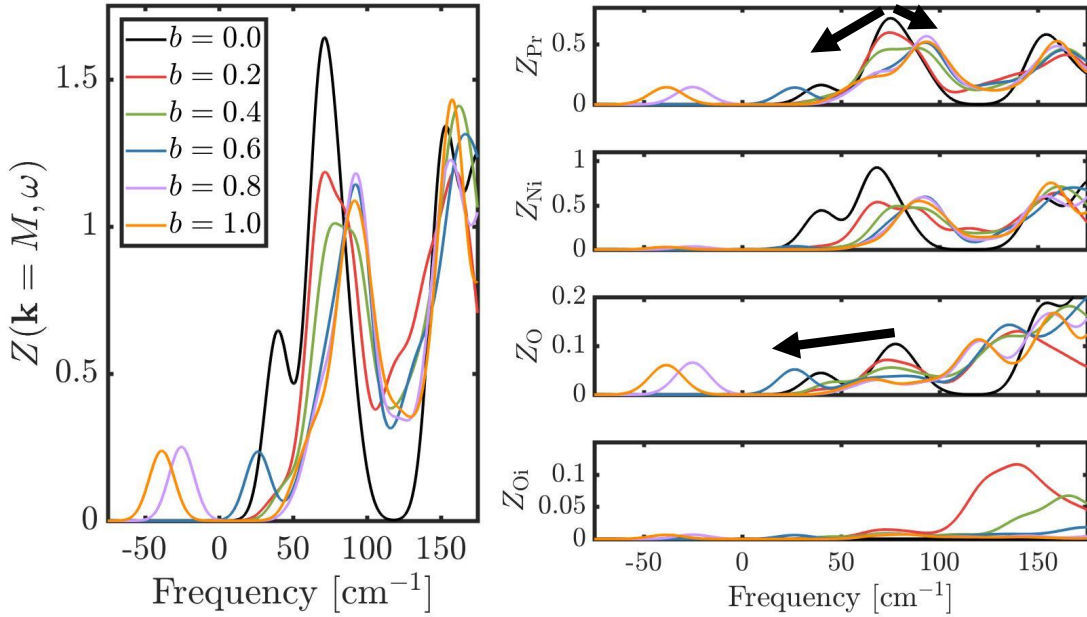


Figure 6.25: $Z(\mathbf{k} = M, \omega)$ and contributions to it from each element as calculated in a low energy $\text{Pr}_2\text{NiO}_{4.25}$ structure as a function of b . A peak around 75 cm^{-1} splits and shifts, as signified by arrows.

trends because the excess oxygen was either present or not, and the slightly softened modes had frequencies in the midst of many other phonons. Nonetheless, the softening of a phonon while using a simple classical potential suggests there is some physically simple mechanism which softens a particular phonon mode when excess oxygen is added to the system.

The softening of a phonon due to excess oxygen has been observed experimentally in $\text{Ln}_2\text{NiO}_{4+\delta}$ [144]. The analysis here may prove useful to understanding these and future experimental results.

6.14 Raman active phonons

The high frequency phonons in $Ln_2NiO_{4+\delta}$ shift significantly as a function of δ within density functional theory. Without considering the symmetry of specific modes, the highest frequency phonon drops by at least 100 cm^{-1} as δ increases from 0 to 0.25. A symmetry analysis of the phonons in $Ln_2NiO_{4+\delta}$ is more complicated than usual because once δ is nonzero the symmetry of the crystal structure is lowered and numerous irreps are mixed into each phonon. The addition of excess oxygen introduces several degrees of freedom to the system not present in Ln_2NiO_4 , further complicating a symmetry analysis of the phonons.

The symmetry of phonons in $Ln_2NiO_{4+\delta}$ was analyzed by diagonalizing the dynamical matrix as usual. Then the extra degrees of freedom corresponding to excess oxygen atoms were removed from each eigenvector. The calculated eigenvalues (phonon frequencies) and modified eigenvectors thus account for the excess oxygen in the system but the eigenvectors do not explicitly include the motion of excess oxygen. By removing these degrees of freedom, the modified eigenvectors can be projected onto the usual $I4/mmm$ or $P4_2/nm$ irreps in order to assign a symmetry label to each eigenvector. The symmetry of the eigenvectors is mixed (because the symmetry is lower than $I4/mmm$ or $P4_2/nm$) and labels were assigned based on the irrep with largest amplitude in each eigenvector. This labeling ignores smaller contributions to the modified eigenvectors but should give a reasonable picture of how the phonon frequencies shift.

Using this symmetry analysis, the largest shift of phonon frequency between $\delta=0$ and 0.25 is more than 150 cm^{-1} and effects the Raman active Γ_5^+ mode of

$P4_2/nm$. This shift is large enough that it should be easily observed using Raman spectroscopy. The frequency of this Γ_5^+ mode in $P4_2/nm$ is not significantly changed by the crystal structure - the frequency is nearly identical in $I4/mmm$ - suggesting some electronic mechanism may play a role.

Dynamical matrices were calculated for the $P4_2/nm$ structure of Pr_2NiO_4 with electronic holes doped into the system to test the effect of holes on the frequency of the Γ_5^+ mode. No changes were made to the crystal structure so that the only change in these calculations was the number of electrons. The frequency of this mode changes by more than 200 cm^{-1} after doping holes corresponding to $\delta=0.25$ into the system, as shown in Figure 6.26.

A dynamical matrix was also calculated for several structures with nonzero δ . These structures must be commensurate with the Γ point of $P4_2/nm$ so only a few structures could be considered. Three $\delta=1/4$ structures were considered, two of which have multiple excess oxygen atoms in the unit cell (only one of the excess oxygen arrangements with a single excess oxygen atom per cell and $\delta=1/4$ is commensurate with Γ). Four $\delta=1/8$ structures were considered, each with distinct excess oxygen arrangements. Only a single $\delta=1/16$ structure was considered because of the large computational cost to obtain a dynamical matrix for a low symmetry structure in a large unit cell. The resulting Γ_5^+ frequency in each structure is shown in Figure 6.26.

There is remarkable agreement between the phonon frequencies of Γ_5^+ in hole doped Pr_2NiO_4 in the $P4_2/nm$ structure and $Pr_2NiO_{4+\delta}$ despite the differences in crystal structure. The agreement is within 0.2% for $\delta=1/16$ and within 2.5% for $\delta=1/8$. In these cases it seems that electronic hole doping can almost entirely explain the change in frequency of Γ_5^+ . There is a larger spread of around 18%

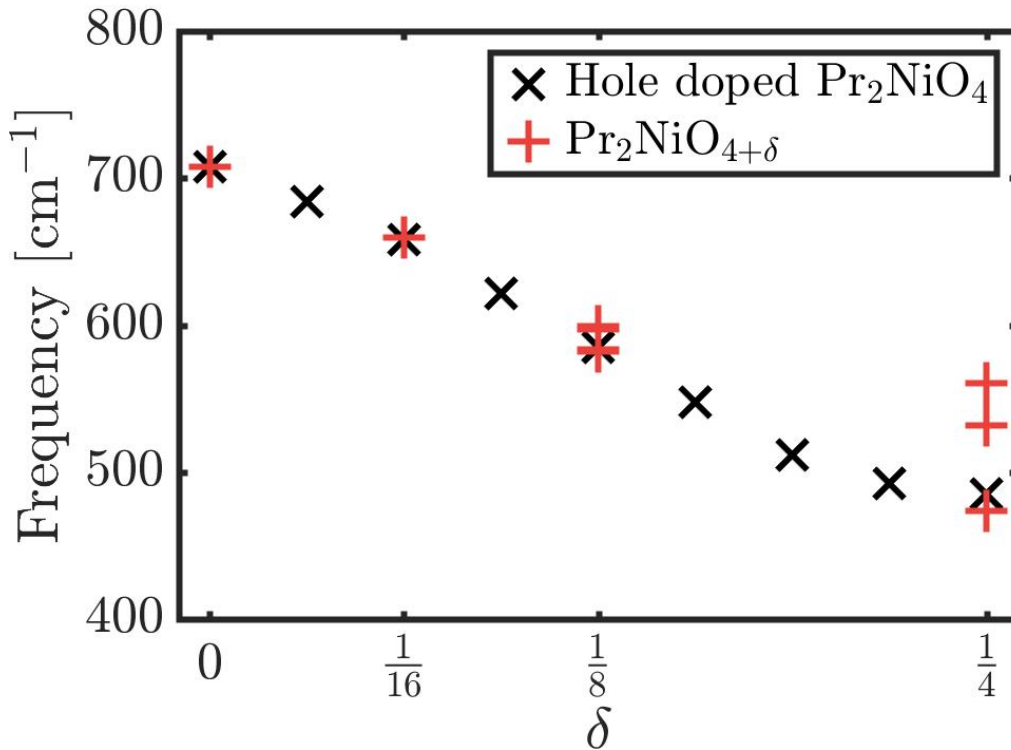


Figure 6.26: Frequency of the highest frequency phonon involving mostly the Γ_5^+ irrep as defined with respect to $P4_2/nm$ (the X_1^+ irrep with respect to $I4/mmm$) for several structures. Red '+' symbols are relaxed $\text{Pr}_2\text{NiO}_{4+\delta}$ structures commensurate with the X point of $I4/mmm$. Black 'x' symbols are the $P4_2/nm$ structure doped with holes corresponding to two holes per excess oxygen atom (2δ).

(roughly 100 cm^{-1}) for $\delta=1/4$, suggesting the lattice has an effect on the phonon frequency for very high densities of excess oxygen.

6.15 Discussion

The importance of the arrangement of excess oxygen in $\text{Ln}_2\text{NiO}_{4+\delta}$ was investigated in detail. The arrangement has a significant effect on both formation

energies and migration barriers for ionic transport, as discussed in Sections 6.8 and 6.9. The large range of energies found for large δ is partly due to a full enumeration of possible arrangements, which includes some that will clearly result in a high energy. However, significant differences in energy were seen between arrangements in conventional orthogonal unit cells relative to the lowest energy arrangements found. These results should be kept in mind for future studies of these materials, both experimentally when the exact crystal structure may be important and in computational studies which should take great care in defining unit cells for use in simulations. The calculations discussed here provide clear evidence that some arrangements of excess oxygen are energetically preferable, consistent with the range of structures observed experimentally.

Section 6.14 demonstrated that a Raman active phonon changes frequency dramatically with δ , suggesting δ may be measured using Raman spectroscopy. If this proves to be possible it may simplify future experiments involving $Ln_2NiO_{4+\delta}$. This may be particularly useful for tracking changes to δ which are known to happen as a function of temperature in air.

CHAPTER 7

SUMMARY AND FUTURE WORK

The crystal structure of several materials was studied using computational methods, primarily density functional theory. In each study the goal was to understand what controls the crystal structure using physical and chemical ideas. The crystal structure is closely linked to macroscopic properties so this understanding can suggest ways to control macroscopic properties via modifications of the crystal structure.

The novel crystal structure of $\text{La}_2\text{SrCr}_2\text{O}_7$ was shown to be determined by a cooperative coupling between octahedral rotations and disorder between the La and Sr atoms. The driving force of the cooperative coupling was shown to be the electronic energy preference of Cr ions to be in a regular octahedral environment. The strength of this preference can be controlled by changing Cr to another transition metal and is easily quantified using the ligand-field stabilization energy of an ion, suggesting a route to control the amount of disorder in similar materials. This new kind of coupling suggests a possible route towards altering the rotation pattern of $n=2$ Ruddlesden-Popper structures. Certain rotation patterns induce a net polarization, so future work may be done to try and control the rotation pattern using this coupling to design new polar materials.

The crystal structure of PbZrO_3 was studied in order to help understand why it exhibits antiferroelectricity. A search for low energy polar structures identified two closely related candidate structures for an electric field induced polar phase. Comparison of these polar structures with the known nonpolar ground state of PbZrO_3 suggested the existence of other structures which may be similarly low in energy. Calculations revealed this to be the case and found

an infinite set of low energy structures. A detailed structural model was developed which highlights the relevant distortions in these structures and explains why the nonpolar and polar structures are close in energy. This newly realized relationship between the nonpolar and polar structures of PbZrO_3 allowed the calculation of switching pathways that may be followed during an electric field induced nonpolar to polar phase transition. The switching pathways differ in the length scale of the crystal structure which switches simultaneously. There is almost no preference for any particular switching path to be followed which means switching can proceed over arbitrarily short or long length scales, and gives insight into why a nonpolar to polar phase transition can be induced with an electric field in PbZrO_3 .

There are low energy barriers between the infinite set of low energy structures in PbZrO_3 . The energy landscape of PbZrO_3 thus has a relatively flat region which connects its nonpolar ground state to polar structures. This kind of energy landscape has not been noticed before and may be a signature of antiferroelectricity. Initial calculations in several non-antiferroelectric materials confirmed the energy landscape was not similar to that of PbZrO_3 . If this mechanism proves to be a defining feature of antiferroelectricity it would be possible to design new antiferroelectrics by searching for, or designing new materials with similarly flat energy landscapes.

Preliminary analysis of NaNbO_3 , a known antiferroelectric, revealed that it has a relatively flat energy landscape corresponding to structures with $a^-a^-c^*$ octahedral rotations where the c^* means an arbitrary pattern of rotations with equal amplitude rotations about the c axis. The irreps involved in this rotation pattern couple to cation displacements in the c plane which give rise to local

dipoles, similar to the Pb displacements in PbZrO_3 . Further studies of NaNbO_3 are warranted but it appears to be a hybrid improper antiferroelectric.

The crystal structure of $\text{Ln}_2\text{NiO}_{4+\delta}$ was studied to gain insight into its ionic transport properties. The arrangement of excess oxygen in this material was shown to have a significant effect on the formation energy of interstitial oxygen and its migration barrier for ionic transport. Future computational studies of this class of materials should handle these possible arrangements carefully in order to better mimic the various arrangements seen in experiments. The SCLD method was implemented to study the effect of excess oxygen on phonons in $\text{Ln}_2\text{NiO}_{4+\delta}$. Changes in the phonon dispersion were clearly seen and may be helpful for interpreting experimentally measured phonon dispersions in these materials. A Raman active phonon shifts its frequency as a function of the number of electronic holes in the system, which are induced by excess oxygen, so Raman spectroscopy may be used to quantify the amount of excess oxygen in these materials. This idea is relatively simple to test and could simplify future experiments which require precise measurements of δ .

Future computational and experimental work on $\text{Ln}_2\text{NiO}_{4+\delta}$ could focus on better identifying the crystal structure. The structure is very complex, and is likely neither completely ordered nor disordered. Another possible research direction is to better understand what determines the arrangement of excess oxygen atoms in order to try and control it. If this arrangement could be arbitrarily controlled, the formation energy contribution to the activation energy of ionic transport could be neglected and significantly lower migration barriers may become accessible.

The study of complex crystal structures is necessary to understand the prop-

erties of many materials used in modern devices. Computational techniques have been developed that allow crystal structures to be simulated, enabling in depth theoretical studies to be performed without having to synthesize materials. The work presented in this dissertation demonstrated how these techniques can be applied in combination with physical and chemical ideas learn about a diverse set of properties within several classes of materials.

APPENDIX A
ADDITIONAL POLAR STRUCTURES IN PbZrO_3

Table A.1: A selection of structures found in the structure search for low energy polar structures. Every metastable polar phase found is included, while some nonpolar structures were excluded. En. A and B are the energy of structure in a fixed unit cell and the fully relaxed unit cell.

Space Group	Alt. Settings	Γ_4^-	R_4^+	M_3^+	Σ_2	Mod. Glazer	Pol. ($\mu\text{C}/\text{cm}^2$)	Vol. ($\text{\AA}^3/\text{f.u.}$)	En. A (meV/f.u.)	En. B (meV/f.u.)
221 Pm $\bar{3}$ m						$a_0^0 a_0^0 a_0^0$	0	71.08	278	278
53 Pmma	Pbmm				(0, a)		0	71.25	154	153
127 P4/mbm				(0, 0, a)		$a_0^0 a_0^0 c_0^+$	0	69.82	132	109
204 Im $\bar{3}$				(a, a, a)		$a_0^+ a_0^+ a_0^+$	0	70.10	113	108
139 I4/mmm				(a, a, 0)		$a_0^+ a_0^0 c_0^0$	0	70.01	115	106
140 I4/mcm			(0, 0, a)			$a_0^0 a_0^0 c_0^0$	0	69.72	110	88
99 P4mm		(0, 0, a)				$a_0^0 a_0^0 c_0^+$	71	72.07	110	83
28 Pma2	P2cm	(a, a, 0)	(0, 0, b)		(c, 0)		18	70.16	82	77
46 Ima2	Ima2	(0, 0, a)	(b, b, 0)			$a_0^- a_0^- c_0^0$	64	71.90	80	68
25 Pmm2	P2mm	(a, a, 0)	(b, \bar{b})		(c, 0)		41	71.14	71	67
38 Amm2		(0, 0, a)		(b, 0, 0)		$a_0^+ b_0^0 c_0^0$	54	71.00	67	63
100 P4bm		(0, 0, a)		(0, 0, b)		$a_0^0 a_0^0 c_0^+$	55	70.99	86	61
28 Pma2	Pbm2	(0, 0, a)			(b, 0)		58	72.24	75	60
107 I4mm		(0, 0, a)		(b, b, 0)		$a_0^+ a_0^+ c_0^0$	55	71.01	62	59
42 Fmm2		(0, 0, a)	(b, 0, 0)			$a_0^- a_0^0 c_0^0$	60	71.75	68	59
167 R $\bar{3}$ c			(a, a, a)			$a_0^- a_0^- a_0^-$	0	69.81	70	59
36 Cmc2 ₁		(0, 0, a)	(b, b, 0)	(c, c, 0)			54	71.16	60	57
137 P4 ₂ /nmc			(0, 0, a)	(b, b, 0)		$a_0^+ a_0^+ c_0^-$	0	69.85	64	55
38 Amm2	C2mm	(a, a, 0)				$a_0^0 a_0^0 c_0^0$	72	72.34	77	54
108 I4cm		(0, 0, a)	(0, 0, b)			$a_0^0 a_0^0 c_0^-$	51	70.74	77	54
31 Pnm2 ₁	Pnm2 ₁	(0, 0, a)	(b, \bar{b})		(c, 0)		52	72.03	59	53
63 Cmcm			(0, 0, a)	(0, b, 0)		$a_0^0 b_0^+ c_0^-$	0	69.77	65	51
26 Pmc2 ₁	Pb2 ₁ m	(a, \bar{a} , 0)			(b, c)		62	72.26	66	47
30 Pnc2	Pnc2	(0, 0, a)	(0, 0, b)		(c, 0)		52	71.26	59	47
38 Amm2		(a, 0, 0)	(b, 0, 0)	(0, 0, c)		$a_0^- b_0^0 c_0^+$	39	70.31	54	46
40 Ama2		(a, 0, 0)	(0, 0, b)	(0, c, 0)		$a_0^0 b_0^+ c_0^-$	32	70.28	48	45
6 Pm		(a, a, b)			(c, 0)		58	72.38	57	44
105 P4 ₂ mc		(0, 0, a)	(0, 0, b)	(c, c, 0)		$a_0^+ a_0^+ c_0^-$	40	70.38	50	44
74 Imma	Imcm		(a, a, 0)			$a_0^- a_0^- c_0^0$	0	69.78	58	44
55 Pbam	Pbam				(a, a)		0	72.23	62	43
108 Imm2		(0, 0, a)		(b, c, d)		$a_0^+ b_0^+ c_0^+$	43	70.69	45	41
31 Pnm2 ₁		(a, 0, 0)	(0, 0, b)	(c, d, e)			43	70.77	43	41
108 Fmm2		(a, a, 0)		(b, b, 0)		$a_0^+ a_0^+ c_0^0$	60	71.48	45	37
41 Aba2		(a, a, 0)	(0, 0, b)	(c, c, 0)		$a_0^+ a_0^+ c_0^-$	38	70.57	39	37
32 Pba2	Pba2	(0, 0, a)			(b, b)		36	72.28	49	37
36 Cmc2 ₁		(a, 0, 0)	(0, 0, b)	(c, 0, 0)		$a_0^+ b_0^0 c_0^-$	45	70.58	46	36
9 Cc		(0, a, b)	(c, 0, 0)	(0, d, 0)		$a_0^- b_0^+ c_0^+$	57	71.32	38	34
7 Pc		(a, b, 0)	(0, 0, c)	(d, e, f)			43	70.99	37	34
31 Pnm2 ₁		(a, 0, 0)	(0, 0, b)	(c, d, e)			41	70.57	37	33
8 Cm		(0, a, b)		(0, c, 0)		$a_0^0 b_0^+ c_0^+$	63	71.58	42	33
62 Pnma	Pnam		(a, a, 0)	(0, 0, b)		$a_0^- a_0^- c_0^+$	0	69.64	45	32
33 Pna2 ₁	Pna2 ₁	(0, 0, a)	(b, b, 0)	(0, 0, c)		$a_0^- a_0^- c_0^+$	40	70.35	39	31
1 P1		(a, b, c)		(0, 0, d)	(e, f)		60	71.89	35	28
160 R3m		(a, a, a)				$a_0^0 a_0^0 a_0^0$	75	72.61	46	28
31 Pnm2 ₁	P2 ₁ nm	(a, a, 0)	(b, \bar{b})	(0, 0, c)	(d, \bar{d})		23	70.88	30	28
7 Pc	P1a1	(a, a, b)		(0, 0, c)		$a_0^0 a_0^0 c_0^+$	72	72.42	40	28
31 Pnm2 ₁	Pn2 ₁ m	(a, \bar{a} , 0)	(b, b, 0)	(0, 0, c)		$a_0^- a_0^- c_0^+$	1	70.18	34	27
7 Pc	P1a1	(a, a, b)		(0, 0, c)		$a_0^0 a_0^0 c_0^+$	55	71.76	33	27
26 Pmc2 ₁	P2 ₁ am	(a, a, 0)		(0, 0, b)		$a_0^0 a_0^0 c_0^+$	55	71.77	33	27

Table A.1 continued

Space Group	Alt. Settings	Γ_4^-	R_4^+	M_3^+	Σ_2	Mod. Glazer	Pol. ($\mu\text{C}/\text{cm}^2$)	Vol. ($\text{\AA}^3/\text{f.u.}$)	En. A (meV/f.u.)	En. B (meV/f.u.)
8 Cm		(a, a, b)		$(c, c, 0)$		$a_+^+ a_+^+ c_+^0$	54	71.68	30	25
8 Cm		$(a, b, 0)$		(c, d, e)		$a_+^+ b_+^+ c_0^+$	52	71.25	26	25
146 R3		(a, a, a)		(b, b, b)		$a_+^+ a_+^+ a_+^+$	50	71.78	21	17
57 Pbcm	Pbcm		$(a, a, 0)$		$(0, b)$		0	70.32	20	15
46 Ima2	I2cm	$(a, a, 0)$	$(b, b, 0)$			$a_+^- a_+^- c_0^0$	57	71.00	18	10
28 Pma2	P2cm	$(a, a, 0)$	$(b, b, 0)$		$(c, 0)$		26	70.64	15	8
161 R3c		(a, a, a)	(b, b, b)			$a_+^- a_+^- a_+^-$	59	71.03	1	0
55 Pbam	Pbam		$(a, a, 0)$		(b, b)		0	70.68	6	0

APPENDIX B

UNIT CELL RELAXATION IN $\text{La}_2\text{NiO}_{4+\delta}$

The effects of unit cell relaxation were considered in $\text{La}_2\text{NiO}_{4+\delta}$. Figure B.1 shows the formation energies for cell relaxed structures relative to the energy in a unit cell corresponding to the I4/mmm lattice for each of the arrangements considered in Figure 6.9. Cell relaxation lowers the energy in all cases but does not make a significant difference in the relative energies between the various oxygen arrangements. The only significant change happens at very high energy and δ . This particular structure is a $1 \times 1 \times 4$ supercell, meaning it has a dense packing of excess oxygen in every 4th rock salt layer. In this type of structure significant changes to the unit cell make sense as the one densely packed layer will expand without significantly altering the rest of the structure.

The effect of unit cell relaxation on migration barriers was also examined in $\text{La}_2\text{NiO}_{4.125}$. Migration barriers were calculated in relaxed unit cells and are compared with the migration barriers in a unit cell fixed to the I4/mmm lattice in Figure B.2. These migration barriers were calculated with a unit cell fixed to that of the relaxed unit cell of the initial structure - the unit cell was not allowed to relax along the migration pathway. This means it is possible for the migration barrier to increase after cell relaxation. Figure B.2 shows there is little difference in the migration barriers whether the unit cell is fully relaxed or constrained to the I4/mmm lattice.

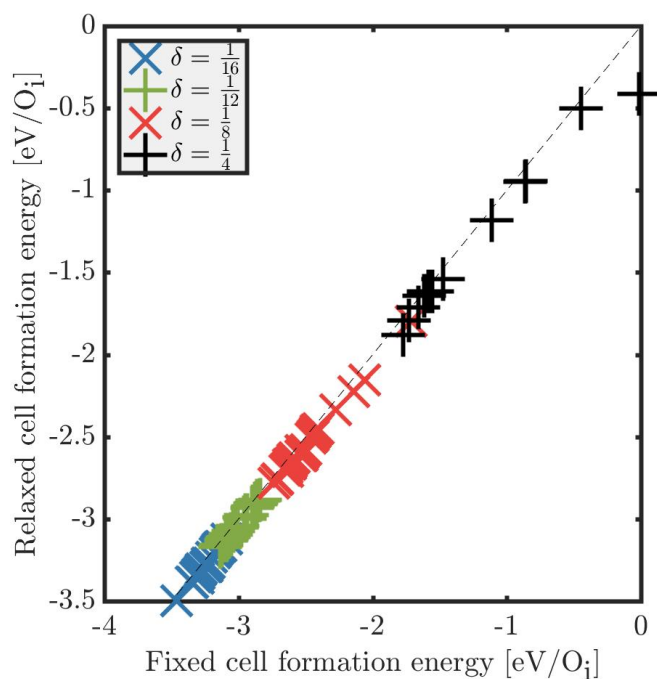


Figure B.1: Formation energies of $\text{La}_2\text{NiO}_{4+\delta}$ calculated in fully relaxed unit cells compared with the energy in a corresponding unit cell constrained to the $I4/mmm$ lattice.

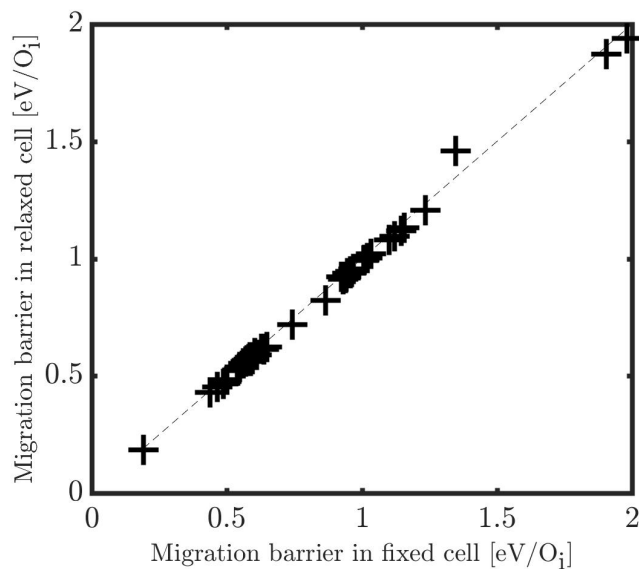


Figure B.2: Migration barriers of $\text{La}_2\text{NiO}_{4.125}$ calculated in fully relaxed unit cells compared with the energy in a corresponding unit cell constrained to the $I4/mmm$ lattice.

BIBLIOGRAPHY

- [1] J. Bardeen and W. H. Brattain, "The transistor, a semi-conductor triode," *Phys. Rev.*, vol. 74, pp. 230–231, Jul 1948.
- [2] B. G. Yacobi, *Semiconductor Materials An Introduction to Basic Principles*. Springer US, 1 ed., 2003.
- [3] N. Ashcroft and N. Mermin, *Solid State Physics*. Philadelphia: Saunders College, 1976.
- [4] S. N. Piramanayagam, "Perpendicular recording media for hard disk drives," *Journal of Applied Physics*, vol. 102, no. 1, p. 011301, 2007.
- [5] Y. Cao, V. Fatemi, S. Fang, K. Watanabe, T. Taniguchi, E. Kaxiras, and P. Jarillo-Herrero, "Unconventional superconductivity in magic-angle graphene superlattices," *Nature*, vol. 556, pp. 43 EP –, Mar 2018. Article.
- [6] E. Bousquet, M. Dawber, N. Stucki, C. Lichtensteiger, P. Hermet, S. Gariglio, J.-M. Triscone, and P. Ghosez, "Improper ferroelectricity in perovskite oxide artificial superlattices," *Nature*, vol. 452, pp. 732–736, 04 2008.
- [7] N. A. Benedek and C. J. Fennie, "Hybrid improper ferroelectricity: A mechanism for controllable polarization-magnetization coupling," *Phys. Rev. Lett.*, vol. 106, p. 107204, Mar 2011.
- [8] A. T. Mulder, N. A. Benedek, J. M. Rondinelli, and C. J. Fennie, "Turning abO_3 antiferroelectrics into ferroelectrics: Design rules for practical rotation-driven ferroelectricity in double perovskites and $A_2B_2O_7$ Ruddlesden-Popper compounds," *Advanced Functional Materials*, vol. 23, no. 38, pp. 4810–4820, 2013.
- [9] M. Aroyo, *International Table For Crystallography*, vol. A. Wiley, 6 ed., 2016.
- [10] H. Ibach and H. Lth, *Introduction to Solid State Physics*. Springer-Verlag Berlin Heidelberg, 4th ed., 2009.
- [11] C. Kittel, *Introduction to Solid State Physics*. New York: John Wiley & Sons, Inc., 6th ed., 1986.

- [12] M. S. Dresselhaus, G. Dresselhaus, and A. Jorio, *Group Theory Application to the Physics of Condensed Matter*. Springer-Verlag Berlin Heidelberg, 2008.
- [13] S. C. Miller and W. F. Love, *Tables of irreducible representations of space groups and co-representations of magnetic space groups*. Boulder, CO: Pruett Press, 1967.
- [14] A. P. Cracknell, *Kronecker product tables. Vol. 1, General introduction and tables of irreducible representations of space groups*. New York : IFI/Plenum, 1979.
- [15] D. S. Sholl and J. A. Steckel, *Density Functional Theory: A Practical Introduction*. Wiley, 2009.
- [16] J. Thijssen, *Computational Physics*. Cambridge University Press, second ed., 2007.
- [17] D. A. Keen and A. L. Goodwin, "The crystallography of correlated disorder," *Nature*, vol. 521, pp. 303 EP –, May 2015. Review Article.
- [18] K. Momma and F. Izumi, "VESTA: a three-dimensional visualization system for electronic and structural analysis," *Journal of Applied Crystallography*, vol. 41, pp. 653–658, Jun 2008.
- [19] H. T. Stokes and D. M. Hatch, "FINDSYM: program for identifying the space-group symmetry of a crystal," *Journal of Applied Crystallography*, vol. 38, pp. 237–238, Feb 2005.
- [20] M. I. Aroyo, D. Orobengoa, G. de la Flor, E. S. Tasci, J. M. Perez-Mato, and H. Wondratschek, "Brillouin-zone database on the Bilbao Crystallographic Server," *Acta Crystallographica Section A*, vol. 70, pp. 126–137, Mar 2014.
- [21] J. A. Alonso, M. J. Martínez-Lope, M. T. Casais, M. A. G. Aranda, and M. T. Fernández-Daz, "Metal-insulator transitions, structural and microstructural evolution of $R\text{NiO}_3$ ($R = \text{Sm}, \text{Eu}, \text{Gd}, \text{Dy}, \text{Ho}, \text{Y}$) perovskites: evidence for room-temperature charge disproportionation in monoclinic HoNiO_3 and YNiO_3 ," *Journal of the American Chemical Society*, vol. 121, no. 20, pp. 4754–4762, 1999.
- [22] J. Varignon, M. N. Grisolia, J. Íñiguez, A. Barthélémy, and M. Bibes, "Complete phase diagram of rare-earth nickelates from first-principles," *npj Quantum Materials*, vol. 2, no. 1, p. 21, 2017.

- [23] A. Mercy, J. Bieder, J. Íñiguez, and P. Ghosez, "Structurally triggered metal-insulator transition in rare-earth nickelates," *Nature Communications*, vol. 8, no. 1, p. 1677, 2017.
- [24] H. Guo, Z. W. Li, L. Zhao, Z. Hu, C. F. Chang, C.-Y. Kuo, W. Schmidt, A. Piovano, T. W. Pi, O. Sobolev, D. I. Khomskii, L. H. Tjeng, and A. C. Komarek, "Antiferromagnetic correlations in the metallic strongly correlated transition metal oxide LaNiO_3 ," *Nature Communications*, vol. 9, no. 1, p. 43, 2018.
- [25] A. M. Glazer, "The classification of tilted octahedra in perovskites," *Acta Crystallographica Section B*, vol. 28, pp. 3384–3392, Nov 1972.
- [26] M. Müller, R. E. Dinnebier, A.-C. Dippel, H. T. Stokes, and B. J. Campbell, "A symmetry-mode description of rigid-body rotations in crystalline solids: a case study of $\text{Mg}(\text{H}_2\text{O})_6\text{RbBr}_3$," *Journal of Applied Crystallography*, vol. 47, pp. 532–538, Apr 2014.
- [27] B. J. Campbell, H. T. Stokes, D. E. Tanner, and D. M. Hatch, "ISODISPLACE: a web-based tool for exploring structural distortions," *Journal of Applied Crystallography*, vol. 39, pp. 607–614, Aug 2006.
- [28] C. Bradley and A. Cracknell, *The Mathematical Theory of Symmetry in Solids : Representation Theory for Point Groups and Space Groups*. Oxford University Press, revised ed., 2010.
- [29] L. D. Landau and E. M. Lifshitz, *Statistical Physics*, vol. 5. Butterworth-Heinemann, 3rd ed., 1980.
- [30] D. M. Hatch and H. T. Stokes, "INVARIANTS: program for obtaining a list of invariant polynomials of the order-parameter components associated with irreducible representations of a space group," *Journal of Applied Crystallography*, vol. 36, pp. 951–952, Jun 2003.
- [31] D. Orobengoa, C. Capillas, M. I. Aroyo, and J. M. Perez-Mato, "AMPLIMODES: symmetry-mode analysis on the Bilbao Crystallographic Server," *Journal of Applied Crystallography*, vol. 42, pp. 820–833, Oct 2009.
- [32] J. M. Perez-Mato, D. Orobengoa, and M. I. Aroyo, "Mode crystallography of distorted structures," *Acta Crystallographica Section A*, vol. 66, pp. 558–590, Sep 2010.

- [33] M. Born and R. Oppenheimer, "Zur quantentheorie der molekeln," *Annalen der Physik*, vol. 389, no. 20, pp. 457–484, 1927.
- [34] P. Hohenberg and W. Kohn, "Inhomogeneous electron gas," *Phys. Rev.*, vol. 136, pp. B864–B871, Nov 1964.
- [35] W. Kohn, "Nobel lecture: Electronic structure of matter—wave functions and density functionals," *Rev. Mod. Phys.*, vol. 71, pp. 1253–1266, Oct 1999.
- [36] W. Kohn and L. J. Sham, "Self-consistent equations including exchange and correlation effects," *Phys. Rev.*, vol. 140, pp. A1133–A1138, Nov 1965.
- [37] J. P. Perdew, K. Burke, and M. Ernzerhof, "Generalized gradient approximation made simple," *Phys. Rev. Lett.*, vol. 77, pp. 3865–3868, Oct 1996.
- [38] J. P. Perdew, A. Ruzsinszky, G. I. Csonka, O. A. Vydrov, G. E. Scuseria, L. A. Constantin, X. Zhou, and K. Burke, "Restoring the density-gradient expansion for exchange in solids and surfaces," *Phys. Rev. Lett.*, vol. 100, p. 136406, Apr 2008.
- [39] S. L. Dudarev, G. A. Botton, S. Y. Savrasov, C. J. Humphreys, and A. P. Sutton, "Electron-energy-loss spectra and the structural stability of nickel oxide: An lsda+u study," *Phys. Rev. B*, vol. 57, pp. 1505–1509, Jan 1998.
- [40] A. I. Liechtenstein, V. I. Anisimov, and J. Zaanen, "Density-functional theory and strong interactions: Orbital ordering in mott-hubbard insulators," *Phys. Rev. B*, vol. 52, pp. R5467–R5470, Aug 1995.
- [41] F. Aryasetiawan, K. Karlsson, O. Jepsen, and U. Schönberger, "Calculations of hubbard U from first-principles," *Phys. Rev. B*, vol. 74, p. 125106, Sep 2006.
- [42] H. J. Kulik, M. Cococcioni, D. A. Scherlis, and N. Marzari, "Density functional theory in transition-metal chemistry: A self-consistent hubbard U approach," *Phys. Rev. Lett.*, vol. 97, p. 103001, Sep 2006.
- [43] G. Kresse and J. Furthmüller, "Efficient iterative schemes for *ab initio* total-energy calculations using a plane-wave basis set," *Phys. Rev. B*, vol. 54, pp. 11169–11186, Oct 1996.
- [44] G. Kresse and J. Furthmüller, "Efficiency of ab-initio total energy calcula-

- tions for metals and semiconductors using a plane-wave basis set," *Computational Materials Science*, vol. 6, no. 1, pp. 15 – 50, 1996.
- [45] G. Kresse and D. Joubert, "From ultrasoft pseudopotentials to the projector augmented-wave method," *Phys. Rev. B*, vol. 59, pp. 1758–1775, Jan 1999.
- [46] H. J. Monkhorst and J. D. Pack, "Special points for brillouin-zone integrations," *Phys. Rev. B*, vol. 13, pp. 5188–5192, Jun 1976.
- [47] P. E. Blöchl, "Projector augmented-wave method," *Phys. Rev. B*, vol. 50, pp. 17953–17979, Dec 1994.
- [48] G. I. Csonka, J. P. Perdew, A. Ruzsinszky, P. H. T. Philipsen, S. Lebègue, J. Paier, O. A. Vydrov, and J. G. Ángyán, "Assessing the performance of recent density functionals for bulk solids," *Phys. Rev. B*, vol. 79, p. 155107, Apr 2009.
- [49] X. Gonze, "Perturbation expansion of variational principles at arbitrary order," *Phys. Rev. A*, vol. 52, pp. 1086–1095, Aug 1995.
- [50] X. Gonze, "Adiabatic density-functional perturbation theory," *Phys. Rev. A*, vol. 52, pp. 1096–1114, Aug 1995.
- [51] G. Henkelman, B. P. Uberuaga, and H. Jónsson, "A climbing image nudged elastic band method for finding saddle points and minimum energy paths," *The Journal of Chemical Physics*, vol. 113, no. 22, pp. 9901–9904, 2000.
- [52] G. Henkelman and H. Jónsson, "Improved tangent estimate in the nudged elastic band method for finding minimum energy paths and saddle points," *The Journal of Chemical Physics*, vol. 113, no. 22, pp. 9978–9985, 2000.
- [53] I. D. Brown, "Recent developments in the methods and applications of the bond valence model," *Chemical Reviews*, vol. 109, pp. 6858–6919, Dec 2009.
- [54] I. D. Brown, *The Chemical Bond in Inorganic Chemistry The Bond Valence Model*. Oxford University Press, second ed., 2016.
- [55] L. Pauling, "The principles determining the structure of complex ionic

- crystals," *Journal of the American Chemical Society*, vol. 51, pp. 1010–1026, Apr 1929.
- [56] R. Zhang, B. M. Abbett, G. Read, F. Lang, T. Lancaster, T. T. Tran, P. S. Halasyamani, S. J. Blundell, N. A. Benedek, and M. A. Hayward, "La₂SrCr₂O₇: Controlling the tilting distortions of n = 2 Ruddlesden-Popper phases through A-site cation order," *Inorganic Chemistry*, vol. 55, pp. 8951–8960, Sep 2016.
- [57] R. Zhang, G. Read, F. Lang, T. Lancaster, S. J. Blundell, and M. A. Hayward, "La₂SrCr₂O₇F₂: A Ruddlesden-Popper oxyfluoride containing octahedrally coordinated Cr⁴⁺ centers," *Inorganic Chemistry*, vol. 55, pp. 3169–3174, Mar 2016.
- [58] R. D. Shannon, "Revised effective ionic radii and systematic studies of interatomic distances in halides and chalcogenides," *Acta Crystallographica Section A*, vol. 32, pp. 751–767, Sep 1976.
- [59] K. S. Aleksandrov and J. Bartolome, "Octahedral tilt phases in perovskite-like crystals with slabs containing an even number of octahedral layers," *Journal of Physics: Condensed Matter*, vol. 6, no. 40, p. 8219, 1994.
- [60] G. H. Rao, K. Brner, and I. D. Brown, "Bond-valence analysis on the structural effects in magnetoresistive manganese perovskites," *Journal of Physics: Condensed Matter*, vol. 10, no. 48, p. L757, 1998.
- [61] W. H. Baur, "The geometry of polyhedral distortions. Predictive relationships for the phosphate group," *Acta Crystallographica Section B*, vol. 30, pp. 1195–1215, May 1974.
- [62] C. Darie, C. Goujon, M. Bacia, H. Klein, P. Toulemonde, P. Bordet, and E. Suard, "Magnetic and crystal structures of BiCrO₃," *Solid State Sciences*, vol. 12, no. 5, pp. 660 – 664, 2010. International Symposium on Structure-Property Relationships in Solid-State Materials.
- [63] J. Prado-Gonjal, R. Schmidt, J.-J. Romero, D. Ávila, U. Amador, and E. Morán, "Microwave-assisted synthesis, microstructure, and physical properties of rare-earth chromites," *Inorganic Chemistry*, vol. 52, pp. 313–320, Jan 2013.
- [64] A. A. Belik, Y. Matsushita, M. Tanaka, and E. Takayama-Muromachi, "Crystal structures and properties of perovskites ScCrO₃ and InCrO₃ with

small ions at the a site," *Chemistry of Materials*, vol. 24, pp. 2197–2203, Jun 2012.

- [65] N. N. Gurusinghe, J. de la Figuera, J. F. Marco, M. F. Thomas, F. J. Berry, and C. Greaves, "Synthesis and characterisation of the n=2 ruddlesden-popper phases $\text{Ln}_2\text{Sr}(\text{Ba})\text{Fe}_2\text{O}_7$ (Ln=La, Nd, Eu)," *Materials Research Bulletin*, vol. 48, no. 9, pp. 3537 – 3544, 2013.
- [66] N. N. Greenwood and A. Earnshaw, *Chemistry of the Elements*. Butterworth-Heinemann, second ed., 1997.
- [67] K. M. Rabe, *Antiferroelectricity in Oxides: A Reexamination*, pp. 221–244. Wiley-VCH Verlag GmbH & Co. KGaA, 2013.
- [68] H. Liu and B. Dkhil, "A brief review on the model antiferroelectric PbZrO_3 perovskite-like material," *Z. Krist-Cryst. Mater.*, vol. 226, pp. 163–170, Jan 2011.
- [69] X. Tan, C. Ma, J. Frederick, S. Beckman, and K. G. Webber, "The antiferroelectric ferroelectric phase transition in lead-containing and lead-free perovskite ceramics," *Journal of the American Ceramic Society*, vol. 94, no. 12, pp. 4091–4107, 2011.
- [70] A. K. Tagantsev, K. Vaideeswaran, S. B. Vakhrushev, A. V. Filimonov, R. G. Burkovsky, A. Shaganov, D. Andronikova, A. I. Rudskoy, A. Q. R. Baron, H. Uchiyama, D. Chernyshov, A. Bosak, Z. Ujma, K. Roleder, A. Majchrowski, J. H. Ko, and N. Setter, "The origin of antiferroelectricity in PbZrO_3 ," *Nat Commun*, vol. 4, 07 2013.
- [71] P. Tolédano and M. Guennou, "Theory of antiferroelectric phase transitions," *Phys. Rev. B*, vol. 94, p. 014107, Jul 2016.
- [72] A. Chauhan, S. Patel, R. Vaish, and C. R. Bowen, "Anti-ferroelectric ceramics for high energy density capacitors," *Materials*, vol. 8, no. 12, pp. 8009–8031, 2015.
- [73] S. Zhang, A. B. Kouna, W. Jo, C. Jamin, K. Seifert, T. Granzow, J. Rödel, and D. Damjanovic, "High-strain lead-free antiferroelectric electrostrictors," *Advanced Materials*, vol. 21, no. 46, pp. 4716–4720, 2009.
- [74] K. Uchino, "Antiferroelectric shape memory ceramics," *Actuators*, vol. 5, no. 2, 2016.

- [75] Z. Xu, J. Zhai, W.-H. Chan, and H. Chen, "Phase transformation and electric field tunable pyroelectric behavior of $\text{Pb}(\text{Nb,Zr,Sn,Ti})\text{O}_3$ and $(\text{Pb,Lu})(\text{Zr,Sn,Ti})\text{O}_3$ antiferroelectric thin films," *Applied Physics Letters*, vol. 88, no. 13, p. 132908, 2006.
- [76] G. Shirane, E. Sawaguchi, and Y. Takagi, "Dielectric properties of lead zirconate," *Phys. Rev.*, vol. 84, pp. 476–481, Nov 1951.
- [77] O. E. Fesenko, R. V. Kolesova, and Y. G. Sineyev, "The structural phase transitions in lead zirconate in super-high electric fields," *Ferroelectrics*, vol. 20, no. 1, pp. 177–178, 1978.
- [78] Z. Xu, X. Dai, D. Viehland, D. A. Payne, Z. Li, and Y. Jiang, "Ferroelectric domains and incommensuration in the intermediate phase region of lead zirconate," *Journal of the American Ceramic Society*, vol. 78, no. 8, pp. 2220–2224, 1995.
- [79] H. Fujishita and S. Katano, "Re-examination of the antiferroelectric structure of PbZrO_3 ," *Journal of the Physical Society of Japan*, vol. 66, no. 11, pp. 3484–3488, 1997.
- [80] D. L. Corker, A. M. Glazer, J. Dec, K. Roleder, and R. W. Whatmore, "A Re-investigation of the Crystal Structure of the Perovskite PbZrO_3 by X-ray and Neutron Diffraction," *Acta Crystallographica Section B*, vol. 53, pp. 135–142, Feb 1997.
- [81] Y. Kobayashi, S. Endo, L. Ming, K. Deguchi, T. Ashida, and H. Fujishita, "X-ray diffraction and dielectric measurements on PbZrO_3 at high pressure: a phase transformation study," *Journal of Physics and Chemistry of Solids*, vol. 60, no. 1, pp. 57 – 64, 1999.
- [82] H. Furuta, S. Endo, L. Ming, and H. Fujishita, "Phase transitions in PbZrO_3 under high pressure studied by raman scattering," *Journal of Physics and Chemistry of Solids*, vol. 60, no. 1, pp. 65 – 67, 1999.
- [83] A. G. S. Filho, P. T. C. Freire, A. P. Ayala, J. M. Sasaki, I. Guedes, J. M. Filho, F. E. A. Melo, E. B. Araújo, and J. A. Eiras, "The concentration-pressure phase diagram for Zr-rich $\text{PbZr}_{1-x}\text{Ti}_x\text{O}_3$ ceramics," *Journal of Physics: Condensed Matter*, vol. 12, no. 32, p. 7295, 2000.
- [84] H. He and X. Tan, "Electric-field-induced transformation of incommensurate modulations in antiferroelectric $\text{Pb}_{0.99}\text{Nb}_{0.02}[(\text{Zr}_{1-x}\text{Sn}_x)_{1-y}\text{Ti}_y]_{0.98}\text{O}_3$," *Phys. Rev. B*, vol. 72, p. 024102, Jul 2005.

- [85] X.-K. Wei, A. K. Tagantsev, A. Kvasov, K. Roleder, C.-L. Jia, and N. Setter, "Ferroelectric translational antiphase boundaries in nonpolar materials," *Nat Commun*, vol. 5, 01 2014.
- [86] R. G. Burkovsky, A. K. Tagantsev, K. Vaideeswaran, N. Setter, S. B. Vakhrushev, A. V. Filimonov, A. Shaganov, D. Andronikova, A. I. Rudskoy, A. Q. R. Baron, H. Uchiyama, D. Chernyshov, Z. Ujma, K. Roleder, A. Majchrowski, and J.-H. Ko, "Lattice dynamics and antiferroelectricity in PbZrO_3 tested by x-ray and brillouin light scattering," *Phys. Rev. B*, vol. 90, p. 144301, Oct 2014.
- [87] J. Hlinka, T. Ostapchuk, E. Buixaderas, C. Kadlec, P. Kuzel, I. Gregora, J. Kroupa, M. Savinov, A. Klic, J. Drahokoupil, I. Etxebarria, and J. Dec, "Multiple soft-mode vibrations of lead zirconate," *Phys. Rev. Lett.*, vol. 112, p. 197601, May 2014.
- [88] R. G. Burkovsky, I. Bronwald, D. Andronikova, B. Wehinger, M. Krisch, J. Jacobs, D. Gambetti, K. Roleder, A. Majchrowski, A. V. Filimonov, A. I. Rudskoy, S. B. Vakhrushev, and A. K. Tagantsev, "Critical scattering and incommensurate phase transition in antiferroelectric PbZrO_3 under pressure," *Scientific Reports*, vol. 7, p. 41512, Jan 2017.
- [89] D. J. Singh, "Structure and energetics of antiferroelectric PbZrO_3 ," *Phys. Rev. B*, vol. 52, pp. 12559–12563, Nov 1995.
- [90] R. Kagimura and D. J. Singh, "First-principles investigations of elastic properties and energetics of antiferroelectric and ferroelectric phases of PbZrO_3 ," *Phys. Rev. B*, vol. 77, p. 104113, Mar 2008.
- [91] S. E. Reyes-Lillo and K. M. Rabe, "Antiferroelectricity and ferroelectricity in epitaxially strained PbZrO_3 from first principles," *Phys. Rev. B*, vol. 88, p. 180102, Nov 2013.
- [92] J. Íñiguez, M. Stengel, S. Prosandeev, and L. Bellaiche, "First-principles study of the multimode antiferroelectric transition in PbZrO_3 ," *Phys. Rev. B*, vol. 90, p. 220103, Dec 2014.
- [93] B. K. Mani, S. Lisenkov, and I. Ponomareva, "Finite-temperature properties of antiferroelectric PbZrO_3 from atomistic simulations," *Phys. Rev. B*, vol. 91, p. 134112, Apr 2015.
- [94] N. Zhang, H. Yokota, A. M. Glazer, Z. Ren, D. A. Keen, D. S. Keeble, P. A.

- Thomas, and Z.-G. Ye, "The missing boundary in the phase diagram of $\text{PbZr}_{1-x}\text{Ti}_x\text{O}_3$," *Nat. Commun.*, vol. 5, p. 5231, Oct 2014.
- [95] H. Stokes, D. Hatch, and B. Campbell, *ISOTROPY Software Suite*, 2015. <http://iso.byu.edu>.
- [96] H. T. Stokes, E. H. Kisi, D. M. Hatch, and C. J. Howard, "Group-theoretical analysis of octahedral tilting in ferroelectric perovskites," *Acta Crystallographica Section B*, vol. 58, pp. 934–938, Dec 2002.
- [97] H. Fujishita, Y. Ishikawa, S. Tanaka, A. Ogawaguchi, and S. Katano, "Crystal structure and order parameters in the phase transition of antiferroelectric PbZrO_3 ," *Journal of the Physical Society of Japan*, vol. 72, no. 6, pp. 1426–1435, 2003.
- [98] M. Tanaka, R. Saito, and K. Tsuzuki, "Electron microscopic studies on domain structure of PbZrO_3 ," *Japanese Journal of Applied Physics*, vol. 21, no. 2R, p. 291, 1982.
- [99] X.-K. Wei, C.-L. Jia, K. Roleder, and N. Setter, "Polarity of translation boundaries in antiferroelectric PbZrO_3 ," *Materials Research Bulletin*, vol. 62, pp. 101 – 105, 2015.
- [100] J. T. Heron, J. L. Bosse, Q. He, Y. Gao, M. Trassin, L. Ye, J. D. Clarkson, C. Wang, J. Liu, S. Salahuddin, D. C. Ralph, D. G. Schlom, J. Iniguez, B. D. Huey, and R. Ramesh, "Deterministic switching of ferromagnetism at room temperature using an electric field," *Nature*, vol. 516, pp. 370–373, Dec 2014. Letter.
- [101] E. A. Nowadnick and C. J. Fennie, "Domains and ferroelectric switching pathways in $\text{Ca}_3\text{Ti}_2\text{O}_7$ from first principles," *Phys. Rev. B*, vol. 94, p. 104105, Sep 2016.
- [102] J. M. Perez-Mato, M. Aroyo, A. García, P. Blaha, K. Schwarz, J. Schweifer, and K. Parlinski, "Competing structural instabilities in the ferroelectric aurivillius compound $\text{SrBi}_2\text{Ta}_2\text{O}_9$," *Phys. Rev. B*, vol. 70, p. 214111, Dec 2004.
- [103] U. Petralanda and I. Etxebarria, "Ab initio study of the structural phase transitions of the double perovskites Sr_2MWO_6 ($M=\text{Zn}, \text{Ca}, \text{Mg}$)," *Phys. Rev. B*, vol. 89, p. 064107, Feb 2014.

- [104] N. A. Benedek, J. M. Rondinelli, H. Djani, P. Ghosez, and P. Lightfoot, "Understanding ferroelectricity in layered perovskites: new ideas and insights from theory and experiments," *Dalton Trans.*, vol. 44, pp. 10543–10558, 2015.
- [105] B. Kocsis, J. M. Perez-Mato, E. S. Tasci, G. de la Flor, and M. I. Aroyo, "A survey of the structural models proposed for $\text{PbZr}_{1-x}\text{Ti}_x\text{O}_3$ using mode analysis," *Journal of Applied Crystallography*, vol. 47, pp. 1165–1179, Aug 2014.
- [106] P. Ghosez, E. Cockayne, U. V. Waghmare, and K. M. Rabe, "Lattice dynamics of BaTiO_3 , PbTiO_3 , and PbZrO_3 : A comparative first-principles study," *Phys. Rev. B*, vol. 60, pp. 836–843, Jul 1999.
- [107] Z. Xu, X. H. Dai, J. F. Li, and D. Viehland, "Effects of quenched impurities and relative antiferroelectric/ferroelectric phase stability on the incommensurately modulated polar structures of La-modified lead zirconate titanate," *Applied Physics Letters*, vol. 71, no. 16, pp. 2280–2282, 1997.
- [108] S. Watanabe and Y. Koyama, "Features of the incommensurate phase in $\text{Pb}(\text{Zr}_{1-x}\text{Ti}_x)\text{O}_3$," *Phys. Rev. B*, vol. 66, p. 134102, Oct 2002.
- [109] I. MacLaren, R. Villaurretia, B. Schaffer, L. Houben, and A. Peliz-Barranco, "Atomic-scale imaging and quantification of electrical polarisation in incommensurate antiferroelectric lanthanum-doped lead zirconate titanate," *Advanced Functional Materials*, vol. 22, no. 2, pp. 261–266, 2012.
- [110] E. Boehm, J.-M. Bassat, P. Dordor, F. Mauvy, J.-C. Grenier, and P. Stevens, "Oxygen diffusion and transport properties in non-stoichiometric $\text{Ln}_{2-x}\text{NiO}_{4+\delta}$ oxides," *Solid State Ionics*, vol. 176, no. 37, pp. 2717 – 2725, 2005.
- [111] D. Parfitt, A. Kordatos, P. P. Filippatos, and A. Chroneos, "Diffusion in energy materials: Governing dynamics from atomistic modelling," *Applied Physics Reviews*, vol. 4, no. 3, p. 031305, 2017.
- [112] A. Demourgues, F. Weill, J. Grenier, A. Wattiaux, and M. Pouchard, "Electron microscopy study of electrochemically prepared $\text{La}_2\text{NiO}_{4+\delta}$ ($0.17 \leq \delta \leq 0.26$)," *Physica C: Superconductivity*, vol. 192, no. 3, pp. 425 – 434, 1992.
- [113] R. Sayers, R. D. Souza, J. Kilner, and S. Skinner, "Low temperature diffusion and oxygen stoichiometry in lanthanum nickelate," *Solid State Ionics*, vol. 181, no. 8, pp. 386 – 391, 2010.

- [114] J. Rodríguez-Carvajal, M. T. Fernández-Díaz, and J. L. Martínez, "Neutron diffraction study on structural and magnetic properties of La_2NiO_4 ," *Journal of Physics: Condensed Matter*, vol. 3, no. 19, p. 3215, 1991.
- [115] D. M. Hatch, H. T. Stokes, K. S. Aleksandrov, and S. V. Misyul, "Phase transitions in the perovskitelike $A_2\text{BX}_4$ structure," *Phys. Rev. B*, vol. 39, pp. 9282–9288, May 1989.
- [116] M. T. Fernández-Díaz, J. Rodríguez-Carvajal, J. L. Martínez, G. Fillion, F. Fernández, and R. Saez-Puche, "Structural and magnetic phase transitions in Pr_2NiO_4 ," *Zeitschrift für Physik B Condensed Matter*, vol. 82, pp. 275–282, Jun 1991.
- [117] A. de Andrés, J. L. Martínez, and P. Odier, "Dynamical study of the structural and magnetic phases in Pr_2NiO_4 single crystals by raman spectroscopy," *Phys. Rev. B*, vol. 45, pp. 12821–12829, Jun 1992.
- [118] J. Rodríguez-Carvajal, M. T. Fernández-Díaz, J. L. Martínez, F. Fernández, and R. Saez-Puche, "Structural phase transitions and three-dimensional magnetic ordering in the Nd_2NiO_4 oxide," *EPL (Europhysics Letters)*, vol. 11, no. 3, p. 261, 1990.
- [119] R. Puche, J. Rodriguez, and F. Fernández, "Non-stoichiometric aspects and physical properties of La_2NiO_4 oxide," *Inorganica Chimica Acta*, vol. 140, pp. 151 – 153, 1987.
- [120] A. Demourgues, F. Weill, B. Darriet, A. Wattiaux, J. Grenier, P. Gravereau, and M. Pouchard, "Additional oxygen ordering in " $\text{La}_2\text{NiO}_{4.25}$ " ($\text{La}_8\text{Ni}_4\text{O}_{17}$): I. electron and neutron diffraction study," *Journal of Solid State Chemistry*, vol. 106, no. 2, pp. 317 – 329, 1993.
- [121] A. Demourgues, F. Weill, B. Darriet, A. Wattiaux, J. Grenier, P. Gravereau, and M. Pouchard, "Additional oxygen ordering in " $\text{La}_2\text{NiO}_{4.25}$ " ($\text{La}_8\text{Ni}_4\text{O}_{17}$): II. structural features," *Journal of Solid State Chemistry*, vol. 106, no. 2, pp. 330 – 338, 1993.
- [122] M. Sayagués, M. Vallet-Reg, J. Hutchison, and J. González-Calbet, "Modulated structure of $\text{La}_2\text{NiO}_{4+\delta}$ as a mechanism of oxygen excess accommodation," *Journal of Solid State Chemistry*, vol. 125, no. 2, pp. 133 – 139, 1996.
- [123] S. J. Skinner, "Characterisation of $\text{La}_2\text{NiO}_{4+\delta}$ using in-situ high tempera-

ture neutron powder diffraction," *Solid State Sciences*, vol. 5, no. 3, pp. 419 – 426, 2003.

- [124] H. Eisaki, S. Uchida, T. Mizokawa, H. Namatame, A. Fujimori, J. van Elp, P. Kuiper, G. A. Sawatzky, S. Hosoya, and H. Katayama-Yoshida, "Electronic structure of $\text{La}_{2-x}\text{Sr}_x\text{NiO}_4$ studied by photoemission and inverse-photoemission spectroscopy," *Phys. Rev. B*, vol. 45, pp. 12513–12521, Jun 1992.
- [125] B. Dabrowski, J. Jorgensen, D. Hinks, S. Pei, D. Richards, H. Vanfleet, and D. Decker, " $\text{La}_2\text{CuO}_{4+\delta}$ and $\text{La}_2\text{NiO}_{4+\delta}$: Phase separation resulting from excess oxygen defects.," *Physica C: Superconductivity and its Applications*, vol. 162-164, pp. 99 – 100, 1989.
- [126] H. Tamura, A. Hayashi, and Y. Ueda, "Phase diagram of $\text{La}_2\text{NiO}_{4+\delta}$ ($0 \leq \delta \leq 0.18$) . I. Phase at room temperature and phases transition above $\delta = 0.15$," *Physica C Superconductivity*, vol. 216, pp. 83–88, Oct. 1993.
- [127] H. Tamura, A. Hayashi, and Y. Ueda, "Phase diagram of $\text{La}_2\text{NiO}_{4+\delta}$ ($0 \leq \delta \leq 0.18$) II. thermodynamics of excess oxygen, phase transitions ($0.06 \leq \delta < 0.11$) and phase segregation ($0.03 \leq \delta < 0.06$)," *Physica C: Superconductivity*, vol. 258, no. 1, pp. 61 – 71, 1996.
- [128] D. J. Buttrey, V. Sachan, J. M. Tranquada, and J. E. Lorenzo, "Stoichiometry, structure, and properties of $\text{La}_2\text{NiO}_{4+\delta}$ and $\text{La}_{2-x}\text{Sr}_x\text{NiO}_{4+\delta}$," in *Advances in Superconductivity VII* (K. Yamafuji and T. Morishita, eds.), (Tokyo), pp. 351–356, Springer Japan, 1995.
- [129] M. Hücker, K. Chung, M. Chand, T. Vogt, J. M. Tranquada, and D. J. Buttrey, "Oxygen and strontium codoping of La_2NiO_4 : Room-temperature phase diagrams," *Phys. Rev. B*, vol. 70, p. 064105, Aug 2004.
- [130] C. Allanyon, J. Rodríguez-Carvajal, M. Fernández-Díaz, P. Odier, J. Bassat, J. Loup, and J. Martínez, "Crystal structure of the high temperature phase of oxidised $\text{Pr}_2\text{NiO}_{4+\delta}$," *Zeitschrift für Physik B Condensed Matter*, vol. 100, pp. 85–90, Mar 1996.
- [131] Z. Hiroi, T. Obata, M. Takano, Y. Bando, Y. Takeda, and O. Yamamoto, "Ordering of interstitial oxygen atoms in $\text{La}_2\text{NiO}_{4+\delta}$ observed by transmission electron microscopy," *Phys. Rev. B*, vol. 41, pp. 11665–11668, Jun 1990.
- [132] V. M. Loktev and H. M. Tatarenko, "Ordered superstructures of oxygen

- ions in $\text{La}_2\text{MeO}_{4+\delta}$ (Me = Cu, Ni)," *physica status solidi (b)*, vol. 166, no. 1, pp. 191–200, 1991.
- [133] L. Otero-Diaz, A. Landa, F. Fernandez, R. Saez-Puche, R. Withers, and B. Hyde, "A tem study of the ordering of excess interstitial oxygen atoms in $\text{Ln}_2\text{NiO}_{4+\delta}$ (Ln = La, Nd)," *Journal of Solid State Chemistry*, vol. 97, no. 2, pp. 443 – 451, 1992.
- [134] J. M. Tranquada, Y. Kong, J. E. Lorenzo, D. J. Buttrey, D. E. Rice, and V. Sachan, "Oxygen intercalation, stage ordering, and phase separation in $\text{La}_2\text{NiO}_{4+\delta}$ with $0.05 \leq \delta \leq 0.11$," *Phys. Rev. B*, vol. 50, pp. 6340–6351, Sep 1994.
- [135] C. Allançon, A. Gonthier-Vassal, J. Bascat, J. Loup, and P. Odier, "Influence of oxygen on structural transitions in $\text{Pr}_2\text{NiO}_{4+\delta}$," *Solid State Ionics*, vol. 74, no. 3, pp. 239 – 248, 1994.
- [136] J. M. Tranquada, J. E. Lorenzo, D. J. Buttrey, and V. Sachan, "Cooperative ordering of holes and spins in $\text{La}_2\text{NiO}_{4.125}$," *Phys. Rev. B*, vol. 52, pp. 3581–3595, Aug 1995.
- [137] I. M. Abu-Shiekah, O. Bakharev, H. B. Brom, and J. Zaanen, "First time determination of the microscopic structure of a stripe phase: Low temperature NMR in $\text{La}_2\text{NiO}_{4.17}$," *Phys. Rev. Lett.*, vol. 87, p. 237201, Nov 2001.
- [138] J. D. Jorgensen, B. Dabrowski, S. Pei, D. R. Richards, and D. G. Hinks, "Structure of the interstitial oxygen defect in $\text{La}_2\text{NiO}_{4+\delta}$," *Phys. Rev. B*, vol. 40, pp. 2187–2199, Aug 1989.
- [139] W. Paulus, A. Cousson, G. Dhahlenne, J. Berthon, A. Revcolevschi, S. Hosoya, W. Treutmann, G. Heger, and R. L. Toquin, "Neutron diffraction studies of stoichiometric and oxygen intercalated La_2NiO_4 single crystals," *Solid State Sciences*, vol. 4, no. 5, pp. 565 – 573, 2002.
- [140] M. Yashima, M. Enoki, T. Wakita, R. Ali, Y. Matsushita, F. Izumi, and T. Ishihara, "Structural disorder and diffusional pathway of oxide ions in a doped Pr_2NiO_4 -based mixed conductor," *Journal of the American Chemical Society*, vol. 130, pp. 2762–2763, 03 2008.
- [141] A. Chroneos, D. Parfitt, J. A. Kilner, and R. W. Grimes, "Anisotropic oxygen diffusion in tetragonal $\text{La}_2\text{NiO}_{4+\delta}$: molecular dynamics calculations," *J. Mater. Chem.*, vol. 20, pp. 266–270, 2010.

- [142] D. Parfitt, A. Chroneos, J. A. Kilner, and R. W. Grimes, "Molecular dynamics study of oxygen diffusion in $\text{Pr}_2\text{NiO}_{4+\delta}$," *Phys. Chem. Chem. Phys.*, vol. 12, pp. 6834–6836, 2010.
- [143] M. Ceretti, O. Wahyudi, A. Cousson, A. Villesuzanne, M. Meven, B. Pedersen, J. M. Bassat, and W. Paulus, "Low temperature oxygen diffusion mechanisms in $\text{Nd}_2\text{NiO}_{4+\delta}$ and $\text{Pr}_2\text{NiO}_{4+\delta}$ via large anharmonic displacements, explored by single crystal neutron diffraction," *J. Mater. Chem. A*, vol. 3, pp. 21140–21148, 2015.
- [144] A. Perrichon, A. Piovano, M. Boehm, M. Zbiri, M. Johnson, H. Schober, M. Ceretti, and W. Paulus, "Lattice dynamics modified by excess oxygen in $\text{Nd}_2\text{NiO}_{4+\delta}$: Triggering low-temperature oxygen diffusion," *The Journal of Physical Chemistry C*, vol. 119, pp. 1557–1564, 01 2015.
- [145] A. Piovano, A. Perrichon, M. Boehm, M. R. Johnson, and W. Paulus, "Positional recurrence maps, a powerful tool to de-correlate static and dynamical disorder in distribution maps from molecular dynamics simulations: the case of $\text{Nd}_2\text{NiO}_{4+\delta}$," *Phys. Chem. Chem. Phys.*, vol. 18, pp. 17398–17403, 2016.
- [146] D. M. Halat, R. Dervişoğlu, G. Kim, M. T. Dunstan, F. Blanc, D. S. Middlemiss, and C. P. Grey, "Probing oxide-ion mobility in the mixed ionic-electronic conductor $\text{La}_2\text{NiO}_{4+\delta}$ by solid-state ^{17}O mas nmr spectroscopy," *Journal of the American Chemical Society*, vol. 138, pp. 11958–11969, 09 2016.
- [147] S. Skinner and J. Kilner, "Oxygen diffusion and surface exchange in $\text{La}_{2-x}\text{Sr}_x\text{NiO}_{4+\delta}$," *Solid State Ionics*, vol. 135, no. 1, pp. 709 – 712, 2000. Proceedings of the 12th International Conference on Solid State.
- [148] J. Bassat, P. Odier, A. Villesuzanne, C. Marin, and M. Pouchard, "Anisotropic ionic transport properties in $\text{La}_2\text{NiO}_{4+\delta}$ single crystals," *Solid State Ionics*, vol. 167, no. 3, pp. 341 – 347, 2004.
- [149] M. Burriel, G. Garcia, J. Santiso, J. A. Kilner, R. J. Chater, and S. J. Skinner, "Anisotropic oxygen diffusion properties in epitaxial thin films of $\text{La}_2\text{NiO}_{4+\delta}$," *J. Mater. Chem.*, vol. 18, pp. 416–422, 2008.
- [150] X. Li and N. A. Benedek, "Enhancement of ionic transport in complex oxides through soft lattice modes and epitaxial strain," *Chemistry of Materials*, vol. 27, pp. 2647–2652, 04 2015.

- [151] A. Chroneos, B. Yildiz, A. Tarancon, D. Parfitt, and J. A. Kilner, "Oxygen diffusion in solid oxide fuel cell cathode and electrolyte materials: mechanistic insights from atomistic simulations," *Energy Environ. Sci.*, vol. 4, pp. 2774–2789, 2011.
- [152] A. Zunger, S.-H. Wei, L. G. Ferreira, and J. E. Bernard, "Special quasirandom structures," *Phys. Rev. Lett.*, vol. 65, pp. 353–356, Jul 1990.
- [153] R. Grau-Crespo, S. Hamad, C. R. A. Catlow, and N. H. de Leeuw, "Symmetry-adapted configurational modelling of fractional site occupancy in solids," *Journal of Physics: Condensed Matter*, vol. 19, no. 25, p. 256201, 2007.
- [154] G. L. W. Hart and R. W. Forcade, "Algorithm for generating derivative structures," *Phys. Rev. B*, vol. 77, p. 224115, Jun 2008.
- [155] S. Mustapha, P. D'Arco, M. D. L. Pierre, Y. Nol, M. Ferrabone, and R. Dovesi, "On the use of symmetry in configurational analysis for the simulation of disordered solids," *Journal of Physics: Condensed Matter*, vol. 25, no. 10, p. 105401, 2013.
- [156] K. Okhotnikov, T. Charpentier, and S. Cadars, "Supercell program: a combinatorial structure-generation approach for the local-level modeling of atomic substitutions and partial occupancies in crystals," *Journal of Cheminformatics*, vol. 8, p. 17, Mar 2016.
- [157] A. Santoro and A. D. Mighell, "Properties of crystal lattices: the derivative lattices and their determination," *Acta Crystallographica Section A*, vol. 28, pp. 284–287, May 1972.
- [158] J. H. Lloyd-Williams and B. Monserrat, "Lattice dynamics and electron-phonon coupling calculations using nondiagonal supercells," *Phys. Rev. B*, vol. 92, p. 184301, Nov 2015.
- [159] A. K. Lenstra, H. W. Lenstra, and L. Lovász, "Factoring polynomials with rational coefficients," *Mathematische Annalen*, vol. 261, pp. 515–534, Dec 1982.
- [160] Y.-L. Lee, J. Kleis, J. Rossmeisl, and D. Morgan, "Ab initio energetics of $\text{LaBO}_3(001)$ ($B = \text{Mn, Fe, Co, and Ni}$) for solid oxide fuel cell cathodes," *Phys. Rev. B*, vol. 80, p. 224101, Dec 2009.

- [161] W. Xie, Y.-L. Lee, Y. Shao-Horn, and D. Morgan, "Oxygen point defect chemistry in ruddlesden–popper oxides $(\text{La}_{1-x}\text{Sr}_x)_2\text{MO}_{4\pm\delta}$ ($\text{M} = \text{Co}, \text{Ni}, \text{Cu}$)," *The Journal of Physical Chemistry Letters*, vol. 7, pp. 1939–1944, 05 2016.
- [162] H. Jiang, P. Rinke, and M. Scheffler, "Electronic properties of lanthanide oxides from the GW perspective," *Phys. Rev. B*, vol. 86, p. 125115, Sep 2012.
- [163] M. T. Czyżyk and G. A. Sawatzky, "Local-density functional and on-site correlations: The electronic structure of La_2CuO_4 and LaCuO_3 ," *Phys. Rev. B*, vol. 49, pp. 14211–14228, May 1994.
- [164] S. Okamoto, A. J. Millis, and N. A. Spaldin, "Lattice relaxation in oxide heterostructures: $\text{LaTiO}_3/\text{SrTiO}_3$ superlattices," *Phys. Rev. Lett.*, vol. 97, p. 056802, Jul 2006.
- [165] L. Wang, T. Maxisch, and G. Ceder, "Oxidation energies of transition metal oxides within the GGA + U framework," *Phys. Rev. B*, vol. 73, p. 195107, May 2006.
- [166] D. C. Patton, D. V. Porezag, and M. R. Pederson, "Simplified generalized-gradient approximation and anharmonicity: Benchmark calculations on molecules," *Phys. Rev. B*, vol. 55, pp. 7454–7459, Mar 1997.
- [167] J. D. Gale, "Gulp: A computer program for the symmetry-adapted simulation of solids," *J. Chem. Soc., Faraday Trans.*, vol. 93, pp. 629–637, 1997.
- [168] A. R. Overy, A. B. Cairns, M. J. Cliffe, A. Simonov, M. G. Tucker, and A. L. Goodwin, "Design of crystal-like aperiodic solids with selective disorder–phonon coupling," *Nature Communications*, vol. 7, 02 2016.
- [169] A. R. Overy, A. Simonov, P. A. Chater, M. G. Tucker, and A. L. Goodwin, "Phonon broadening from supercell lattice dynamics: Random and correlated disorder," *physica status solidi (b)*, vol. 254, no. 4, p. 1600586, 2016.
- [170] X. Gonze and C. Lee, "Dynamical matrices, born effective charges, dielectric permittivity tensors, and interatomic force constants from density-functional perturbation theory," *Phys. Rev. B*, vol. 55, pp. 10355–10368, Apr 1997.
- [171] Y. Hinuma, G. Pizzi, Y. Kumagai, F. Oba, and I. Tanaka, "Band structure

diagram paths based on crystallography," *Computational Materials Science*, vol. 128, pp. 140 – 184, 2017.

- [172] T. Zhu, K. SwaminathanGopalan, K. J. Cruse, K. Stephani, and E. Ertekin, "Vibrational energy transport in hybrid ordered/disordered nanocomposites: Hybridization and avoided crossings of localized and delocalized modes," *Advanced Functional Materials*, vol. 28, no. 17, p. 1706268.